# CONSTRAINTS ON THE ASSEMBLY AND DYNAMICS OF GALAXIES. I. DETAILED REST-FRAME OPTICAL MORPHOLOGIES ON KILOPARSEC SCALE OF $z \sim 2$ STAR-FORMING GALAXIES[*]

N. M. FÖRSTER SCHREIBER[1], A. E. SHAPLEY[2], D. K. ERB[3,10], R. GENZEL[1,4], C. C. STEIDEL[5], N. BOUCHÉ[3,6,7,9], G. CRESCI[8],
AND R. DAVIES[1]

[1] Max-Planck-Institut für extraterrestrische Physik, Giessenbachstrasse, D-85748 Garching, Germany
[2] Department of Physics and Astronomy, University of California, Los Angeles, CA 90095-1547, USA
[3] Department of Physics, University of California Santa Barbara, Santa Barbara, California, CA 93106-9530, USA
[4] Department of Physics, University of California, Berkeley, CA 94720, USA
[5] California Institute of Technology, MS 105-24, Pasadena, CA 91125, USA
[6] CNRS, Institut de Recherche en Astrophysique et Planétologie de Toulouse, 14 Avenue E. Belin, F-31400 Toulouse, France
[7] Université de Toulouse, UPS-OMP, IRAP, F-31400 Toulouse, France
[8] INAF-Osservatorio Astrofisico di Arcetri, Largo E. Fermi 5, I-50125 Firenze, Italy
*Received 2010 November 5; accepted 2011 February 8; published 2011 March 24*

## ABSTRACT

We present deep and high-resolution *Hubble Space Telescope* NIC2 F160W imaging at $1.6\,\mu$m of six $z \sim 2$ star-forming galaxies with existing near-infrared integral field spectroscopy from SINFONI at the Very Large Telescope. The unique combination of rest-frame optical imaging and nebular emission-line maps provides simultaneous insight into morphologies and dynamical properties. The overall rest-frame optical emission of the galaxies is characterized by shallow profiles in general (Sérsic index $n < 1$), with median effective radii of $R_{\rm e} \sim 5$ kpc. The morphologies are significantly clumpy and irregular, which we quantify through a non-parametric morphological approach, estimating the Gini ($G$), multiplicity ($\Psi$), and $M_{20}$ coefficients. The estimated strength of the rest-frame optical emission lines in the F160W bandpass indicates that the observed structure is not dominated by the morphology of line-emitting gas, and must reflect the underlying stellar mass distribution of the galaxies. The sizes and structural parameters in the rest-frame optical continuum and H$\alpha$ emission reveal no significant differences, suggesting similar global distributions of the ongoing star formation and more evolved stellar population. While no strong correlations are observed between stellar population parameters and morphology within the NIC2/SINFONI sample itself, a consideration of the sample in the context of a broader range of $z \sim 2$ galaxy types ($K$-selected quiescent, active galactic nucleus, and star forming; 24 $\mu$m selected dusty, infrared-luminous) indicates that these galaxies probe the high specific star formation rate and low stellar mass surface density part of the massive $z \sim 2$ galaxy population, with correspondingly large effective radii, low Sérsic indices, low $G$, and high $\Psi$ and $M_{20}$. The combined NIC2 and SINFONI data set yields insights of unprecedented detail into the nature of mass accretion at high redshift.

*Key words:* galaxies: evolution – galaxies: high-redshift – galaxies: kinematics and dynamics – galaxies: structure

*Online-only material:* color figures

## 1. INTRODUCTION

A fundamental but still unsolved issue is the origin of the Hubble sequence and the formation of the spheroidal and disk components of present-day galaxies. Observations indicate that the Hubble sequence emerges around $z \sim 1$–2, along with the closely connected bimodality in integrated rest-frame optical colors characterized by a "red sequence" of mostly elliptical/bulge-dominated early types and a "blue cloud" of generally disk-dominated and irregular late types (e.g., Bell et al. 2004; van den Bergh et al. 1996, 2001; Lilly et al. 1998; Stanford et al. 2004; Ravindranath et al. 2004; Papovich et al. 2005; Kriek et al. 2008a, 2009; Williams et al. 2009). Although colors are easier to measure, morphologies potentially yield more information about the processes that shape galaxies over time. Morphological studies reveal a progressively larger proportion of irregular and disk-like types at higher redshift compared to the local galaxy population (e.g., Lotz et al. 2004, 2006; Law et al. 2007b; Scarlata et al. 2007a, 2007b; Elmegreen et al. 2007; Pannella et al. 2009), hinting at the diversity of the processes driving early galaxy evolution.

Morphologies, however, can be difficult to interpret. Band-shifting can plausibly explain part of the observed changes in morphologies; high-resolution imaging conducted so far mostly in the optical regime traces rest-UV wavelengths at $z \gtrsim 1$, which are more affected by dust obscuration and ongoing star formation (e.g., Toft et al. 2007; Overzier et al. 2010; Cameron et al. 2010). Star-forming sites within galaxies may also evolve in size and spatial distribution as a result of different dominant triggering mechanisms, and different physical and dynamical conditions prevailing at earlier epochs. Kiloparsec-sized "clumps" are in fact ubiquitous among high-$z$ star-forming galaxies and are believed to be at least in part due to fragmentation in Toomre-unstable gas-rich disks (e.g., Elmegreen et al. 2007, 2009, and references therein). There is now direct kinematic evidence that high-$z$ disks are significantly more turbulent (and geometrically thicker) than their $z \sim 0$ counterparts, implying accordingly larger Jeans length setting the characteristic size scale of self-gravitating star-forming complexes (e.g., Bournaud et al. 2007, 2008; Genzel et al. 2008, 2010). High gas mass fractions

at $z \sim$ 1–2.5 have also been confirmed through observations of CO rotational transitions (e.g., Tacconi et al. 2010; Daddi et al. 2010). Higher merger rates in the young universe may further contribute to the irregular appearance of galaxies. Merger-induced morphological disturbances can however last over a wide range of timescales, from <100 Myr up to >1 Gyr depending on progenitors' baryonic mass ratio, gas fraction, and orbital parameters (e.g., Lotz et al. 2008, 2010a, 2010b).

Information on the galaxy kinematics is therefore crucial to establish the nature and dynamical state of high $z$ galaxies. Kinematics provide powerful diagnostics to distinguish reliably between disks and mergers as a function of the degree of symmetry of velocity fields and velocity dispersion maps (e.g., Krajnović et al. 2006; Flores et al. 2006; Shapiro et al. 2008; Épinat et al. 2010), and to determine the main source of dynamical support from the ratio of rotation velocity to local intrinsic velocity dispersion (e.g., Puech et al. 2007; Cresci et al. 2009; Épinat et al. 2009). Spatially resolved mapping of the two-dimensional kinematics at $z \gtrsim 1$ has become possible during the past decade, with the newest generation of sensitive near-IR integral field spectrographs mounted on ground-based 10 m class telescopes.

Using the near-IR integral field spectrometer SINFONI at the ESO Very Large Telescope (VLT), we carried out the first and largest survey to date of the gas kinematics of 80 $z \sim$ 1–3 galaxies, "SINS" (Förster Schreiber et al. 2006b, 2009; Genzel et al. 2006, 2008; Bouché et al. 2007; Shapiro et al. 2008; Cresci et al. 2009). The survey includes 62 rest-UV/optically selected objects at 1.3 < $z$ < 2.6 for which we targeted primarily the Hα and [N II] emission lines. This "SINS Hα sample" covers roughly two orders of magnitude in stellar mass ($M_\star \approx 3 \times 10^9$–$3 \times 10^{11}$ $M_\odot$) and star formation rate (SFR $\approx$ 10–800 $M_\odot$ yr$^{-1}$). The line emission is resolved on typical spatial scales of 4–5 kpc for the seeing-limited data and down to 1–2 kpc for the subset of 11 sources followed-up with adaptive optics (AO). Kinematically, about one-third of the SINS galaxies are rotation-dominated yet turbulent disks, another third comprises typically more compact dispersion-dominated objects, and the remaining sources are interacting/merging systems. Concurring results on the kinematic mix at $z \sim$ 1–3 have been found by other groups (e.g., Erb et al. 2003, 2004, 2006; Wright et al. 2007, 2009; Law et al. 2007a, 2009; Stark et al. 2008; Épinat et al. 2009; Jones et al. 2010). If the relative proportions vary somewhat between different studies, possibly reflecting in part differences in samples and mass/redshift ranges, the existence of disks in the early universe and their typically high intrinsic local velocity dispersion now seem fairly well established. Under these conditions, and in the absence of major mergers, internal dynamical processes can drive the secular evolution of disks and formation of bulges/spheroids on timescales $\sim$1 Gyr, about an order of magnitude faster than in present-day disks (e.g., Noguchi 1999; Immeli et al. 2004a, 2004b; Carollo et al. 2007; Bournaud et al. 2007; Genzel et al. 2008; Elmegreen et al. 2009).

While Hα emission provides an excellent probe of the sites of ongoing star formation activity and the current dynamical state of a galaxy, broadband rest-frame optical imaging with high spatial resolution is required to characterize the structural properties of the underlying stellar component. Dynamical processes at play in the past are imprinted in the stellar mass distribution, and the stellar population contains a record of earlier star formation. Unique insights into early galaxy evolution can therefore be gained from the powerful combination of ionized

gas kinematics and spatial distribution from Hα with detailed morphologies from high-resolution broadband imaging.

In this paper, we present the results of deep high-resolution imaging at 1.6 $\mu$m with the NICMOS/NIC2 camera on board the *Hubble Space Telescope* (*HST*) of six of the SINS galaxies at 2.1 < $z$ < 2.5. The NICMOS imaging probes the rest-frame 5000 Å continuum of the galaxies, redward of the Balmer/4000 Å break. In this range, light from longer-lived, lower-mass stars that make up the bulk of the stellar mass becomes more important compared to that of young hot stars shining more brightly at shorter wavelengths, and the effects of dust extinction are smaller than in the rest-UV. Five of the targets exhibit compelling signatures of disk-like kinematics. The kinematics of the sixth source unambiguously reveals a major merger, although this is not obvious from the surface brightness distribution of Hα at seeing-limited resolution. The original motivation for our NIC2 follow-up was to determine whether the stellar light/mass distribution of the kinematically identified disks also follows a disk-like profile and to unveil the components of the merger system.

With the deep $\sim$1 kpc resolution NIC2 1.6 $\mu$m imaging, our primary goals in the present study are to derive the global structural parameters and the detailed morphologies of the galaxies as traced by the stellar light. We further explore the connection with stellar population properties and, taking advantage of the high-quality SINFONI data of our targets, we test if and how the structure relates to the dynamical properties. Our targets extend up to the high-mass end of the rest-UV-selected $z \sim$ 2 population and overlap in mass and redshift range with other massive galaxy samples with deep and high-resolution NIC2 1.6 $\mu$m data studied by van Dokkum et al. (2008), Dasyra et al. (2008), and Kriek et al. (2009). The similar NIC2 data sets between these samples and ours allow consistent comparisons of the structural and morphological properties of massive $z \approx$ 2–2.5 galaxies selected through different criteria and, anticipating our results, show how galaxies of similar masses can be very different in those respects, reflecting a wide range in star formation activity. In a companion paper (N. M. Förster Schreiber et al. 2011, in preparation; hereafter Paper II), we focus on the properties of the kpc-scale clumps identified in the NIC2 images of our targets and derive constraints on the nature and evolution of these clumps.

The paper is organized as follows. We introduce the sample and the SINFONI data sets, and describe the NIC2 observations and data reduction in Section 2. In Section 3, we revisit the global photometric and stellar populations properties of the galaxies with the inclusion of the new NIC2 1.6 $\mu$m data and place them in the broader context of $z \sim$ 2 populations in terms of stellar mass, star formation rate (SFR), and kinematics. We present the structural and morphological analysis in Section 4 and combine the NIC2 broadband imaging together with the emission line data from SINFONI in Section 5. We compare our sample to other massive galaxy samples at $z \sim$ 2–2.6 in terms of structural and morphological properties and address the connection with stellar populations in Section 6. In Section 7, we constrain the spatial distribution of stellar mass in one of our targets with additional high-resolution data from the *HST*/Advanced Camera for Surveys (ACS), compare the rest-frame optical and Hα sizes, and discuss the relation between morphologies and Hα kinematics. We summarize the paper in Section 8. Throughout the paper, we assume a Λ-dominated cosmology with $H_0 = 70\,h_{70}$ km s$^{-1}$ Mpc$^{-1}$, $\Omega_m = 0.3$, and $\Omega_\Lambda = 0.7$. For this cosmology, $1''$ corresponds to $\approx$8.2 kpc at

**Table 1**
Galaxies Observed

| Object | $z_{H\alpha}$[a] | Kinematic Type[b] | $U_n$ (mag) | $G$ (mag) | $\mathcal{R}$ (mag) | $J$ (mag) | $H_{160}$ (mag) | $K_s$ (mag) |
|---|---|---|---|---|---|---|---|---|
| Q1623 − BX528 | 2.2683 | Major merger | 24.52 ± 0.18 | 23.81 ± 0.14 | 23.56 ± 0.13 | 22.44 ± 0.17 | 22.33 ± 0.06 | 21.61 ± 0.20 |
| Q1623 − BX663[c] | 2.4332 | Disk | 25.40 ± 0.24 | 24.38 ± 0.17 | 24.14 ± 0.15 | 23.41 ± 0.30 | 22.79 ± 0.10 | 21.78 ± 0.21 |
| SSA22a − MD41 | 2.1704 | Disk | 24.81 ± 0.11 | 23.50 ± 0.06 | 23.31 ± 0.05 | ⋯ | 22.64 ± 0.05 | 22.30 ± 0.36 |
| Q2343 − BX389 | 2.1733 | Disk | 26.39 ± 0.39 | 25.13 ± 0.19 | 24.85 ± 0.16 | 23.82 ± 0.24 | 23.11 ± 0.10 | 22.04 ± 0.25 |
| Q2343 − BX610[c] | 2.2103 | Disk | 24.67 ± 0.21 | 23.92 ± 0.12 | 23.58 ± 0.11 | 22.35 ± 0.13 | 22.09 ± 0.06 | 21.07 ± 0.13 |
| Q2346 − BX482 | 2.2571 | Disk | 24.44 ± 0.12 | 23.54 ± 0.10 | 23.32 ± 0.09 | ⋯ | 22.34 ± 0.07 | ⋯ |

**Notes.** Magnitudes are given in the AB system. Optical, $J$ and $K_s$ magnitudes are taken from Erb et al. (2006; with the exception of SSA22a − MD41 for which the $K_s$ magnitude was measured on NTT/SOFI imaging available from the ESO archive). The $H_{160}$-band magnitudes were measured from the new NICMOS/NIC2 data presented in this paper.
[a] Systemic vacuum redshift derived from the integrated Hα line emission in the SINFONI data (Förster Schreiber et al. 2009).
[b] Classification according to the Hα kinematics from SINFONI (Shapiro et al. 2008; Förster Schreiber et al. 2006b, 2009).
[c] Spectral signatures of an AGN are detected in the optical and near-IR spectrum of Q1623 − BX663 and the large-scale Hα kinematics suggest that the host galaxy is a low-inclination rotating disk (Erb et al. 2006; Förster Schreiber et al. 2006b, 2009). The *Spitzer*/MIPS fluxes of Q1623−BX663 and Q2343−BX610 are indicative of obscured AGN activity (Reddy et al. 2010).

$z = 2.2$. Magnitudes are given in the AB photometric system unless otherwise specified.

## 2. SAMPLE, OBSERVATIONS, DATA REDUCTION

### 2.1. *Choice of NICMOS/NIC2 Targets*

Table 1 lists the galaxies observed along with their photometric properties. They were drawn from the initial sample of 17 rest-UV-selected objects at $z \sim 2$ from the SINS survey (Förster Schreiber et al. 2006b, 2009) carried out with SINFONI (Eisenhauer et al. 2003; Bonnet et al. 2004) at the ESO VLT. The galaxies were originally part of the large optical spectroscopic survey of $z \sim 1.5$–2.5 candidates selected by their $U_n G \mathcal{R}$ colors described by Steidel et al. (2004, see also Adelberger et al. 2004). Additional multi-wavelength data include ground-based near-IR $J$ and $K_s$ imaging, and space-based *Spitzer* mid-IR photometry at 3–8 $\mu$m with IRAC and at 24 $\mu$m with MIPS for the majority of our targets (Erb et al. 2006; Reddy et al. 2010, and Förster Schreiber et al. 2009 for the $K_s$-band photometry of MD 41). Prior to the SINFONI observations, near-IR long-slit spectroscopy was obtained for all of our NIC2 targets with NIRSPEC at the Keck II telescope and ISAAC at the VLT by Erb et al. (2003, 2006) and Shapley et al. (2004).

The choice of our NIC2 targets was primarily driven by their kinematic nature along with their high signal-to-noise ratio (S/N), high-quality SINFONI data mapping the spatial distribution, and relative gas motions from Hα out to radii $\gtrsim 10$ kpc (Förster Schreiber et al. 2006b). They include five rotating disks (BX 663, MD 41, BX 389, BX 610, and BX 482) and one major merger (BX 528). The quantitative kinematic classification performed through application of kinemetry is described by Shapiro et al. (2008), and detailed dynamical modeling of the disks is presented by Genzel et al. (2008) and Cresci et al. (2009). The disks show the expected signatures of a fairly ordered two-dimensional velocity field, with a monotonic gradient across the source and flattening of the velocity curve at large radii, alignment of the Hα kinematic and morphological major axes, and peak of the velocity dispersion close to the dynamical and geometrical center. In contrast, BX 528 exhibits a reversal in velocity gradient along the major axis, as observed in nearby counterrotating binary mergers. Interestingly, the Hα morphology of this merger from the seeing-limited SINFONI data does not show features that would distinguish it from

the disks; all sources have extended, more or less irregular/clumpy Hα distributions at a typical seeing-limited resolution of $\approx 0\rlap{.}''5$.

Two of our targets (BX 663 and BX 610) are candidate active galactic nucleus (AGN) hosts on the basis of their observed mid-IR spectral energy distributions (SEDs) from *Spitzer* IRAC and MIPS photometry (Reddy et al. 2010; N. Reddy 2010, private communication). BX 663 also exhibits spectral signatures of Type 2 AGN in its integrated rest-UV and rest-optical spectrum (Shapley et al. 2004; Erb et al. 2006). In our spatially resolved SINFONI data (as well as the new NIC2 imaging presented in this paper), the host galaxy is well detected and can be distinguished from the central compact emission peak with higher [N II]/Hα and broad Hα velocity component associated with the AGN, underneath the narrower component dominated by star formation. In contrast, BX 610 exhibits no sign of AGN in the rest-frame UV and optical, including the spatially and spectrally resolved SINFONI data, so that its AGN is likely to be very obscured and will not affect any aspect of our analysis. Therefore, in the context of this paper, we will only consider BX 663 explicitly as an AGN source.

### 2.2. *SINFONI Data Sets*

The SINFONI data sets of our NIC2 targets are fully described by Förster Schreiber et al. (2009). They are among the deepest of the SINS survey, with on-source integration times in the $K$ band (targeting the Hα and [N II] $\lambda\lambda 6548$, 6584 emission lines) ranging from 3 to 7.3 hr. All galaxies were first observed using the largest pixel scale ($0\rlap{.}''125$ pixel$^{-1}$), five of them in seeing-limited mode under very good seeing conditions, and one of them (BX 663) with the aid of AO using a nearby natural guide star. The typical effective angular resolution of these SINFONI $K$-band data has an FWHM $\approx 0\rlap{.}''5$, corresponding to $\approx 4.1$ kpc at the redshift of the sources (FWHM = $0\rlap{.}''39$ or 3.2 kpc for the NGS-AO data of BX 663). Seeing-limited $H$-band data were taken for all but BX 528 to map the [O III] $\lambda\lambda 4959$, 5007 and Hβ emission lines, also under a very good near-IR seeing of $\approx 0\rlap{.}''55$ and using the $0\rlap{.}''125$ pixel$^{-1}$ scale. In addition, Laser Guide Star (LGS) AO-assisted $K$-band observations were obtained for BX 482 using the intermediate pixel scale of $0\rlap{.}''05$ pixel$^{-1}$, with a total on-source integration time of 6.8 hr and an effective resolution of $0\rlap{.}''17$ (1.4 kpc), very similar to that of the NIC2 1.6 $\mu$m imaging.

**Table 2**
Log of NICMOS/NIC2 Observations

| Object | Date Observed | P.A.[a] (deg) | $3\sigma$ Limit in $d = 0\rlap.{''}22$[b] (mag) |
|---|---|---|---|
| Q1623 − BX528 | 2007 Apr 27 | −5.43 | 28.07 |
| Q1623 − BX663 | 2007 Apr 28–29 | −20.43 | 28.17 |
| SSA22a − MD41 | 2007 May 7–8 | 30.13 | 27.98 |
| Q2343 − BX389 | 2007 Jul 10 | 16.91 | 28.08 |
| Q2343 − BX610 | 2007 Sep 24 | −45.43 | 28.14 |
| Q2346 − BX482 | 2007 Jul 18 | 4.57 | 28.22 |

**Notes.** The total on-source integration time is 10,240 s for all targets.
[a] Position angle of the $y$-axis (in degrees east of north).
[b] Effective $3\sigma$ background noise limiting magnitudes (AB system) in a "point-source" circular aperture with diameter $d = 0\rlap.{''}22$, or $1.5 \times$ FWHM of the NIC2 PSF as measured from stellar profiles in the data. The limiting depths were determined from the analysis of the noise properties of the reduced data presented in Section 2.6.

The central averaged Hα surface brightness (within the Hα half-light radius) of the NIC2 targets ranges from $\approx 1 \times 10^{-17}$ to $\approx 1 \times 10^{-16}$ erg s$^{-1}$ cm$^{-2}$ arcsec$^{-2}$. Using the conversion factor of Kennicutt (1998) between the Hα luminosity and SFR, divided by 1.7 to scale from a Salpeter (1955) to a Chabrier (2003) initial mass function (IMF), and accounting for beam smearing in computing the intrinsic physical area, we calculate SFRs per unit area of $\approx 0.15$–$0.4\ M_\odot$ yr$^{-1}$ kpc$^{-2}$ (uncorrected for dust extinction). The median S/N per pixel of the Hα maps over the regions where line emission is detected (i.e., S/N > 3) is $\approx 10$–15 for the six galaxies. From the velocity-integrated line maps and the noise properties of the data cubes (see details in Förster Schreiber et al. 2009), the $3\sigma$ Hα surface brightness sensitivities are typically $\approx 10^{-17}$ erg s$^{-1}$ cm$^{-2}$ arcsec$^{-2}$, corresponding to a limiting SFR of $\approx 0.03\ M_\odot$ yr$^{-1}$ kpc$^{-2}$.

### 2.3. NICMOS/NIC2 Observations

The NICMOS observations were carried out between 2007 April and 2007 September with the NIC2 camera onboard the *HST* and using the F160W filter (hereafter referred to as the $H_{160}$ bandpass). The $H_{160}$ bandpass, centered at 1.6 μm (FWHM = 0.4 μm), probes the longest wavelengths at which the *HST* thermal emission is unimportant, taking full advantage of the lack of sky background that limits the sensitivity of ground-based near-IR observations. NIC2 has a pixel scale of $0\rlap.{''}075$, critically sampling the *HST* point-spread function (PSF) at 1.6 μm, and a field of view (FOV) of $19\rlap.{''}2 \times 19\rlap.{''}2$. While the NIC3 camera has greater surface brightness sensitivity, NIC2 offers the best combination of resolution and sensitivity for our science goals, and also allows more consistent comparisons with the available *HST*/ACS imaging of MD 41 and SINFONI+AO observations of BX 482, which have comparable or better resolution than NIC2.

Each target was observed for four orbits, with each orbit split into four exposures with a subpixel dither pattern to ensure good sampling of the PSF and minimize the impact of hot/cold bad pixels and other such artifacts (e.g., "grot," electronic bars). The individual exposure time was 640 s, giving a total on-source integration time of 10,240 s. The read-out mode employed was the SPARS-64 MULTIACCUM sequence with NSAMP = 12. We used a square four-point dither pattern with a step size of $1\rlap.{''}5375$ (20.5 pixels). We defined the starting positions of each dither sequence as the mid-points of the sides of a $0\rlap.{''}9 \times 0\rlap.{''}45$ rectangle (12 × 6 pixels). Table 2 summarizes the log of the observations.

### 2.4. NICMOS/NIC2 Data Reduction

We started with the pipeline-reduced data products, processed with the STSDAS task *calnica*, version 4.1.1, of the **nicmos** package within the IRAF environment. We refer to the NICMOS Data Handbook[11] for details and the description of specific instrumental features of NICMOS. The steps performed in this stage include bias, zero read signal, and dark current subtraction; data linearization; correction for the so-called electronic bars; flat fielding; and conversion to count rates. The task *calnica* also identifies cosmic ray hits and various bad pixels. These identifications missed on a significant number of obvious bad pixels present in our data, so we extended the bad pixel lists for each exposure as described below.

We then used the task *pedsky* in the same IRAF package to subtract a first-order estimate of the background and the quadrant-dependent residual bias (or "pedestal") in each individual exposure. We subtracted the median value along each column to correct for bias jumps. We constructed a static bad pixel mask for each galaxy based on deviant pixels in the normalized flat field and those identified by *calnica* with bad data quality flags. To identify remaining bad pixels and cosmic rays, we first drizzled the images for each galaxy onto a common finer pixel grid accounting for their relative shifts, the (small) NIC2 distortion, and the static bad pixel masks, using the IRAF task *drizzle* in the STSDAS **analysis** package. A clean reference image was generated by median-combining the registered drizzled images with "minmax" rejection. This image was inverse-drizzled to the original pixel scale and coordinate system of each individual exposure with the task *blot* in the STSDAS **analysis** package. We compared the "blotted" reference images with their corresponding input image and updated the static bad pixel mask to make a mask for each exposure. The background-subtracted exposures were again drizzled, now using the updated individual bad pixel masks, to create the combined drizzled image of each galaxy. For the drizzling, we chose an output pixel scale of $0\rlap.{''}05$, corresponding to that of the SINFONI+AO data of BX 482, and used a square kernel with 0.7 times the size of the input pixels (i.e., a "drop size" of 0.7). We found from experimentation that this combination of parameters gave the best results in terms of preserving the angular resolution and minimizing the impact on the pixel-to-pixel rms noise level of our NIC2 data.

The combined drizzled images showed substantial residual features on scales of a few tens of pixels together with residuals from vignetting at the bottom of the array. These features were successfully modeled and subtracted from the combined images using background maps generated with the SExtractor software, version 2.2.2 (Bertin & Arnouts 1996). Since our science goals require detection of low surface brightness emission of the galaxies to large radii, we took particular care in making these background maps. We masked out sufficiently large areas around each object and then ran SExtractor with a background mesh size of 24 pixels and filter size of three meshes. This combination provided the best match to the spatial frequency of the residual features, without compromising the faint extended emission from the galaxies. Further linear residual features were removed by fitting second-order polynomials (with object masking) along columns and rows. This step also resulted in a small reduction of the pixel-to-pixel rms noise.

Weight maps (for use in the determination of the noise properties and in the structural analysis) were generated in the final combination of the exposures with the task *drizzle*. These

---

[11] http://www.stsci.edu/hst/nicmos/documents/handbooks/DataHandbookv8

reflect the effective total integration time at each output pixel in the drizzling procedure (i.e., accounting for the drop size and the relative size of the input and output pixels as well as the bad pixel and cosmic ray masking). We normalized the weight maps of each galaxy to a maximum of unity. We cropped the final images and weight maps to a region $19\rlap{.}''55 \times 18\rlap{.}''05$ to exclude the edges with relative weight $\lesssim 0.4$.

### 2.5. PSF

For the morphological analysis, accurate knowledge of the PSF in our data is important. We empirically determined the resulting PSF based on stellar profiles in our final reduced images. In total, there are four suitable stars (isolated, sufficiently bright but unsaturated) in three of our NIC2 pointings. Their profiles have a Gaussian core and show Airy wings at larger radii (around $0\rlap{.}''23$). To increase the S/N, we averaged the peak-normalized stellar profiles. From a Gaussian fit to the resulting empirical PSF, the FWHM is $0\rlap{.}''145$ with an ellipticity of 0.08 (or an FWHM of $0\rlap{.}''143$ and an identical ellipticity of 0.08 for a Moffat fit). Relative to the average PSF, the deviations of the radial profiles of the stars are at most 15% (on average $\approx 5\%$) out to a radius of $0\rlap{.}''35$, enclosing 95% of the total flux and where the profiles are at $\approx 1\%$ of the peak value. The curves of growth of the individual stars differ by $<10\%$ (on average $\approx 3\%$) from that of the average PSF. We adopted this empirical average PSF for our analysis.

### 2.6. Noise Properties and Limiting Depths

The quality of the final reduced data is very uniform among our targets. To characterize the effective noise properties, we followed the approach described in detail by Labbé et al. (2003) and Förster Schreiber et al. (2006a). For uncorrelated Gaussian noise, the effective standard deviation from the mean of the background for an aperture of area $A$ is simply the pixel-to-pixel rms $\overline{\sigma}$ scaled by the linear size $N = \sqrt{A}$ of the aperture, $\sigma(N) = N\overline{\sigma}$. However, instrumental features, the data reduction, and the drizzling and combination procedures have added significant systematics and correlated noise in the final data. We thus derived the function $\sigma(N)$ directly from the data by measuring the fluxes of $\approx 240$ non-overlapping circular apertures. We placed the apertures at random in the maps but so as to avoid pixels associated with sources down to S/N $\approx 3$, corresponding to a surface brightness of $\mu(H_{160,AB}) = 23.4$ mag arcsec$^{-2}$. Series of measurements were repeated with different aperture diameters ranging from $0\rlap{.}''1$ to $1''$.

For each aperture size, the distribution of fluxes is symmetric around the background value (about 0), and is well reproduced with a Gaussian profile. We determined the background rms variations from the width of the best-fit Gaussian to the observed distribution for each aperture size. While at any fixed spatial scale, the noise properties over the images are consistent with being Gaussian, the variations with $N$ deviate appreciably from the scaling expected for Gaussian noise, being systematically larger and increasing nonlinearly. The real noise behavior in our NIC2 images can be approximated by the polynomial model:

$$\sigma(N) = \frac{N\,\overline{\sigma}\,(a + b\,N)}{\sqrt{w}}, \tag{1}$$

where the weight term $1/\sqrt{w}$ accounts for the spatial variations in the noise level related to the exposure time and is taken from the weight maps. The coefficient $a$ represents the effects

of correlated noise, which are dominated by the resampling of the images to the final pixel scale through the drizzling procedure. The curvature in the $\sigma(N)$ relation quantified by the coefficient $b$ indicates a noise contribution that becomes increasingly important on larger scales. For our data, this probably originates mostly from instrumental features, and residuals from the background subtraction and flat fielding. Qualitatively, the same second-order polynomial behavior is seen in ground- and space-based optical and near-IR imaging data analyzed by Labbé et al. (2003, their Figure 4), Förster Schreiber et al. (2006a, their Figure 6), and Wuyts et al. (2008, their Figure 3).

The noise properties are very similar in all NIC2 maps. The derived pixel-to-pixel rms values are identical within 3%. The mean and standard deviation of the best-fit polynomial coefficients among the six images are 1.20 and 0.15 for $a$ and 0.039 and 0.017 for $b$. Limiting magnitudes and photometric uncertainties from our NIC2 data are computed through Equation (1) for the corresponding aperture size. The effective $3\sigma$ magnitude limits in a "point-source aperture" with diameter $d = 1.5 \times$ FWHM $= 0\rlap{.}''22$ (maximizing the S/N of photometric measurements in unweighted circular apertures of point-like sources) are $\approx 28.1$ mag (see Table 2).

## 3. GLOBAL PROPERTIES OF THE GALAXIES

### 3.1. General Appearance of the NIC2 Images

Figure 1 presents the final reduced NIC2 images at a sampling of $0\rlap{.}''05$ pixel$^{-1}$. The angular resolution from the effective PSF with FWHM $= 0\rlap{.}''145$ corresponds to a spatial resolution of 1.2 kpc at the median $z = 2.2$ of the targets. We computed the geometric center as the unweighted average of the $x$ and $y$ coordinates of pixels with S/N $> 3$. Emission from the galaxies is detected out to radii of $0\rlap{.}''8$–$1\rlap{.}''2$, or 6.5–10 kpc. The averaged surface brightness of the sources over the emitting regions (with S/N $> 3$) is in the range $\mu(H_{160,AB}) = 22.6$–23.0 mag arcsec$^{-2}$, with typical S/N $= 4$–6 per pixel.

The spatial distribution of the $H_{160}$-band light in the images is characterized by a diffuse and low surface brightness component over which rich, brighter substructure is superposed. The most prominent features are the bright and compact regions, seen in all galaxies; each of the non-AGN disks contains several such clumps. BX 663 exhibits a bright central peak, and only one other and comparatively fainter clump to the southeast (SE); since the rest-UV and optical emission lines of this object indicate the presence of a Type 2 AGN, the compact central $H_{160}$-band peak may not be dominated by AGN emission and could trace in large part stellar continuum light. Detailed modeling of the optical to mid-IR SED of this galaxy will help to place constraints on the contribution of the stars and AGN (K. Hainline et al. 2011, in preparation). In BX 528, the merger components are clearly separated in our NIC2 image, with a projected distance of $\approx 8$ kpc between the compact northwestern and the more extended southeastern parts (hereafter BX 528$-$NW and BX 528$-$SE) and significant emission along a "bridge" between the two components. The fainter source $\approx 1\rlap{.}''8$ to the northeast is undetected in our SINFONI data so that its association with BX 528 is unclear. Likewise for the source $\approx 2''$ south of BX 482, which could also result from chance alignment. In contrast, the small source $\approx 0\rlap{.}''6$ south of the main body of BX 389 corresponds to an extension in our seeing-limited H$\alpha$ maps (with about three times coarser resolution) and is thus likely to be a small satellite at the same redshift and projected distance of
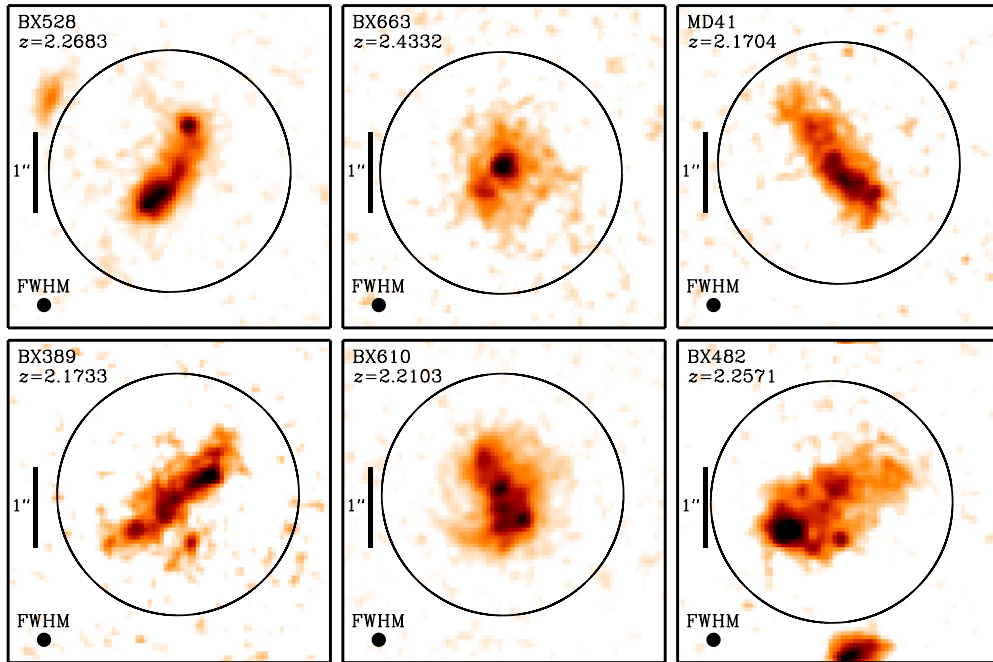
**Figure 1.** *HST* NICMOS/NIC2 $H_{160}$ maps of the galaxies, probing the broadband emission around rest-frame 5000 Å. The target name and Hα redshift are labeled in the top corner of each panel. The color coding scales linearly with flux density from white to black for the minimum to maximum levels displayed (varying for each galaxy). The FWHM of the effective PSF is indicated by the filled circle at the bottom left of each corner; the angular resolution is $0\farcs145$, or $\approx 1.2$ kpc at the median $z = 2.2$ of the sources. The angular scale of the images is shown with the $1''$ long vertical bar next to each galaxy. The black solid circle overlaid on each map shows the aperture used to extract the integrated $H_{160}$-band flux density (diameter of $3''$). In all maps, north is up and east is to the left.

(A color version of this figure is available in the online journal.)

5 kpc (hereafter "BX 389−S"; see Sections 4 and 7). No other source is detected in the NIC2 images within $\approx 2''$ or projected $\approx 15$ kpc of our primary targets; this area corresponds to the deeper part of the SINFONI data, where we can search for line emission to faint levels of candidate companions to determine a physical association.

Other characteristics of note include the broad curved features reminiscent of spiral arms seen in the outer isophotes of BX 610, on the northwest (NW) and southeast sides. In addition, the inner isophotes in this galaxy show a significant and systematic increase in ellipticity and change in position angle (P.A.). From fitting elliptical isophotes to the NIC2 image using the task *ellipse* in IRAF, the apparent (uncorrected for beam smearing) ellipticity and P.A. vary from $\sim 0.8$ and $\sim 35°$ at radii $r \lesssim 0\farcs5$ (or 4 kpc) to $\sim 0.1$ and $\sim 0°$ at $r \sim 1''$ (8 kpc). The interpretation of the inner isophotal feature is complicated by the presence of the clumps, which are mostly aligned along a similar P.A., but it is suggestive of a bar-like structure as seen in local barred spirals.

### 3.2. Photometric Properties

The new $H_{160}$-band photometry from our *HST*/NICMOS data constitutes a significant addition to that available for our targets, especially for BX 482 without any previous near-IR imaging and MD 41 for which the existing $K$-band data are fairly shallow. Published data include ground-based optical $U_n G \mathcal{R}$ imaging for all sources, and near-IR $J K_s$ imaging for a subset, presented by Erb et al. (2006; see also Steidel et al. 2004). The photometry was measured in matched isophotal apertures determined from the $\mathcal{R}$-band images and corrected to "total" magnitudes in elliptical apertures scaled based on the first moment of the $\mathcal{R}$-band light profiles (Steidel et al. 2003). *Spitzer*/IRAC mid-IR photometry has subsequently been obtained for all objects

except BX 482 (Reddy et al. 2010). To construct the broadband SEDs and derive the global stellar and extinction properties of our targets, we however excluded the IRAC data for the following reasons. The optical and near-IR photometry provides the most uniform data sets among the six galaxies in terms of wavelength coverage whereas of the five objects with IRAC data, only three were observed in all four channels. Moreover, contamination by AGN emission in BX 663 and BX 610 becomes important at the longer wavelengths probed by IRAC and would affect the modeling results.

To include the $H_{160}$ band in the SEDs of our targets, we measured the total magnitude in a circular aperture of diameter $3''$ on the NIC2 images (indicated in Figure 1). Because of the small NIC2 field of view, the accuracy of the measurements in the $\mathcal{R}$-band isophotal aperture used for the ground-based photometry on the PSF-matched $H_{160}$-band images is compromised by the difficulty of determining the local background sufficiently reliably: the area empty of sources signal after convolving to the optical seeing of $\sim 1''$ is too small. The median difference between the total magnitudes based on the fixed circular aperture measurement on unconvolved NIC2 maps and that in the isophotal apertures on PSF-matched NIC2 maps is $-0.16$ mag, with the maximum for BX 389 ($-0.51$ mag) and best agreement for BX 528 ($-0.002$ mag). The photometry is given in Table 1 and the optical/near-IR SEDs are plotted in Figure 2.

By their primary selection, all targets satisfy the $U_n G \mathcal{R}$ color criteria of "BX" or "MD" objects (Adelberger et al. 2004; Steidel et al. 2004). Synthetic broadband colors measured on the spectrum of the best-fitting stellar population model to the observed SEDs (described in Section 3.3 below) suggest that all targets would also satisfy the $BzK = (z - K)_{AB} - (B - z)_{AB} > -0.2$ mag criterion of $z > 1.4$ "star-forming $BzK$ objects"
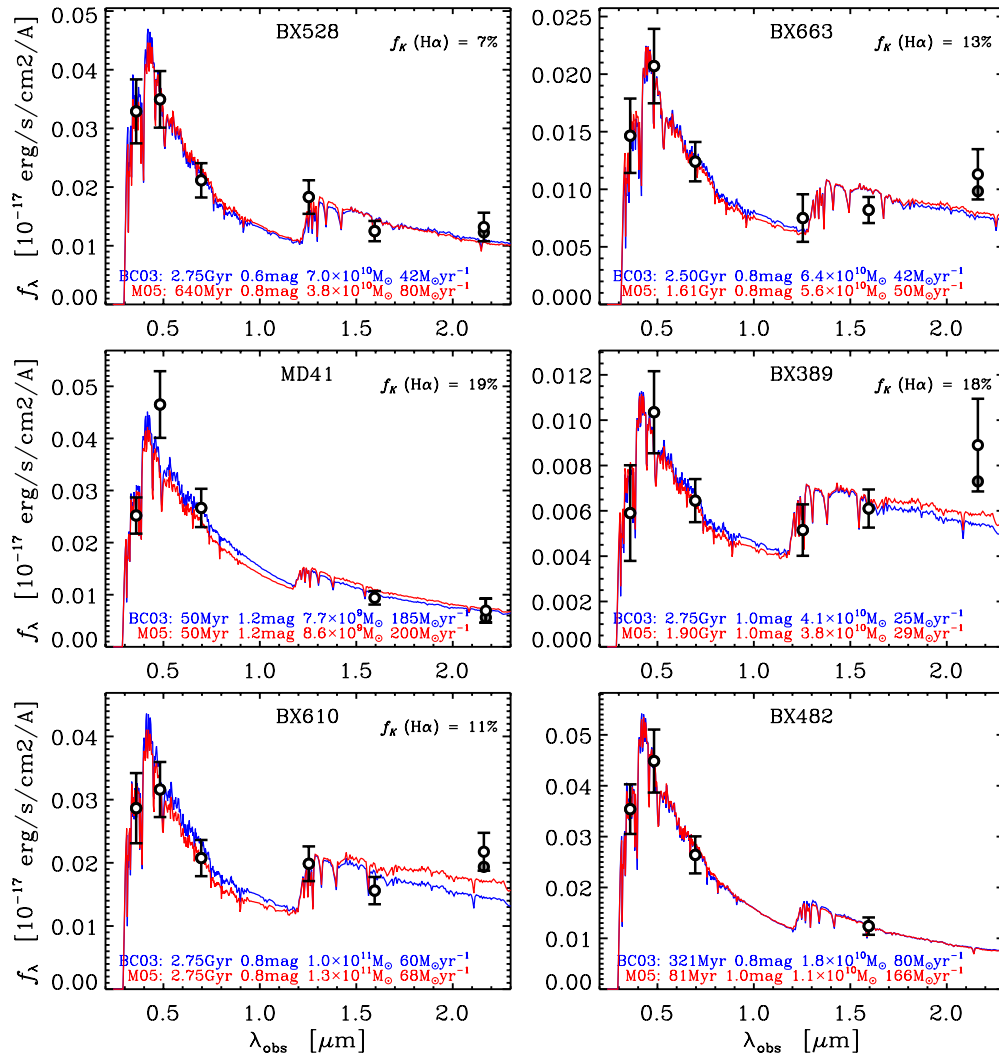
**Figure 2.** Broadband optical to near-IR SEDs of the galaxies, including the $H_{160}$ flux density measured from the NIC2 data presented in this paper. The large white-filled circles and error bars represent the observed photometry and $1\sigma$ uncertainties (Table 1). The gray-filled circle shows the $K$-band flux density corrected for the contribution by the H$\alpha$ line emission, estimated from the available SINFONI data and given explicitly in each panel. The solid lines show the synthetic spectrum of the best-fitting stellar population model, assuming a constant star formation rate, solar metallicity, the Calzetti et al. (2000) reddening law, and the Chabrier (2003) or Kroupa (2001) IMF, obtained with the Bruzual & Charlot (2003) and Maraston (2005) models (blue and red lines, respectively). The best-fit age, $A_V$, stellar mass, and SFR for each galaxy and synthesis code are listed in each panel.

(A color version of this figure is available in the online journal.)

introduced by Daddi et al. (2004). In addition, two of the four sources with both $J$ and $K$ photometry (BX 663 and BX 389) have the red $(J - K_s)_{AB} > 1.34$ colors of "Distant Red Galaxies" (DRGs; Franx et al. 2003; van Dokkum et al. 2004), and one (BX 610, $(J - K_s)_{AB} = 1.28$ mag) is within $0.3\sigma$ of the DRG criterion. For these three sources and for BX 528, the photometry is consistent with the presence of a significant population of evolved stars along with the young stars producing the blue rest-UV SED. The best-fit models to the SEDs of these four objects imply rest-frame $(U - B)_{AB} \approx 0.75$–0.9 mag colors, close to or just at the separation adopted by, e.g., Kriek et al. (2009), between "red" and "blue" objects. In contrast, MD 41 and BX 482 are significantly bluer with rest-frame $(U - B)_{AB} \approx 0.5$ mag.

Our NIC2 sample is relatively bright in the near-IR; the five targets with $K$-band imaging have a median $K_{s,AB} = 21.8$ mag and span a range of $\approx 1.2$ mag in the observed $K$ band ($K_{s,AB} = 21.1$–22.3 mag) as well as in the rest-frame absolute $V$-band magnitude (as derived from the SED modeling below,

with $M_{V,AB}$ between $-23.1$ and $-21.9$ mag). In addition, the *Spitzer*/MIPS 24 $\mu$m measurements available for four of the targets (BX 389, BX 610, BX 528, and BX 663) indicate that they are among the brightest 3% of rest-UV-selected $z \sim 2$ galaxies, in terms of rest-frame 8 $\mu$m luminosity (Reddy et al. 2010).

### 3.3. SED Modeling and Stellar Properties

Stellar population synthesis modeling of BX 528, BX 663, BX 389, and BX 610 was first presented by Erb et al. (2006). The new $H_{160}$ photometry from NIC2 and $K$-band flux for MD 41 provide additional constraints and allow us to extend the SED modeling to BX 482 and MD 41, which had previously only three optical data points. For consistently derived stellar and dust extinction properties within our sample, we re-modeled the optical/near-IR SEDs of all six objects.[12] We followed standard

---

[12] We verified that the SED modeling results are essentially unchanged when including the available IRAC photometry for the three targets without AGN contribution to their mid-IR SED.

**Table 3**
Stellar and Dust Properties of the Galaxies

| Object | Age (Myr) | $A_V$ (mag) | $M_\star$ $(10^{10}\,M_\odot)$ | $M_{V,\,AB}$[a] (mag) | SFR $(M_\odot\,\mathrm{yr}^{-1})$ | sSFR[b] $(\mathrm{Gyr}^{-1})$ |
|---|---|---|---|---|---|---|
| Q1623 − BX528 | $2750^{+96}_{-2110}$ | $0.6 \pm 0.2$ | $6.95^{+0.17}_{-3.61}$ | $-22.90^{+0.04}_{-0.12}$ | $42^{+29}_{-16}$ | $0.6^{+1.7}_{-0.1}$ |
| Q1623 − BX663 | $2500^{+147}_{-800}$ | $0.8 \pm 0.2$ | $6.40^{+0.22}_{-2.28}$ | $-22.68^{+0.05}_{-0.20}$ | $42^{+13}_{-12}$ | $0.7^{+0.3}_{-0.2}$ |
| SSA22a − MD41 | $50^{+31}_{-0}$ | $1.2 \pm 0.2$ | $0.77^{+0.10}_{-0.03}$ | $-22.37^{+0.04}_{-0.09}$ | $185^{+3}_{-70}$ | $24^{+1}_{-9}$ |
| Q2343 − BX389 | $2750^{+224}_{-1945}$ | $1.0 \pm 0.2$ | $4.12^{+0.77}_{-2.16}$ | $-21.94^{+0.09}_{-0.13}$ | $25^{+17}_{-2}$ | $0.6^{+1.2}_{-0.1}$ |
| Q2343 − BX610 | $2750^{+173}_{-650}$ | $0.8 \pm 0.2$ | $10.0^{+2.7}_{-0.6}$ | $-23.10^{+0.12}_{-0.04}$ | $60^{+26}_{-1}$ | $0.6 \pm 0.2$ |
| Q2346 − BX482 | $321^{+485}_{-141}$ | $0.8 \pm 0.2$ | $1.84^{+0.79}_{-0.46}$ | $-22.65^{+0.07}_{-0.08}$ | $80^{+42}_{-32}$ | $4.3^{+3.0}_{-2.5}$ |

**Notes.** Results from SED modeling of the optical and near-IR photometry, with best-fitting star formation history having a constant SFR for all targets. The formal (random) fitting uncertainties are given, derived from the 68% confidence intervals based on 200 Monte Carlo simulations for the default set of Bruzual & Charlot (2003) models with solar metallicity, a Chabrier (2003) IMF, and the Calzetti et al. (2000) reddening law; systematic uncertainties (from SED modeling assumptions) are estimated to be typically a factor of ∼1.5 for the stellar masses, ±0.3 mag for the extinctions, and factors of ∼2–3 for the ages as well as for the absolute and specific star formation rates.
[a] Rest-frame absolute *V*-band magnitude, uncorrected for extinction.
[b] Specific star formation rate, i.e., the ratio of the star formation rate over stellar mass.

procedures (e.g., Shapley et al. 2001; Erb et al. 2006; Förster Schreiber et al. 2006a), exploring also a range of parameters and model ingredients to assess possible systematics from the assumptions adopted. Our specific procedure is described in detail by Förster Schreiber et al. (2009) and is summarized here.

We used the stellar evolutionary code from Bruzual & Charlot (2003). The age, extinction, and luminosity scaling of the synthetic model SED were the free parameters in the fits. The ages were allowed to vary between 50 Myr and the age of the universe at the redshift of the source. The lower limit is set to avoid implausibly young solutions and corresponds approximately to the dynamical timescale $\tau_{\rm dyn} = r/v$ from the inclination-corrected velocity $v$ at a radius of $r \sim 10$ kpc of the galaxies (e.g., Förster Schreiber et al. 2006b; Genzel et al. 2008). We employed the Chabrier (2003) IMF and the reddening curve of Calzetti et al. (2000) and assumed a solar metallicity. We fixed the star formation history (SFH), adopting a constant star formation (CSF) rate model, which we found appropriate for most galaxies (see below, and also Erb et al. 2006). We derived the formal (random) uncertainties on the best-fit parameters from 200 Monte Carlo simulations, where we varied the input photometry assuming a Gaussian probability distribution for the measurements uncertainties (see Section 2.6). To explore the impact of model assumptions and ingredients, we also used the evolutionary synthesis code of Maraston (2005) and ran suites of models with exponentially declining SFRs with *e*-folding timescales $\tau$ between 10 Myr and 1 Gyr, with a metallicity of 1/5 and 2.5 times solar, and with extinction laws appropriate for the Small Magellanic Cloud (Prévot et al. 1984; Bouchet et al. 1985) and the Milky Way (Allen 1976).

Table 3 lists the best-fit properties for our adopted set of Bruzual & Charlot (2003) models with CSF, solar metallicity, and Calzetti et al. (2000) law along with the formal uncertainties taken as the 68% confidence intervals from the Monte Carlo simulations around the best-fit values. Figure 2 shows the corresponding synthetic model spectra; best-fit Maraston (2005) models for the same CSF, metallicity, and reddening law are also shown for comparison. To gauge systematic uncertainties, we looked at the variations in derived properties for the other suites of model assumptions and synthesis code considered. For individual galaxies, and compared to the adopted properties, the median of the variations is as follows: the ages are mostly

younger by a factor of ≈2, the extinction in *V* band $A_V$ decrease by ≈0.2 mag, the stellar masses $M_\star$ tend to be lower by a factor of ≈1.5, the absolute and specific SFRs tend to decrease by factors of ≈2. The overall sense of these variations reflects in part the fact that, by construction, CSF models generally lead to older ages than declining SFHs. While the systematic uncertainties above are significant, the derived properties of the galaxies are robust in a relative sense. In particular, MD 41 and BX 482 remain the youngest and least massive of the sample in any case.

Our choice of CSF is obviously very simplistic. For the range of SFHs above, we find that the longest timescales ($\tau = 1$ Gyr or CSF) are favored (in a minimum $\chi^2$ sense) for four out of six galaxies. MD 41 and BX 482, with bluest SEDs, have best fits formally obtained for models with $\tau \lesssim 50$ Myr but the age, $M_\star$, and SFR are within $3\sigma$ or less of the values for CSF. Recent work has emphasized the fact that declining SFHs may well be inappropriate for high $z$ star-forming galaxies (Renzini 2009; Maraston et al. 2010). Our exploration of constant and declining SFHs was motivated by continuity with previous work and consistency with the SED modeling assumptions for the comparison samples discussed in Section 6.

We did not account for emission line contribution in our SED modeling. The main contribution expected for our sample is from Hα in the *K* band, and these are in the range 7%–19% (with a median of 13%) based on our SINFONI *K*-band observations (see also Erb et al. 2006). The median [N II] $\lambda 6584$/Hα ratio is 0.23 (with highest ratio 0.43 for BX 610). SINFONI *H*-band data are available for five targets; the [O III] doublet and Hβ are all detected in two cases and their contributions to the $H_{160}$ flux densities are smaller than for Hα in *K*, and $3\sigma$ upper limits for the others are at most 29% (see Section 5). The Hα-corrected *K*-band flux densities are indicated in Figure 2; the impact on the SED modeling results is not significant in view of the other uncertainties involved.

Our targets span over an order of magnitude in stellar mass, from $7.7 \times 10^9$ to $1.0 \times 10^{11}\,M_\odot$ with median $5.3 \times 10^{10}\,M_\odot$. The stellar populations that dominate their rest-UV to optical SEDs cover the full range allowed in our modeling (from 50 Myr to 2.75 Gyr), and are moderately obscured (with $A_V$ between 0.6 and 1.2 mag, or equivalently $E(B - V) = 0.15$–$0.30$ mag). Four of the six targets have in fact ages consistent with the age of the universe at their redshift, indicating the presence of mature
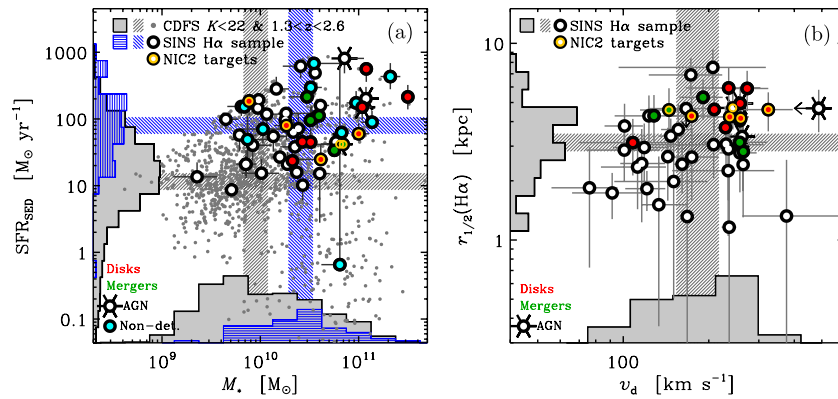
**Figure 3.** Stellar and dynamical properties of the galaxies observed with NIC2. The data points for the NIC2 targets are indicated with yellow, and the data for the comparison samples are taken from Förster Schreiber et al. (2009). (a) Stellar mass and star formation rate derived from SED modeling, compared to those of the SINS Hα sample at $1.3 < z < 2.6$ and of $K$-selected galaxies from the CDFS (Wuyts et al. 2008) in the same redshift interval and at $K_s < 22.0$ mag (the magnitude of the faintest of the SINS Hα sample galaxies in the $K$ band). The SINS data points are shown with large filled dots, their projected distribution onto each axis with blue-hatched histograms, and their median magnitudes as blue-hatched horizontal bars. The CDFS data are plotted with small gray dots, gray-filled histograms, and gray-hatched bars. The histograms are arbitrarily normalized. The galaxies classified as disk-like and merger-like by kinemetry (Shapiro et al. 2008) are plotted as red- and green-filled circles. Sources that were known to host an AGN based on optical (rest-UV) or previous long-slit near-IR (rest-frame optical) spectroscopy are indicated with a six-pointed skeletal star. SINS targets that were not detected in Hα line emission are marked as cyan-filled circles. (b) Half-light radius and circular velocity $v_d$ derived from the SINFONI Hα observations, compared to those of the entire SINS Hα sample. The color scheme for data points is the same as for the left panel, and the projected distributions and median values for the SINS Hα sample are shown with the gray histograms and gray-hatched bars. The NIC2 sample spans roughly an order of magnitude in stellar mass and SFR, and lies at the high end of the distribution of Hα sizes and circular velocities inferred for the SINS Hα sample.

(A color version of this figure is available in the online journal.)

stellar populations. The median absolute and specific SFRs are $\approx 50\ M_\odot\ \mathrm{yr}^{-1}$ and 0.6 Gyr$^{-1}$ (with ranges of 25–185 $M_\odot\ \mathrm{yr}^{-1}$ and 0.6–24 Gyr$^{-1}$). Figure 3(a) compares our NIC2 sample in the $M_\star - $ SFR plane with the full SINS Hα sample, and a purely $K$-selected sample taken from the Chandra Deep Field South (CDFS) in the same $z = $ 1.3–2.6 interval and to the same $K_{s,\mathrm{Vega}} = 22$ mag limit as the SINS sample (Förster Schreiber et al. 2009 and also Wuyts et al. 2008). The properties of these comparison samples were derived using the same SED fitting procedure and model assumptions as for the NIC2 sample. Clearly, and by selection, our NIC2 galaxies probe the actively star-forming part of the $z \sim 2$ galaxy population (see also discussions by Erb et al. 2006; Förster Schreiber et al. 2009). Their median stellar mass and SFR are comparable to those of the SINS Hα sample ($\approx 3 \times 10^{10}\ M_\odot$ and $\approx 70\ M_\odot\ \mathrm{yr}^{-1}$).

### 3.4. Hα and Kinematic Properties

If our targets do not particularly stand out in terms of their stellar properties compared to the SINS Hα sample, they do more so in terms of their Hα brightness and kinematics. This distinction arises because, as described in Section 2, we chose them among the sources with highest S/N and spatially best-resolved Hα emission from our seeing-limited SINFONI data sets. Five of them were explicitly selected because of their disk-like kinematics, and BX 528 because it shows in contrast kinematic signatures expected for counterrotating mergers. The spatial extent and brightness of our targets make them particularly well suited for a detailed study of morphologies and reliable assessment of structural parameters from sensitive kpc-resolution continuum imaging.

Figure 3(b) compares the NIC2 galaxies with the SINS Hα sample in the velocity–size plane, with the half-light radii and (inclination-corrected) circular velocities derived from Hα (Genzel et al. 2008; Cresci et al. 2009; Förster Schreiber et al. 2009). The NIC2 targets lie at the high end of the $v_d - r_{1/2}(\mathrm{H}\alpha)$ distribution. With $r_{1/2}(\mathrm{H}\alpha) \approx$ 4–5 kpc, they are all larger than the median of 3.1 kpc for the SINS Hα sample. The $v_d$ for the

disks are roughly equal to or larger than the median for SINS galaxies of $\approx 180$ km s$^{-1}$, and up to $\sim 300$ km s$^{-1}$. For the merger BX 528, the velocity gradient is lower and leads to a lower equivalent $v_d$ of 145 km s$^{-1}$ (see Förster Schreiber et al. 2009). The ratios of circular velocity to intrinsic local velocity dispersion of the disks are in the range $v_d/\sigma_0 \approx$ 2–6, which is significantly lower than for local spiral galaxies (values in the range $\sim$10–40; e.g., Dib et al. 2006; Épinat et al. 2010) and suggests comparatively larger gas turbulence and geometrical thickness. These low $v_d/\sigma_0$ ratios appear to be a characteristic feature of early disk galaxies at $z \sim$ 1–3 (e.g., Förster Schreiber et al. 2006b; Wright et al. 2007; Genzel et al. 2008; Stark et al. 2008; Cresci et al. 2009; Épinat et al. 2009).

The median integrated Hα flux of the NIC2 targets (uncorrected for extinction) is $F(\mathrm{H}\alpha) = 1.9 \times 10^{-16}$ erg s$^{-1}$ cm$^{-2}$ (and range from 1.1 to $3.1 \times 10^{-16}$ erg s$^{-1}$ cm$^{-2}$). This places them among the brighter half of the SINS Hα sample (with median $F(\mathrm{H}\alpha) = 1.1 \times 10^{-16}$ erg s$^{-1}$ cm$^{-2}$). In terms of integrated Hα line widths, their median is $\sigma(\mathrm{H}\alpha) = 155$ km s$^{-1}$ (spanning the range 120–245 km s$^{-1}$), somewhat broader than the median for the SINS Hα sample (130 km s$^{-1}$). This difference is due in part to the large observed velocity gradients for the sources.

## 4. ANALYSIS OF THE REST-FRAME OPTICAL MORPHOLOGIES

### 4.1. Parametric Analysis of the Galaxies' Structure

#### 4.1.1. Methodology

In a first step to characterize quantitatively the morphologies of our galaxies, we followed a parametric approach. The main goal here is to derive the global structural parameters of the sources. We used the code GALFIT (Peng et al. 2002) to fit the two-dimensional surface brightness distributions with a Sérsic (1968) profile:

$$I(r) = I(0) \exp[-b_n\,(r/R_e)^{1/n}], \qquad (2)$$

where $I$ is the intensity as a function of radius $r$, $b_n$ is a normalization constant, and $R_e$ is the effective radius enclosing half of the total light of the model. In this parameterization, ellipticals with de Vaucouleurs profiles have a Sérsic index $n = 4$, exponential disks have $n = 1$, and Gaussians have $n = 0.5$. In the fitting procedure, GALFIT convolves the model light distribution to the effective resolution of the data and determines the best fit based on $\chi^2$ minimization. We input our empirically determined PSF and the weight maps scaled by the pixel-to-pixel rms measured on the reduced images (see Section 2). To reduce the impact of large-scale residuals from flat fielding and background subtraction (Section 2.6), we performed the fits within a region $7'' \times 7''$ centered on the sources.

The free parameters in the fits were the Sérsic index ($n$), the effective radius ($R_e$), the axis ratio ($b/a$, semiminor over semimajor axis radii), the P.A. of the major axis, and the total magnitude. Given that surface brightness fitting of faint galaxies is sensitive to the background determination and that Sérsic profile parameters tend to be degenerate with the "sky" value (see, e.g., Peng et al. 2002; van Dokkum et al. 2008), we fixed the sky level $S$ in our fits. Moreover, asymmetric and clumpy surface brightness distributions can strongly bias the results, so we also fixed the coordinates $x_0$ and $y_0$ of the center position. In order to derive realistic uncertainties, we performed a series of fits where these fixed parameters were drawn at random from plausible distributions. Specifically, for every galaxy we ran GALFIT 500 times, each time varying the $x_0$ and $y_0$ according to a uniform distribution within a squared box of $2 \times 2$ pixels around the geometric center as defined in Section 3.1, which corresponds closely to the dynamical center of our targets. For the background, the fixed input $S$ values were drawn at random from the central 10% of the distribution of individual pixel values in the regions empty of sources (with this range reflecting the uncertainty in the background level). The best-fit parameters were taken as the median of the results for all 500 runs, and the $1\sigma$ uncertainties as the 68% confidence intervals about the median.

We performed additional series of fits to explore systematics from the center and sky background determinations. In all cases, the initial guesses for the center and sky values were generated as described above. In the first two series, one of the sky or center was chosen as a free parameter and the other was fixed. In a third series, both parameters were free. For BX 663, MD 41, BX 389, and BX 610, the best-fit structural parameters for these additional series are all within the 68% confidence intervals of the results for the first series with sky and center fixed to the randomly drawn values in each iteration. For BX 528 and BX 482, the two series with the free center position lead to significantly different results as expected from their particularly asymmetric morphologies, with changes in $R_e$ and $n$ by $\gtrsim 2\sigma$.

For the interacting system BX 528, single component fits are clearly inappropriate. When the center is free to vary, the fits are heavily influenced by the brighter BX 528−SE component: the best-fit center moves toward this component, the Sérsic index increases to match the steeper inner profile and the $R_e$ also increases. For this system, we thus also ran a series fitting two Sérsic profiles simultaneously, fixing the respective center position and sky to random values drawn from appropriate distributions as explained above. Likewise, we performed two-component fits for BX 389 to derive the structural parameters of the small southern companion BX 389−S. The best-fit parameters for the main part of BX 389 are almost identical to those obtained with the single-component fits. For BX 482,

the large and bright clump on the southeast side (which makes up $\approx 15\%$ of the total light after subtracting the "background" light from the host galaxy; see Paper II) drives the center in this direction when allowed as a free parameter, and leads to a somewhat higher best-fit $n$ index. At the same time, because the northwest side of the galaxy is overall fainter and lacks bright small-scale features, the best-fit $R_e$ is smaller. We did not consider two-component fits for BX 482 because the kinematics as well as morphologies are more consistent with a single system.

### 4.1.2. Results for the NIC2 Targets

Table 4 gives the results for the main structural parameters, $R_e$, $n$, $b/a$, and P.A., of our targets from the single-component fits as well as from the two-component fits for BX 528 and BX 389. In Figure 4, the first two columns show the best-fit values for single-component fits along with the distributions obtained from the 500 GALFIT runs in each parameter. In the third column, ellipses are drawn on the NIC2 images showing the effective radius, axis ratio, and P.A. of the best-fit models. The fourth column shows the fit residuals, revealing the clumpy structure and large scale asymmetries in the light distributions. Figure 5 shows the same but for the two-component fits to BX 528 and BX 389. Figure 6 compares the radial light profiles of the galaxies' data and of the best-fit model (here using the two-component model for BX 528). The profiles correspond to the average along ellipses centered on the best-fit $x_0$ and $y_0$ position, and with best-fit axis ratio and P.A. of the single-component models. This tends to smooth out the small-scale structure and asymmetric features of the surface brightness distributions; the detailed substructure will be considered in the next subsection.

All of our targets qualify as morphologically late-type, disk-dominated systems, often defined as having $n < 2$–2.5 (e.g., Bell et al. 2004; Trujillo et al. 2006). The only exceptions are BX 528−NW and BX 389−S that have $n \approx 3$ but the large uncertainties make them within $1\sigma$ of the above criterion. A remarkable feature of the four non-AGN galaxies with disk-like H$\alpha$ kinematics is their shallow inner light profiles. With Sérsic indices in the range $\approx 0.15$–0.6, these are significantly less centrally concentrated than exponential disks (by definition $n = 1$). The residuals are overall smallest for MD 41 and BX 389, the two most edge-on disks based on their axis ratios ($b/a \approx 0.30$) from the fits to the $H_{160}$-band images as well as from their H$\alpha$ morphologies and kinematics (Förster Schreiber et al. 2006b; Genzel et al. 2008; Cresci et al. 2009). The spiral-like features in BX 610 noted in Section 3.1 are most obvious in the outer parts beyond the effective radius. The residuals for the single- and double-component fits to BX 528 indicate that neither case provides a very good representation. There is clearly significant light emitted along the "bridge" between the SE and NW components.

BX 663 has the highest $n$ index among our sample, reflecting the fairly prominent central peak and shallower profile of the extended emission at larger radii. We explored two-component models, meant to represent the case of a disk + bulge and of a disk + unresolved nuclear source. A free $n$ component was considered for the disk, and the second component was taken as either a de Vaucouleurs profile with fixed $n = 4$ or as the empirically determined PSF. Because the central peak is accounted for by the $n = 4$ or PSF component, the underlying disk ends up with low $n$ of 0.24 (disk + bulge) or 0.63 (disk + unresolved source), in the range obtained for the other five SINS targets. The disk $R_e$ values, however, differ by 10% or less ($<2.5\sigma$) from the
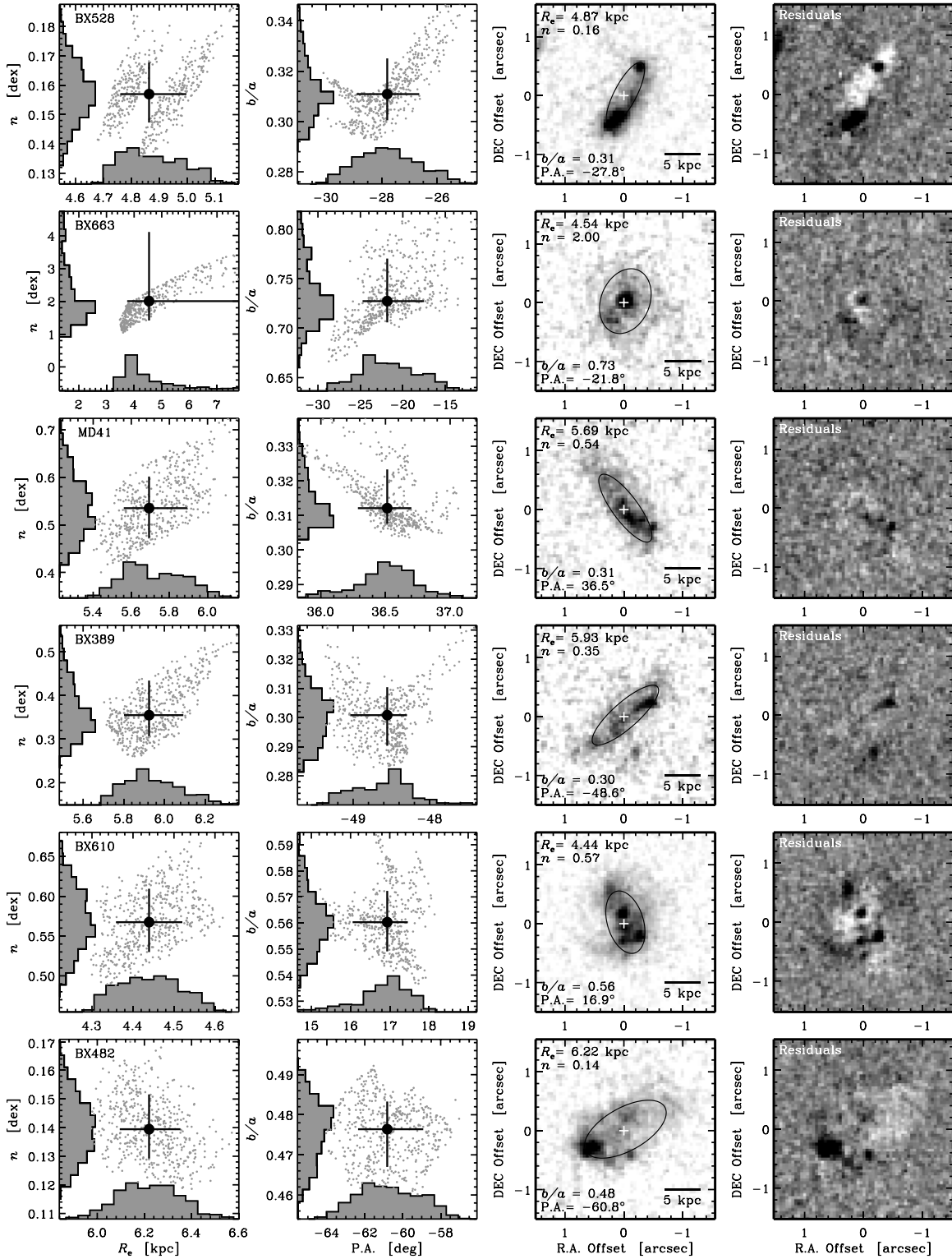
**Figure 4.** Results of parametric fits to the two-dimensional $H_{160}$-band surface brightness distribution of our NIC2 sample. The structural parameters (effective radius $R_e$, Sérsic index $n$, axis ratio $b/a$, and position angle P.A.) were derived from a series of 500 single-component Sérsic model fits, as described in Section 4.1.1. Each row shows the results for a given galaxy, with panels as follows. Far left: $n$ vs. $R_e$, where small gray dots show the results of the 500 iterations, histograms correspond to the projected distributions onto each axis, and the large black dot and error bars indicate the median and 68% confidence intervals adopted as best-fit parameters and $1\sigma$ uncertainties. Middle left: same as the far left panel but for $b/a$ vs. P.A. Middle right: NIC2 images with overplotted ellipse of center, semimajor axis, axis ratio, and orientation equal to the adopted best-fit position, $R_e$, $b/a$, and P.A. Far right: residual map obtained by subtracting the NIC2 image with the Sérsic model with best-fit parameters. All images are plotted with a linear intensity gray scale (with negative to positive residuals ranging from white to black).

best-fit single-component $R_e$. For the disk + bulge case, the de Vaucouleurs component has $R_e = 2.47^{+5.03}_{-0.95}$ kpc. In terms of $\chi^2$ values and of residuals, the best-fit two-component models

are indistinguishable from the best-fit single Sérsic model, so we consider only the single-component model for BX 663 throughout this paper.
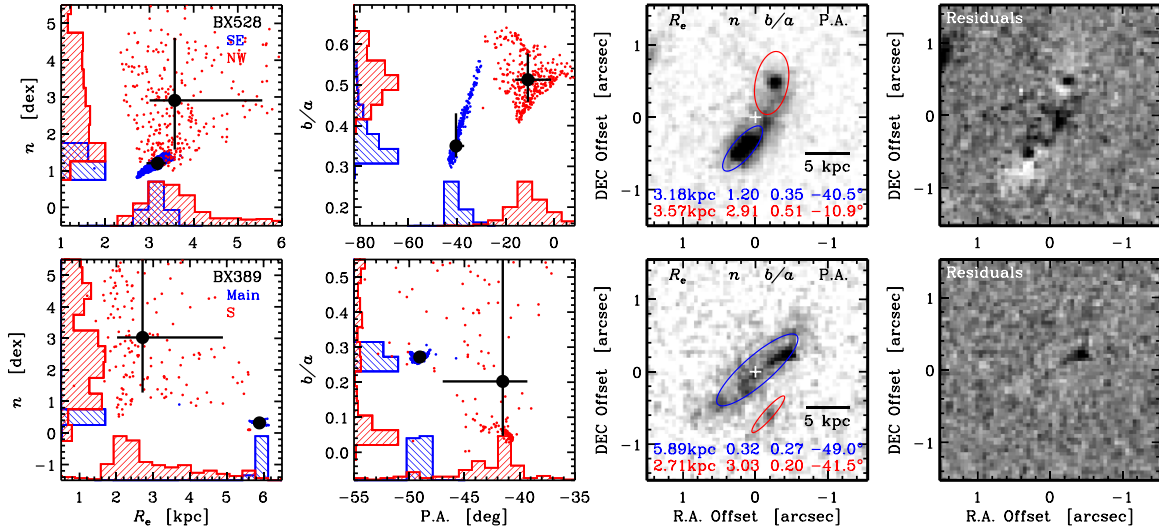
**Figure 5.** Same as Figure 4 for the two-component Sérsic fits for BX 528 and BX 389. In the first three panels to the left and for BX 528, blue and red colors correspond to the results for the southeast and northwest components, respectively. For BX 389, blue is used for the main part of the galaxy and red for the small southern companion.

(A color version of this figure is available in the online journal.)

**Table 4**
Best-fit Structural Parameters from the NIC2 $H_{160}$-band Images

| Object | $R_e$ (kpc) | $n$ | $b/a$ | P.A. (deg) |
|---|---|---|---|---|
| | Single-component models | | | |
| Q1623 − BX528 | $4.86^{+0.13}_{-0.10}$ | $0.16 \pm 0.01$ | $0.31 \pm 0.01$ | $-27.8^{+1.2}_{-1.1}$ |
| Q1623 − BX663 | $4.54^{+7.71}_{-0.79}$ | $2.00^{+2.11}_{-0.59}$ | $0.73^{+0.04}_{-0.02}$ | $-21.8^{+4.3}_{-2.9}$ |
| SSA22a − MD41 | $5.69^{+0.20}_{-0.13}$ | $0.54^{+0.07}_{-0.06}$ | $0.31 \pm 0.01$ | $36.5 \pm 0.2$ |
| Q2343 − BX389 | $5.93^{+0.17}_{-0.12}$ | $0.36^{+0.07}_{-0.05}$ | $0.30 \pm 0.01$ | $-48.6^{+0.3}_{-0.5}$ |
| Q2343 − BX610 | $4.44 \pm 0.08$ | $0.57 \pm 0.04$ | $0.56 \pm 0.01$ | $16.9^{+0.5}_{-0.9}$ |
| Q2346 − BX482 | $6.22^{+0.13}_{-0.12}$ | $0.14 \pm 0.01$ | $0.48 \pm 0.01$ | $-60.8^{+1.9}_{-1.5}$ |
| | Two-component models | | | |
| Q1623 − BX528 SE | $3.18^{+0.18}_{-0.25}$ | $1.20^{+0.15}_{-0.19}$ | $0.35^{-0.08}_{-0.03}$ | $-40.5^{+3.4}_{-1.7}$ |
| Q1623 − BX528 NW | $3.57^{+1.98}_{-0.57}$ | $2.91^{+1.70}_{-1.34}$ | $0.51^{+0.06}_{-0.05}$ | $-10.9^{+9.5}_{-5.2}$ |
| Q2343 − BX389 Main | $5.89^{+0.08}_{-0.09}$ | $0.32^{+0.04}_{-0.04}$ | $0.27 \pm 0.01$ | $-49.0^{+0.5}_{-0.4}$ |
| Q2343 − BX389 S | $2.71^{+2.18}_{-0.69}$ | $3.03^{+2.64}_{-1.75}$ | $0.20^{+0.35}_{-0.16}$ | $-41.5^{+2.2}_{-5.4}$ |

**Notes.** Structural parameters derived from Sérsic profile fits to the two-dimensional rest-frame ≈5000 Å surface brightness distribution from the NIC2 $H_{160}$-band images. Single-component models were fitted to all targets. For BX 528, two-component fits were also performed to account for the southeast ("SE") and northwest ("NW") components. Similarly for BX 389, where the two components represent the main part of the galaxy and the small companion to the south, "Main" and "S," respectively. The results are obtained from a series of 500 GALFIT runs as described in Section 4.1. The best-fit effective radius $R_e$, the Sérsic index $n$, the ratio of minor to major axis $b/a$, and the position angle P.A. (in degrees east of north) correspond to the median of the distribution of results, and the uncertainties represent the 68% confidence intervals around the best fit.

We find no significant correlation between structural parameters ($R_e$, $n$, and $b/a$) and SED derived properties ($M_\star$, age, $A_V$, absolute and specific SFR) among our targets. Studies of larger samples based on ground-based seeing-limited or higher resolution NICMOS/NIC3 near-IR imaging (e.g., Trujillo et al. 2006; Toft et al. 2007; Franx et al. 2008) show the existence of relationships between size, stellar mass, and star formation activity at $z \sim$ 2–3 (though with significant scatter). Among our five disks, MD 41 and BX 389 with highest $A_V$ values have the lowest axis ratios, which seems consistent with the trend of higher extinction in more edge-on star-forming disks observed locally (e.g., Maller et al. 2009; Yip et al. 2010). However,

clearly, only the strongest correlations would be discerned with our very small sample.

### 4.2. Non-parametric Analysis of the Morphologies

#### 4.2.1. Methodology

The models considered in the previous section are admittedly very simplistic. Simple one- or two-component axisymmetric models can reproduce reasonably well the overall surface brightness distribution of some of our sources but do poorly for others. Such a parametric approach appears to be satisfactory to estimate global parameters such as the effective radius
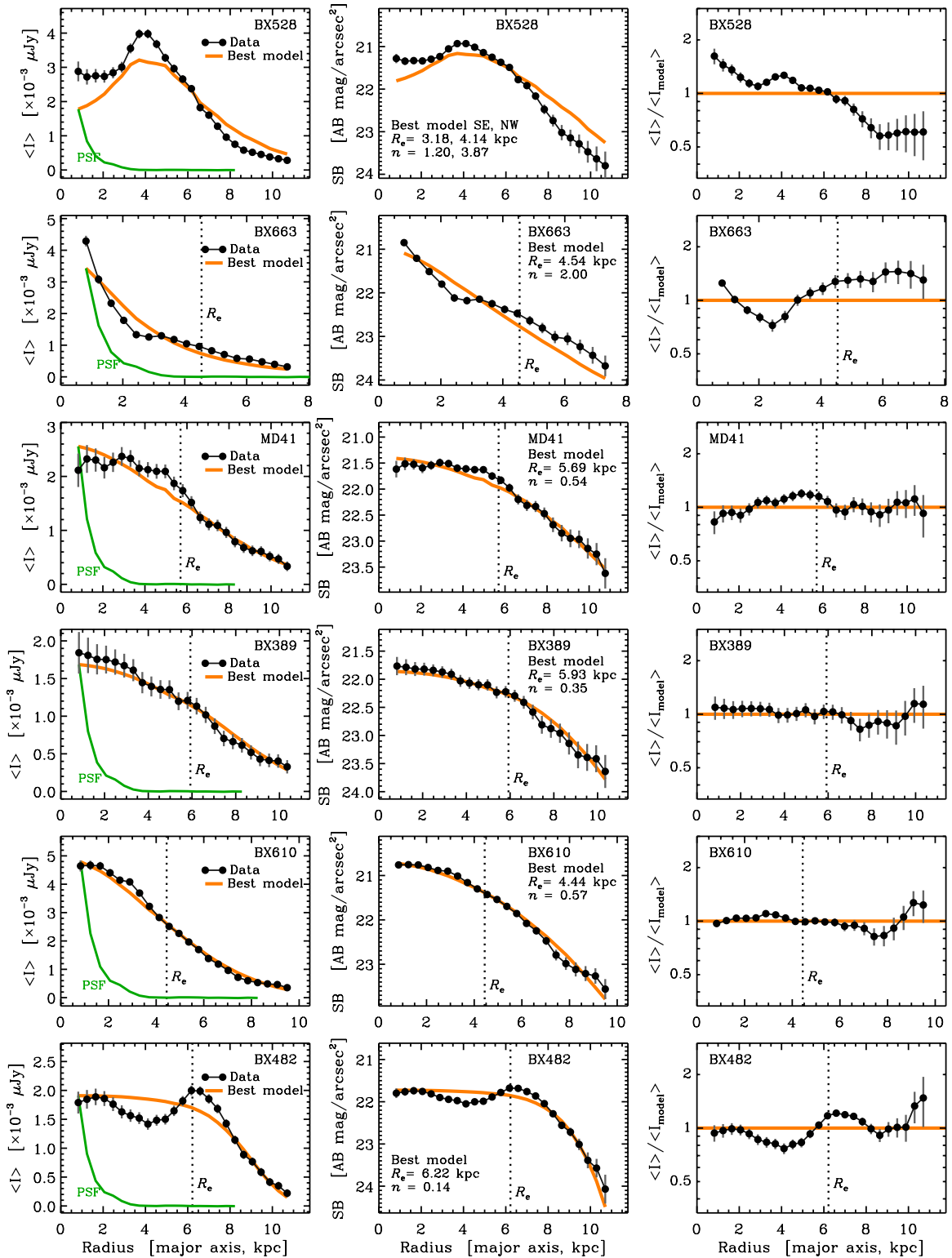
**Figure 6.** Radial profiles in $H_{160}$-band light of our NIC2 sample. The profiles are azimuthally averaged along concentric ellipses with center, semimajor axis, axis ratio, and orientation equal to the best-fit position, $R_e$, $b/a$, and P.A. values from the Sérsic model fits to the galaxies (see Section 4.1). Each row shows the results of a given galaxy, with the panels as follows. Left: mean intensity in units of $\mu$Jy as a function of semimajor axis radius of the elliptical annuli; the black curve and dots show the profile extracted from galaxy's image while the orange curve shows the corresponding profile for the best-fit Sérsic model. The radial intensity profile of the PSF (along concentric circular annuli) is plotted in green for reference. Middle: same as for the left panel for the mean surface brightness in units of mag arcsec$^{-2}$, with the best-fit structural parameters labeled explicitly. Right: ratio of the mean intensity profiles of the data and of the best-fit model as a function of semimajor axis radius of the elliptical annuli. For all galaxies except BX 528, single-component Sérsic models are considered, and the derived effective radius is indicated by a vertical dashed line. For BX 528, the model curves plotted here are extracted from the image for the best-fit two-component model but along elliptical annuli defined by the best-fit single-component model. The different intensity units between the left and middle panels are chosen to highlight in turn the central brighter and outer fainter regions of the sources.

(A color version of this figure is available in the online journal.)

and shape of the radial light profile. On the other hand, it obviously does not capture the prominent small-scale and irregular structure of clumpy disks and merging systems. The difficulty of describing star-forming galaxies at $z \sim 2$–$3$ within the framework of a Hubble sequence of more regular spiral and elliptical morphological types has been highlighted previously by several authors (e.g., Lotz et al. 2006; Law et al. 2007b; Peter et al. 2007). Accordingly, we also followed a non-parametric approach to characterize in detail morphologies of our galaxies, measuring the Gini, $M_{20}$, and multiplicity coefficients, which have been introduced and applied by Abraham et al. (2003), Lotz et al. (2004, 2006), and Law et al. (2007b).

The Gini parameter, $G$, is a measure of the uniformity with which the flux of a galaxy is distributed among its constituent pixels. $G = 0$ corresponds to the case where the flux is distributed evenly among all pixels, while $G = 1$ indicates that a single pixel contains all of the flux. The Gini parameter is formally defined such that

$$ G = \frac{1}{\bar{f} N_{\rm pix}(N_{\rm pix} - 1)} \sum_{i=1}^{N_{\rm pix}} (2i - N_{\rm pix} - 1) f_i, \qquad (3) $$

where $\bar{f}$ is the mean sky-subtracted flux per pixel, $f_i$ is the sky-subtracted flux in pixel $i$, and the pixels have been sorted in order of increasing flux.

The $M_{20}$ parameter represents the second-order moment of the brightest 20% of a galaxy's flux. The total second-order moment is defined such that

$$ M_{\rm tot} = \sum_{i}^{N_{\rm pix}} f_i [(x_i - x_c)^2 + (y_i - y_c)^2], \qquad (4) $$

where $f_i$ is the flux in each pixel, $x_i$ and $y_i$ indicate the pixel location, and $x_c$ and $y_c$ indicate the centroid of the galaxy light distribution, as determined from its first-order moments. $M_{20}$ is then computed by sorting galaxy pixels by flux, and summing $M_i$ until the pixel is reached at which 20% of the total galaxy flux is contained in pixels that have brighter or equal fluxes. That is

$$ M_{20} \equiv \log_{10} \left( \frac{\sum_i M_i}{M_{\rm tot}} \right), \text{ while } \sum_i f_i < 0.2 f_{\rm tot}. \qquad (5) $$

Lotz et al. (2004) introduced $M_{20}$ as an indicator sensitive to merger signatures such as multiple nuclei.

Finally, a third classification parameter, the multiplicity ($\Psi$), introduced by Law et al. (2007b), is somewhat analogous to the $M_{20}$ parameter, in that it is sensitive to the presence and distribution of multiple clumps of flux. $\Psi$ is conceptually akin to the total gravitational potential energy of a massive body. The "potential energy" of the pixel flux distribution can be described as

$$ \psi_{\rm tot} = \sum_{i=1}^{N_{\rm pix}} \sum_{j=1, j \neq i}^{N_{\rm pix}} \frac{f_i f_j}{r_{ij}}, \qquad (6) $$

where $r_{ij}$ is the distance between the $i$th and $j$th pixels. The greatest "potential energy" for a given set of pixel fluxes is the most compact distribution, with the brightest pixels at the center, and flux decreasing outward. Such a configuration would be described by

$$ \psi_{\rm compact} = \sum_{i=1}^{N_{\rm pix}} \sum_{j=1, j \neq i}^{N_{\rm pix}} \frac{f_i f_j}{r'_{ij}}, \qquad (7) $$
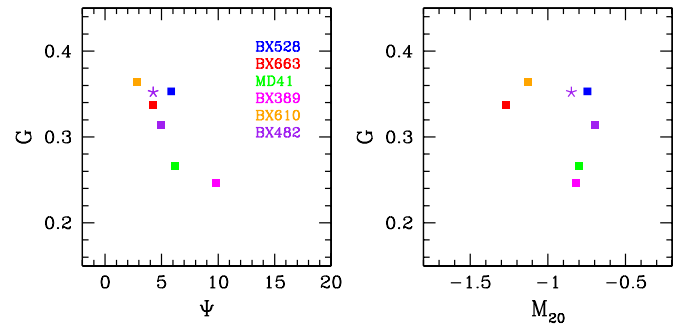


**Figure 7.** Morphological parameters for SINS galaxies derived from the NIC2 $H_{160}$-band images. Each galaxy was analyzed as if it was placed at the maximum redshift of the sample, i.e., $z = 2.43$. Left: Gini vs. $\Psi$ (multiplicity). Right: Gini vs. $M_{20}$. The AO-assisted SINFONI H$\alpha$ map of BX 482 was also analyzed in the same manner, and the results are plotted (star symbol) along with the NIC2 results (squares) in both panels.

(A color version of this figure is available in the online journal.)

where $r'_{ij}$ is the distance between the $i$th and $j$th pixels in the maximally compact configuration. The multiplicity, $\Psi$, is then defined to be

$$ \Psi = 100 \log_{10} \left[ \frac{\psi_{\rm compact}}{\psi_{\rm tot}} \right]. \qquad (8) $$

Law et al. (2007b) argued that $\Psi$ provides larger dynamic range than $M_{20}$. Illustrative examples of the relationship between multiplicity and overall appearance are provided by both Peter et al. (2007) and Law et al. (2007b).

Some care must be taken in assigning pixels to a galaxy light distribution, especially when considering galaxies over a range of redshifts, where the differential effects of cosmological surface brightness dimming must be taken into account. We search for pixels associated with a galaxy within a $1''.5$ radius of the galaxy centroid. Pixel selection is performed on a lightly smoothed version of the data, which has been convolved with a circularly symmetric Gaussian kernel with a 1 pixel standard deviation. We select pixels to be associated with the galaxy if the smoothed flux is more than $1.5(\frac{1+z_{\rm high}}{1+z})^3 \times \sigma$ above the sky, with $\sigma$ calculated from the raw data, and where $z_{\rm high}$ is the highest redshift for the subset of galaxies under consideration. The redshift-dependent factor counteracts the effects of surface brightness dimming in a given passband. Once pixels are assigned to a galaxy light distribution, the raw, unsmoothed data are used for morphological analysis.

### 4.2.2. Results for the NIC2 Targets

Figure 7 shows the resulting Gini, $M_{20}$, and $\Psi$ coefficients for the SINFONI sample. To control for surface brightness dimming effects, each galaxy was analyzed as if it would be observed at the maximum redshift in the sample, i.e., $z = 2.43$. The Gini values range from $G = 0.25$–$0.36$, with a median of $G_{\rm med} = 0.33$. The $\Psi$ values are in the range 2.8–9.8, with a median of $\Psi_{\rm med} = 5.4$. Finally, the $M_{20}$ values range from $-1.1$ to $-0.6$ with a median of $M_{20, \rm med} = -0.7$.

In order to interpret these numbers, we compare the NIC2 morphologies for objects in our sample with those derived from much larger samples of rest-UV-selected galaxies at similar redshifts with morphologies from optical imaging with the *HST* ACS. The ACS F814W ($i_{814}$-band) rest-UV morphologies from Peter et al. (2007) provide one such comparison sample, spanning a comparable redshift range to that of the objects in our
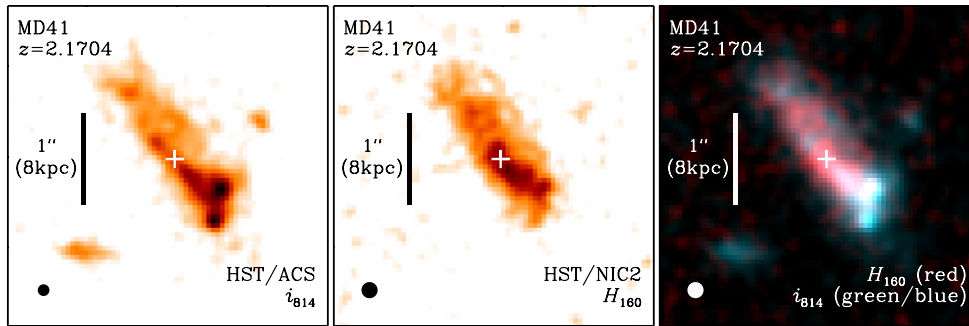
**Figure 8.** Comparison of rest-frame UV and optical morphologies for MD 41. North is up and east is to the left in both images, and a bar of $1''$ in length indicates the scale in the images. Left: ACS $i_{814}$-band map at the original angular resolution of the data, with the FWHM of the PSF indicated by the filled circle at the bottom left corner. Middle: same as the left panel for the NIC2 $H_{160}$-band map. Right: color composite after accurate PSF matching and registration of the ACS and NIC2 maps; in this RGB image, the red channel is assigned to the $H_{160}$ band and the green and blue channels to the $i_{814}$ band. The colors for all images plotted correspond to a linear flux density scale. The white cross shows the location of the geometrical center of MD 41 as determined from the NIC2 map. Overall, the images are strikingly similar, although on small scales there are noticeable differences. In particular, the two brightest clumps in the $i_{814}$ band on the southwest edge of the galaxy are much fainter in the $H_{160}$ band and, consequently, have bluer colors than the bulk of the source. In addition, two compact regions appear in the $i_{814}$-band image alone, which are offset from the main body of the galaxy. The colors of these compact offset sources are thus significantly bluer than that of the main part of the galaxy. These sources also have no counterpart in line emission within $\pm1000$ km s$^{-1}$ of the H$\alpha$ line of MD 41 in our SINFONI data. Therefore, we cannot determine whether they are physically associated with MD41.

(A color version of this figure is available in the online journal.)

NIC2 sample. To make a controlled comparison, we restrict the analysis to the subset of objects in the Peter et al. sample with the same average pixel-based S/N.[13] This subset of objects in the Peter et al. (2007) sample has an identical median $G$ value to the objects in our sample, and median $\Psi$ and $M_{20}$ values that are very similar ($\Psi_{med} = 7.0$ and $M_{20,med} = -0.8$). The data set used to analyze the ACS $i_{814}$-band morphologies of rest-UV-selected galaxies by Peter et al. (2007) has similar depth to the summed $BViz$ images featured in Law et al. (2007b), where rest-UV-selected objects were also analyzed. Accordingly, these authors found roughly identical rest-UV morphological results. Overall, the rest-frame optical morphologies for the objects in our sample are similar to the typical rest-frame UV morphologies for $z \sim 2$ star-forming galaxies.

One of the objects in our sample, MD 41, has existing deep ACS F814W imaging. In Figure 8, both ACS and NIC2 images are shown side by side at their respective original spatial resolution, along with an RGB color composite after PSF matching of the ACS map to the resolution of the NIC2 map (as described in Section 7.1). The average pixel S/N of MD 41 is very similar in the two images, making for a fair comparison of the wavelength-dependent morphology. Overall, the morphologies in the two bands are strikingly similar. The most notable difference consists of the two brightest clumps in the ACS map at the southwestern edge of MD 41, which have only faint counterparts in the NIC2 image and, accordingly, exhibit bluer colors than the rest of the galaxy. In addition, two compact (radius $\sim 0''.2$) sources offset by $\sim1''$ from the main body of the galaxy appear in the ACS image, alone, indicating significantly bluer colors than the main region of galaxy emission. We have not yet determined if these sources are associated with MD 41. In particular, a search of the SINFONI data cube does not reveal any emission line at these locations and within $\pm1000$ km s$^{-1}$ of the H$\alpha$ line of MD 41, which could support a physical association.

The Gini values measured in the ACS and NIC2 images of MD 41 are both $G \sim 0.3$, while the multiplicity is slightly lower for the rest-frame optical image (6.3) than the rest-frame UV image (9.7 with the two offset objects included and 8.1 without). The $M_{20}$ values are comparable as well, with $-0.7$ in the rest-frame optical and $-0.9$ in the rest-frame UV. While the parameters and appearance in each band are not identical, we stress that the differences are not significant. MD 41 does not display a strong morphological "k-correction," according to which the rest-frame UV and optical morphologies would trace light from very different stellar populations. Similar comparative studies of the rest-UV and optical morphologies of samples of $z \sim 1.5$–4 galaxies based on ACS optical and recent WFC3 $H_{160}$-band imaging are presented by Overzier et al. (2010) and Cameron et al. (2010).

For another object in the sample, BX 482, the SINFONI H$\alpha$ map obtained with LGS-AO and $0''.17$ PSF FWHM (Genzel et al. 2008; Förster Schreiber et al. 2009) is of sufficient resolution and S/N to measure the detailed morphological parameters using the same methodology and compare with the NIC2 $H_{160}$-band properties. We plot the morphological parameters derived from the H$\alpha$ map of BX 482 in Figure 7, along with the NIC2-based parameters. The H$\alpha$ line and $H_{160}$-band morphologies are quite similar in terms of $G$, $\Psi$, and $M_{20}$, with the prominent high surface brightness clump appearing in both SINFONI and NIC2 images.

We searched for correlations between the morphological ($G$, $\Psi$, and $M_{20}$) and stellar population parameters ($M_\star$, age, $A_V$, absolute and specific SFR). The most significant ($3\sigma$) trend is found between stellar mass and $G$, such that more massive galaxies are characterized by higher $G$ values. Correlations between $G$ and other gauges of galaxy evolutionary state such as age and specific SFR are not readily apparent within our sample. However, our sample of six objects is obviously too small for discerning all but the strongest trends. Furthermore, with only actively star-forming galaxies in our sample, we do not probe the full dynamic range of $z \sim 2$ star-forming histories. In Section 6, we return to the connection between morphology and other galaxy properties, considering our SINS sample alongside $z \sim 2$ galaxies selected using very different criteria (van Dokkum et al. 2008; Dasyra et al. 2008; Kriek et al. 2009).

---

[13] To determine the average pixel-based S/N, we calculated the average ratio over all object pixels of the flux in each pixel and the pixel-to-pixel noise in the background.
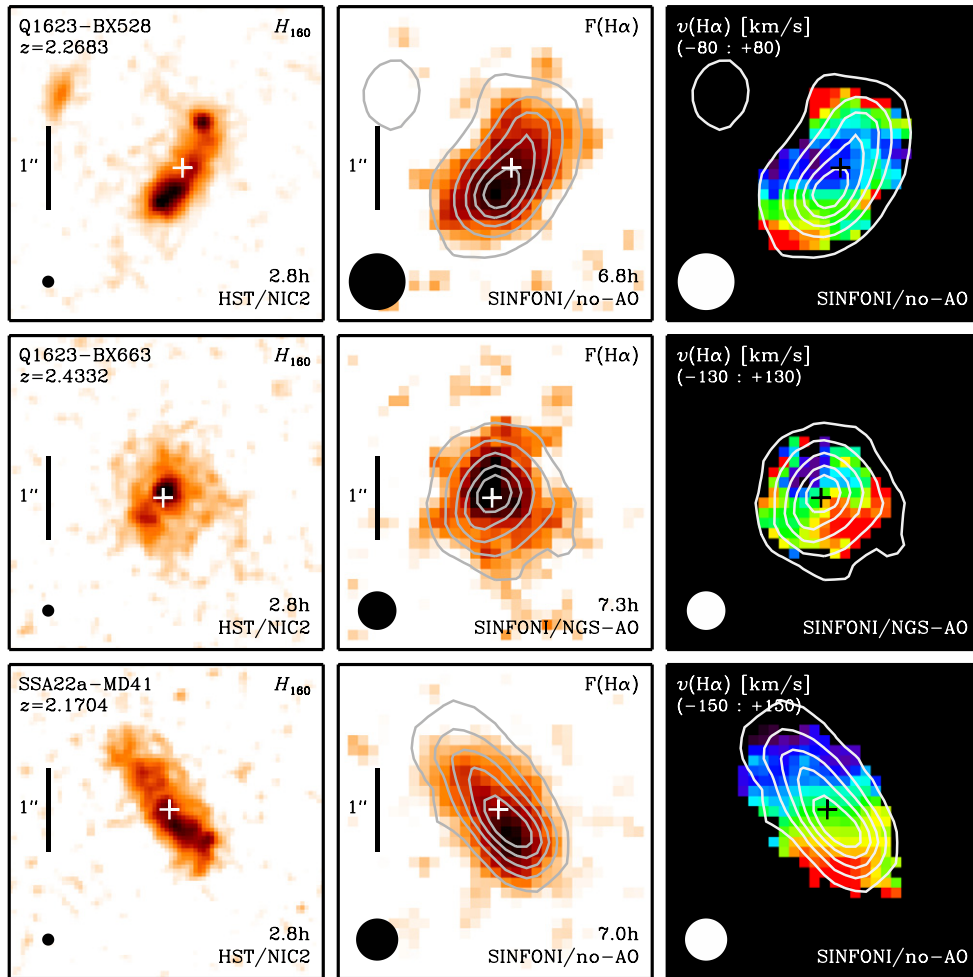
**Figure 9.** Comparison of $H_{160}$-band images and Hα line maps and velocity fields from SINFONI for three of our NIC2 targets: BX 528, BX 663, and MD 41. Each row corresponds to a given galaxy, with the panels as follows. Left: $H_{160}$-band map at the original NIC2 angular resolution. Middle: Hα line map with contours of the PSF-matched NIC2 $H_{160}$-band image overplotted in light gray. Right: Hα velocity field with contours of the PSF-matched NIC2 $H_{160}$-band image overplotted in white; the velocities are color coded from blue to red for blueshifted to redshifted line emission relative to the systemic velocity and over the range labeled at the top left. In each panel, the FWHM of the PSF of the corresponding image is shown by the filled circle in the bottom left corner. The vertical bar indicates an angular scale of $1''$ ($\approx 8$ kpc at the redshift of the sources). The white crosses mark the geometrical center of the sources. The total on-source integration times are also given for the NIC2 and SINFONI data, as well as whether the SINFONI data were obtained without AO or with AO using a natural or the laser guide star ("NGS-AO" and "LGS-AO," respectively).

(A color version of this figure is available in the online journal.)

## 5. COMPARISON WITH EMISSION LINE PROPERTIES FROM SINFONI

In this section, we combine the NIC2 images and SINFONI emission line data of our six targets to compare the Hα morphologies and structural parameters with those from the rest-frame optical emission, and determine the contribution from [O III] and Hβ line emission to broadband $H_{160}$ flux densities.

### 5.1. Comparison of Morphologies

For proper comparison of the $H_{160}$ band and Hα maps, we first convolved the NIC2 images to the spatial resolution of the SINFONI data. The SINFONI FOV is too small to include neighboring stars observed simultaneously with the galaxies, and the PSFs are based on the average of broadband images synthesized from the SINFONI data cubes of stars observed immediately before or after the target. These non-simultaneous PSF calibrations are however estimated to provide good representations of the PSF of the targets' data, to ≈20% in terms of the FWHM (Förster Schreiber et al. 2009). We computed the smoothing kernels with a Lucy–Richardson deconvolution al-

gorithm. Curve-of-growth analysis of the convolved NIC2 and original SINFONI PSFs indicates that the fraction of enclosed flux agrees to better than 5% in circular apertures with diameters in the range $0''.15$–$1''.5$ in all cases.

After convolution, we resampled the NIC2 images to the pixel scale of the SINFONI data where appropriate ($0''.125$ pixel$^{-1}$ for all sets but the AO $0''.05$ pixel$^{-1}$ data of BX 482) and aligned them with the emission line maps relying primarily on the outer isophotes. The detailed emission line and broadband morphologies can plausibly differ for any galaxy. However, for our sources, and especially at a seeing-limited resolution of $\approx 0''.5$, the overall light distribution turns out to be very similar. We verified the registration with line-free continuum maps extracted from the SINFONI data cubes for the brighter sources. In contrast to the line maps, the continuum maps have lower S/N so that mostly only the central brighter regions or the continuum peak are reliable. The alignment based on line and continuum in those cases agrees well within 1–2 SINFONI pixels.

Figures 9 and 10 show, for each target, the original $H_{160}$-band image along with the Hα line map and velocity field with contours of the convolved $H_{160}$-band image overplotted. The most
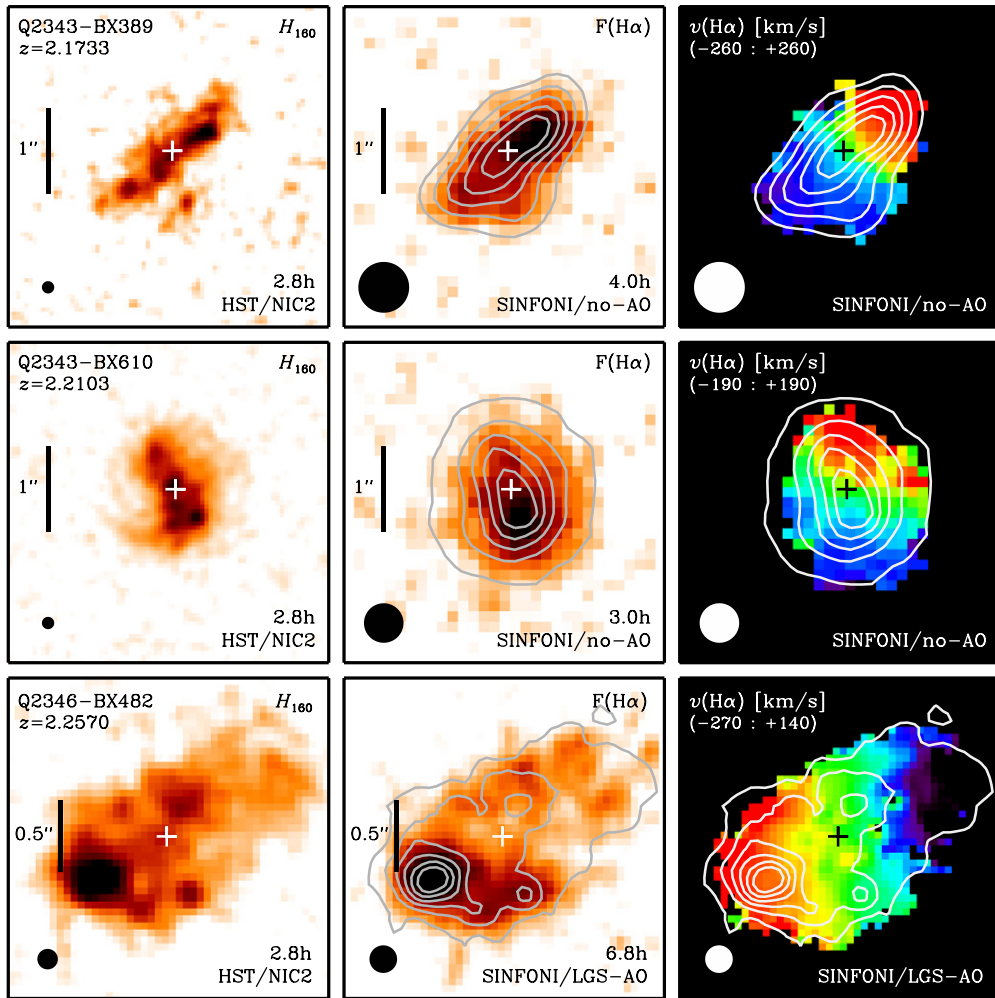
**Figure 10.** Same as Figure 9, but for the three other NIC2 targets: BX 389, BX 610, and BX 482.
(A color version of this figure is available in the online journal.)

detailed comparison is possible for BX 482 with AO-assisted SINFONI data. Both the lower surface brightness component and the brighter substructure are comparable between the $H_{160}$ band and H$\alpha$ emission. This similarity is reflected in the nearly equal values of Gini, multiplicity, and $M_{20}$ coefficients from the analysis in Section 4.2 (see Figure 7). In the details, there are however some noticeable differences. In particular, a few of the brighter peaks, or clumps, visible in the NIC2 or in the H$\alpha$ image have no obvious counterparts in the other map. The properties of the clumps identified in these two images are studied in Paper II. The central regions of BX 482 also appear to be slightly brighter in $H_{160}$-band emission than in H$\alpha$ emission.

For the other galaxies with lower resolution SINFONI data, the small-scale substructure is smeared out but the overall $H_{160}$ band and H$\alpha$ distributions at $0\farcs4$–$0\farcs6$ resolution are very similar. For BX 389, the southern companion that is clearly separated from the main galaxy in the original NIC2 image is still apparent at lower resolution as an extension in the outer isophotes. The well-resolved SE and NW merger components of BX 528, and the bridge of emission connecting them, blend together and the PSF-matched NIC2 image strikingly resembles the fairly regular and centrally concentrated H$\alpha$ line map. While in most cases, the general large-scale features of the morphologies are recognizable at $\approx 0\farcs5$ resolution, BX 528 offers an example where the nature of the system can only be reliably assessed

with the additional information from either the kinematics or higher spatial resolution data.

### 5.2. Comparison of Structural Parameters

We performed two-dimensional Sérsic model fits on both the H$\alpha$ maps and the PSF-matched NIC2 images using GALFIT, following the procedure described in Section 4.1.1. For BX 482, we ran fits on the AO-assisted as well as the seeing-limited H$\alpha$ data. For BX 528 and BX 389, we considered only single component fits since, at the $\approx 0\farcs5$ resolution of the SINFONI data, the merger components are unresolved in the former case, and the southern companion is blended with the primary galaxy in the latter. For consistency, fits on the convolved NIC2 images were restricted to a smaller region corresponding to the deepest area with effective $\approx 3\farcs8 \times 3\farcs8$ FOV of the SINFONI data at the $0\farcs125$ pixel$^{-1}$ scale, and $\approx 2\farcs3 \times 2\farcs3$ FOV of the AO data at $0\farcs05$ pixel$^{-1}$ for BX 482. This reduced area potentially affects the sky background estimates, degenerate with the profile shape and half-light radius. The smaller FOV as well as the broader PSF both contribute to the significantly larger uncertainties for the fits performed on the lower resolution maps compared to those using the maps at the original NIC2 resolution. Table 5 reports the best-fit structural parameters and Figure 11 compares the results from H$\alpha$ with those from the PSF-matched NIC2 data.
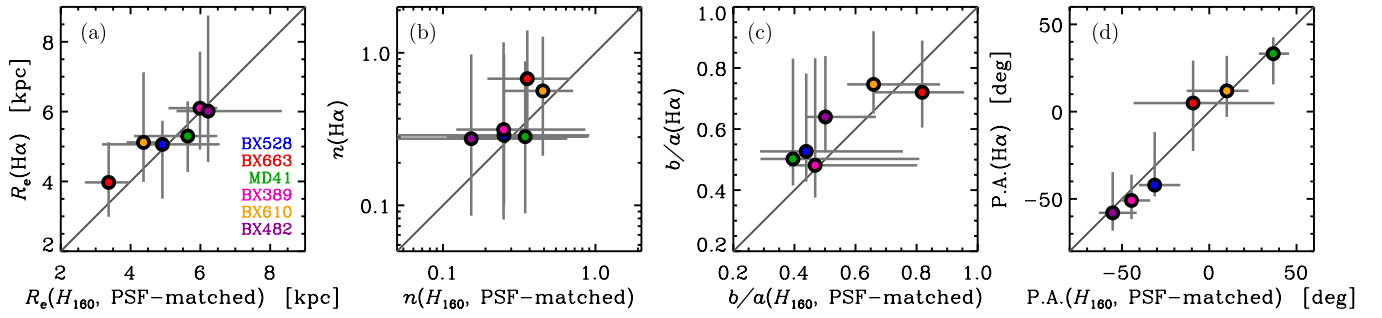
**Figure 11.** Comparison of the structural parameters from single-component Sérsic profile fits to the two-dimensional $H_{160}$ band and Hα surface brightness distributions. For consistency, the fits were performed on the $H_{160}$-band images matched to the PSF and resampled to the $0\farcs125$ pixel$^{-1}$ scale of the lower $\approx 0\farcs5$ resolution Hα maps. Data for the different targets are color coded as indicated in the leftmost panel. (a) Effective radius. (b) Sérsic index. (c) Axis ratio. (d) Position angle (in degrees east of north). The solid line indicates the one-to-one relation. The parameters derived from the Hα and smoothed $H_{160}$-band maps at $\approx 0\farcs5$ resolution are in good agreement and typically within their $1\sigma$ uncertainties. They also agree well with the values obtained from fits to the original higher resolution NIC2 images (see Table 5).

(A color version of this figure is available in the online journal.)

**Table 5**
Best-fit Structural Parameters from the SINFONI Hα Maps and PSF-matched NIC2 $H_{160}$-band Images

| Object | Map | FWHM Resolution[a] | $R_e$[b] (kpc) | $n$[b] | $b/a$[b] | P.A.[b] (deg) |
|---|---|---|---|---|---|---|
| Q1623 − BX528 | Hα | $0\farcs63$ | $5.06^{+0.68}_{-1.56}$ | $0.29^{+0.69}_{-0.19}$ | $0.53^{+0.26}_{-0.10}$ | $-42.1^{+30.4}_{-6.5}$ |
| | $H_{160}$ | $0\farcs63$ | $4.91^{+1.64}_{-1.73}$ | $0.25^{+0.66}_{-0.23}$ | $0.44^{+0.32}_{-0.15}$ | $-31.3^{+14.7}_{-9.0}$ |
| Q1623 − BX663 | Hα | $0\farcs39$ | $3.97^{+1.15}_{-0.99}$ | $0.68^{+0.73}_{-0.41}$ | $0.72^{+0.17}_{-0.12}$ | $4.9^{+24.3}_{-27.4}$ |
| | $H_{160}$ | $0\farcs39$ | $3.37^{+0.58}_{-0.68}$ | $0.36^{+0.32}_{-0.16}$ | $0.82^{+0.14}_{-0.16}$ | $-9.3^{+46.6}_{-34.0}$ |
| SSA22a − MD41 | Hα | $0\farcs44$ | $5.30^{+0.99}_{-1.02}$ | $0.28^{+0.60}_{-0.19}$ | $0.50^{+0.33}_{-0.09}$ | $33.2^{+9.3}_{-17.6}$ |
| | $H_{160}$ | $0\farcs44$ | $5.64^{+0.85}_{-1.54}$ | $0.35^{+0.55}_{-0.24}$ | $0.40^{+0.41}_{-0.11}$ | $36.7^{+9.0}_{-8.3}$ |
| Q2343 − BX389 | Hα | $0\farcs54$ | $6.10^{+1.62}_{-1.19}$ | $0.31^{+0.86}_{-0.23}$ | $0.48^{+0.35}_{-0.11}$ | $-50.9^{+14.8}_{-10.7}$ |
| | $H_{160}$ | $0\farcs54$ | $5.99^{+0.49}_{-0.90}$ | $0.25^{+0.61}_{-0.13}$ | $0.47^{+0.33}_{-0.09}$ | $-44.6^{+10.7}_{-5.8}$ |
| Q2343 − BX610 | Hα | $0\farcs39$ | $5.12^{+2.01}_{-1.13}$ | $0.56^{+0.71}_{-0.35}$ | $0.75^{+0.17}_{-0.10}$ | $11.9^{+20.1}_{-14.9}$ |
| | $H_{160}$ | $0\farcs39$ | $4.37^{+0.62}_{-0.49}$ | $0.45^{+0.26}_{-0.20}$ | $0.66^{+0.22}_{-0.09}$ | $10.1^{+12.5}_{-23.0}$ |
| Q2346 − BX482 | Hα | $0\farcs17$ | $6.07^{+7.09}_{-1.46}$ | $0.35^{+3.47}_{-0.28}$ | $0.59^{+0.21}_{-0.12}$ | $-50.2^{+32.4}_{-6.7}$ |
| | $H_{160}$ | $0\farcs15$ | $6.22^{+0.13}_{-0.12}$ | $0.14 \pm 0.01$ | $0.48 \pm 0.01$ | $-60.9^{+1.9}_{-1.5}$ |
| | Hα | $0\farcs50$ | $6.01^{+2.74}_{-1.46}$ | $0.27^{+0.70}_{-0.19}$ | $0.64^{+0.20}_{-0.11}$ | $-58.0^{+23.4}_{-10.2}$ |
| | $H_{160}$ | $0\farcs50$ | $6.22^{+2.11}_{-0.91}$ | $0.15^{+0.50}_{-0.11}$ | $0.50^{+0.17}_{-0.06}$ | $-55.4^{+13.7}_{-8.0}$ |

**Notes.** Structural parameters derived from single-component Sérsic profile fits to the two-dimensional Hα maps from SINFONI and to the $H_{160}$-band images from NIC2 convolved to the effective spatial resolution and resampled to the pixel scale of the SINFONI data. The results are obtained from a series of 500 GALFIT runs as described in Section 4.1, and the best-fit value and uncertainties correspond to the median and 68% confidence intervals of the distribution of results in each parameter.
[a] PSF FWHM of the SINFONI Hα maps, and of the convolved NIC2 $H_{160}$-band images.
[b] Main structural parameters derived from the GALFIT fits: the effective radius radius $R_e$, the Sérsic index $n$, the ratio of minor to major axis $b/a$, and the position angle P.A. (in degrees east of north).

Overall, there is good agreement between the measurements based on the different data sets, with differences almost always within the (larger) $1\sigma$ uncertainties of the results obtained from the lower resolution maps. BX 663 is the most deviant source, with largest offsets in Sérsic index (smaller by 1.3–1.6), half-light radius (smaller by factors of 1.14–1.35), and P.A. (differences by $\approx 15°$–$25°$) between the lower resolution Hα and PSF-matched $H_{160}$-band maps and the original resolution $H_{160}$-band image. On the other hand, the parameters derived from the Hα and PSF-matched $H_{160}$ maps are in closer agreement, with $R_e$ and $n$ for Hα higher by 18% and 0.3, respectively, and $b/a$ lower by 13%, all within the $1\sigma$ uncertainties. To investigate the cause of the differences in parameters obtained from the original $H_{160}$-band image of this galaxy and from the smoothed and resampled version, we created a pure $n = 2$ Sérsic model with total magnitude, $R_e$, $b/a$, and P.A.

equal to the values of the best fit to the original NIC2 map of BX 663. The mock galaxy was pasted into an empty area of the full NIC2 map, which was then convolved to the SIN-FONI PSF, and finally resampled to $0\farcs125$ pixel$^{-1}$. The input parameters are recovered within $<1\sigma$ by the fitting procedure in the $0\farcs05$ pixel$^{-1}$ data, both at the original NIC2 and the lower SINFONI resolution (with differences of $\leqslant 4\%$ in $R_e$ and $<0.2$ in $n$). Significantly lower $R_e$ and $n$ index are derived after resampling to the larger pixel scale with, however, the best-fit parameters for the mock galaxy in excellent agreement with those of the real PSF-matched and resampled $H_{160}$-band image of BX 663 (within $<1\sigma$, with 4% difference in $R_e$ and 0.12 in $n$). These tests indicate that the information on the steep inner profile of BX 663 leading to $n = 2$ is lost with the coarser $0\farcs125$ pixel$^{-1}$ sampling despite the good $\approx 0\farcs4$ resolution of its SINFONI data.

**Table 6**
Emission Line Contributions to the $H_{160}$-band Flux Densities

| Object | $f_{BB}$([O III] $\lambda$ 5007) | $f_{BB}$([O III] $\lambda$ 4959) | $f_{BB}$(H$\beta$) | $f_{BB}$(tot) |
|---|---|---|---|---|
| Q1623 − BX528 | ... | ... | ... | ... |
| Q1623 − BX663 | < 0.05 | < 0.02 | < 0.12 | < 0.20 |
| SSA22a − MD41 | 0.11 ± 0.01 | 0.043 ± 0.005 | 0.023 ± 0.004 | 0.17 ± 0.01 |
| Q2343 − BX389 | 0.19 ± 0.02 | 0.050 ± 0.008 | < 0.054 | < 0.29 |
| Q2343 − BX610 | 0.034 ± 0.004 | 0.013 ± 0.002 | 0.018 ± 0.002 | 0.064 ± 0.005 |
| Q2346 − BX482 | 0.062 ± 0.006 | 0.019 ± 0.003 | < 0.037 | < 0.12 |

**Notes.** Individual and total fractional contributions of the [O III] $\lambda\lambda$ 4959, 5007 and H$\beta$ emission lines to the integrated broadband flux density measured from the NIC2 $H_{160}$-band data. The uncertainties correspond to 1$\sigma$ uncertainties from the line fluxes and broadband magnitudes. For undetected lines, the 3$\sigma$ upper limit on the line flux has been used.

For the other five sources, a comparison of the fits to the smoothed and original $H_{160}$ maps indicates that the half-light radii, Sérsic indices, and P.A.s agree on average to <1%, 0.1, and 4°, respectively, with differences among individual galaxies of at most 2%, 0.2, and 7°. The axis ratios are higher by ≈30% on average (in the range 5%–55%) for the fits to the smoothed NIC2 data. Among these five sources, the differences between fits to the ≈0″.5 resolution H$\alpha$ and PSF-matched $H_{160}$ maps are on average 3% for $R_e$, 0.08 for $n$, and 5° for P.A. (at most 17%, 0.12, and 11°). The axis ratios from the H$\alpha$ maps are higher than those from the smoothed $H_{160}$ data by 20% on average (in the range 3%–30%). For BX 482, the differences between the parameters obtained based on the seeing-limited and AO H$\alpha$ maps are in the same ranges as for the smoothed versus unsmoothed $H_{160}$-band maps for the other sources (excluding BX 663). The close agreement between the parameters derived from the H$\alpha$ and $H_{160}$-band emission for BX 482, either at ≈0″.15 or ≈0″.5 resolution, is unsurprising in view of their similar morphologies in the high-resolution SINFONI and NIC2 data (Figures 7 and 10).

One important implication of the Sérsic model fits is that the global H$\alpha$ and rest-frame ≈5000 Å light distributions do not differ significantly from each other. This result is further supported by the comparison of the radial light profiles extracted along ellipses with center, axis ratio, and P.A. from the best-fit model to the $H_{160}$-band maps in Figure 12. In this Figure, the lower resolution H$\alpha$ and PSF-matched $H_{160}$ maps are used for all sources, except for BX 482 where the profiles are extracted from the AO-assisted H$\alpha$ data and original $H_{160}$-band image. At ≈0″.5 resolution, the H$\alpha$ and $H_{160}$-band profiles follow closely each other, with differences becoming important only beyond ≈1.5–2 $R_e$ or typically 8–10 kpc. For the low flux levels reached at these large radii, systematic residuals in background subtraction and flat fielding potentially affect the profiles in a substantial way. At radii $\lesssim$ 1.5–2 $R_e$, some of the (small) discrepancies may reflect differences in the detailed morphologies as well as uncertainties in the exact SINFONI PSF and thus the convolution kernel applied to smooth the NIC2 data. For the higher resolution profiles of BX 482, the ring-like feature that is dominated by the very bright clump on the southeast side of the galaxy is prominent in both H$\alpha$ and rest-frame ≈5000 Å; as seen also from Figure 10, the regions in the vicinity of the galaxy center are comparatively fainter in H$\alpha$ than in $H_{160}$-band light.

The comparisons above do not indicate significant beam-smearing effects between angular resolution of FWHM ≈ 0″.15 and ≈0″.5 for the objects in our NIC2 sample. The galaxies are sufficiently large that their overall radial light distributions remain well resolved at ≈0″.5 resolution. The most noticeable difference is the systematic shift to higher axis ratios for all sources. The coarser 0″.125 pixel$^{-1}$ sampling leads to a significant decrease in the Sérsic index for BX 663, the object with steepest inner light profile ($n$ = 2) at 0″.05 pixel$^{-1}$. The parametric fits do not reveal any major difference between H$\alpha$ and broadband rest-frame ≈5000 Å emission in terms of $R_e$, $n$, and P.A. for the five sources with $n$ < 1.

### 5.3. Emission Line Contributions

In view of the similarity between the $H_{160}$ band and H$\alpha$ maps for our targets, it is important to assess the contribution of emission lines to the broadband emission. At the redshift of our targets, the NIC2 F160W bandpass includes the [O III] $\lambda\lambda$ 4959, 5007 doublet and H$\beta$. For all sources except BX 528, SINFONI seeing-limited observations of these lines with the $H$-band grating were taken as part of the SINS survey (Förster Schreiber et al. 2009). These data are analyzed and discussed by P. Buschkamp et al. (2011, in preparation), to which we refer for details. The [O III] lines are detected in all galaxies but BX 663, while H$\beta$ is detected in MD 41 and BX 610. Some of the non-detections can be attributed to the galaxies' lines being redshifted to the wavelength of bright telluric lines (in particular H$\beta$ for BX 663 and BX 482). For all non-detections, we derived upper limits on the fluxes.

Table 6 reports the fractional emission line contribution based on the integrated $H_{160}$-band flux density and line fluxes (or 3$\sigma$ upper limits). In all five sources with SINFONI $H$-band data, H$\beta$ is the weakest line. The largest line contribution is inferred for BX 389, where the [O III] lines make up 24% of the total $H_{160}$-band flux density and, with the 3$\sigma$ upper limit on H$\beta$, the total line contribution is estimated at <29%. BX 610 has the smallest contributions, amounting to ≈6% for all three lines combined. The broadband $H_{160}$ emission of our NIC2 targets is thus clearly dominated by the continuum, with only a modest to very small fraction from the [O III] and H$\beta$ lines.

While the general appearance of the targets in [O III] emission, and in H$\beta$ where detected, resembles that in H$\alpha$, there are in some cases measurable differences. These gradients in line ratios reflect spatial variations in line excitation or gas-phase oxygen abundance, and in dust extinction across the targets (Genzel et al. 2008; P. Buschkamp et al. 2011, in preparation). To assess possible spatial variations in the emission line contributions, we also examined the galaxies on a pixel by pixel basis after convolving the NIC2 maps to the PSFs of the SINFONI $H$-band data, resampling them to 0″.125 pixel$^{-1}$, and aligning them following the same procedure as for H$\alpha$. We considered only pixels with S/N $\geqslant$ 3 in both $H_{160}$ flux density and line flux (the summed fluxes over these pixels represent typically
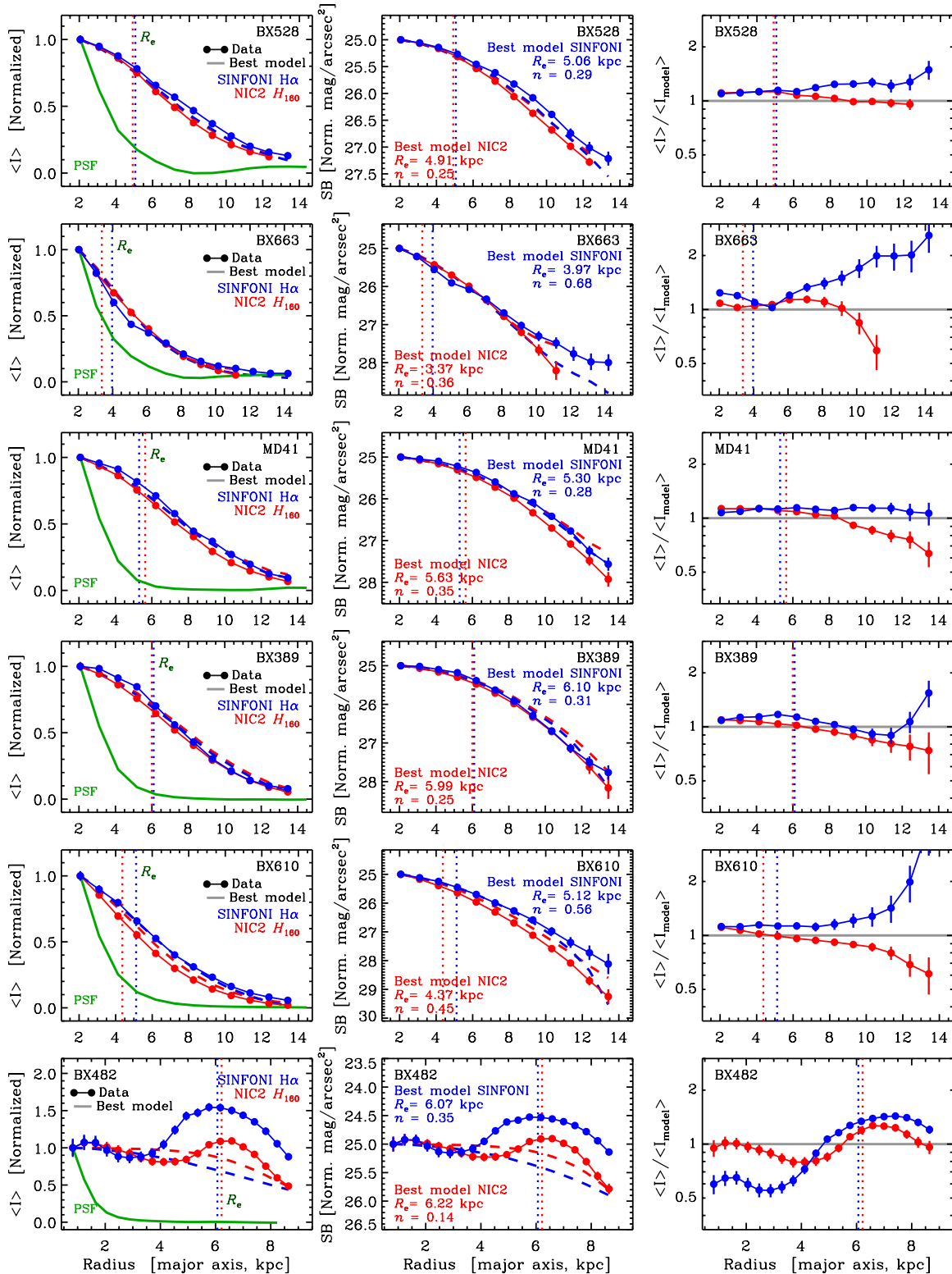
**Figure 12.** Radial light profiles of the Hα and $H_{160}$-band emission of the targets. The profiles and best-fit single-component Sérsic model overplotted are based on the ≈0″.5 resolution SINFONI Hα maps (using the 0″.125 pixel$^{-1}$ scale, taken under seeing-limited conditions or with NGS-AO for BX 663) and PSF-matched NIC2 $H_{160}$ images except for BX 482, where the AO-assisted SINFONI and original resolution NIC2 data both at 0″.05 pixel$^{-1}$ are used (see Section 5). From left to right, each row shows for a given source the mean intensity in linear flux units, the surface brightness in magnitude units, and the ratio of the observed intensity profile to that of the best-fit Sérsic model (Section 5.2). The data are plotted with solid lines and dots, and the models are shown with dashed lines; blue and red colors are used for Hα and $H_{160}$ band, respectively. The profiles are computed along ellipses with center, axis ratio, and P.A. corresponding to the Sérsic model that best fits the NIC2 images; the maximum radius is determined by the effective field of view of the SINFONI data and so as to avoid the noisiest parts at the edges. The intensity and surface brightness profiles are all normalized to unity and 25 mag, respectively, at the central position. The ratio of observed and model intensity profiles is as computed before normalization, and the horizontal gray line in the right-hand panels indicates a ratio of unity. The vertical dotted lines in all panels show the best-fit effective radii from the Sérsic fits, and the SINFONI PSF radial intensity profiles are plotted in the left-hand panels in green for reference. The close correspondence between Hα and rest-frame ≈5000 Å radial light distributions is striking, reflecting the similarity in the maps shown in Figures 9 and 10.

(A color version of this figure is available in the online journal.)

>75% of the integrated measurements of the galaxies in 3″ diameter apertures). The mean and median of the [O III] $\lambda\,5007$ contributions for the four sources where the line is detected are within $\approx7\%$ of the estimates from the integrated fluxes. The top (75%) quartile of the pixel line contributions range from 7% (BX 610) to 16% (BX 389). For H$\beta$, detected in MD 41 and BX 610, the mean and median contributions in individual pixels are within $\leqslant5\%$ of those determined from the total fluxes, with top quartiles of 7% for MD 41 and 2% for BX 610. We conclude that spatial variations in line emission are not likely to affect significantly the observed $H_{160}$-band morphologies.

## 6. COMPARISON WITH OTHER $z \sim 2$ SAMPLES

As we found in Section 4, there are hardly any significant trends of structural parameters or morphological properties with global stellar and dust extinction properties among our six SINS galaxies. However, the small sample size leads to limited statistics and range in parameter space covered. In order to expand our analysis and ultimately place the morphological results for our NIC2 sample of rest-UV-selected galaxies in the larger context of the $z \sim 2$ galaxy population, we compare their properties to those of galaxy samples selected using very different photometric criteria. We restrict this comparison to samples in the same redshift range that have been characterized using the same type of observations, i.e., $HST$/NIC2 F160W imaging. The two comparison samples are 19 $K$-selected galaxies presented by van Dokkum et al. (2008) and Kriek et al. (2009), and 11 24 $\mu$m selected dusty, IR-luminous galaxies from Dasyra et al. (2008).

The parent sample for the van Dokkum et al. (2008) and Kriek et al. (2009) analyses is described by Kriek et al. (2006, 2008b) and consists of 36 massive galaxies with $K_{\rm Vega} < 19.7$ mag, $1.6 \leqslant z \leqslant 3.0$, and $\log(M_\star/M_\odot) > 10.5$. The stellar masses are given by Kriek et al. (2008b) for a Salpeter (1955) IMF; we divided them by 1.7 for consistency with our adopted Chabrier (2003) IMF throughout the analysis below. All galaxies in this $K$-selected sample have spectroscopy with the *Gemini* near-IR spectrograph (GNIRS), and 19 objects obtained early in the survey, at $2 < z < 2.6$, have NIC2 imaging with the F160W filter. Based on their GNIRS spectra, nine of these objects present no detectable H$\alpha$ emission, with an upper limit of $W$(H$\alpha$) = 10 Å. The remaining 10 objects have detectable rest-frame optical emission lines, indicating either star formation or AGN activity (for six and four objects, respectively; Kriek et al. 2009). The range of activity in this roughly stellar mass-selected sample of 19 objects is reflected in their structural parameters. The nine quiescent galaxies are very compact, nearly circularly symmetric, and show little if any substructure except for one source. They are characterized by a median circularized effective radius[14] of 0.9 kpc (ranging from 0.5 to 2.4 kpc), and a median Sérsic index, $n$, of 2.3 (ranging from 0.5 to 4.5). The six star-forming galaxies are significantly more extended and less centrally concentrated, and appear more similar to our SINS targets. Their median $R_{\rm e,circ}$ is 2.8 kpc (ranging from 1.5 to 5.0 kpc) and median $n$ index is 0.9 (ranging from 0.0 to 3.3). The four AGN sources resemble the quiescent galaxies on average in terms of structure, with a median size of $R_{\rm e,circ} \approx 1.1$ kpc and Sérsic index of $n \approx 2.5$.

As discussed by Kriek et al. (2009), in terms of establishing evolutionary connections within this $K$-selected NIC2 sample, half of the star-forming galaxies appear to constitute direct structural precursors to the AGN and quiescent galaxies, based on the fact that the majority of their stellar mass may be contained within a compact core. However, the remaining star-forming galaxies lack evidence for a strong, central mass concentration and therefore any direct structural link with the quiescent objects (Kriek et al. 2009). The median stellar mass for the quiescent galaxies is $1.6 \times 10^{11}\,M_\odot$, implying central stellar mass densities $\sim$100 times higher than for $z \sim 0$ galaxies with similar stellar mass, characterized by significantly larger effective radii ($\sim$5 kpc). Understanding the formation and evolution of such compact, quiescent galaxies at high $z$ is the basis of much ongoing observational and theoretical work (e.g., Trujillo et al. 2007; Cimatti et al. 2008; van der Wel et al. 2008; Damjanov et al. 2009; Hopkins et al. 2009; Mancini et al. 2010; Wuyts et al. 2010).

The parent sample for the objects we analyzed from Dasyra et al. (2008) consists of 52 IR-bright sources in the *Spitzer* Extragalactic First Look Survey, with 24 $\mu$m fluxes greater than 0.9 mJy, $\nu F_\nu(24\,\mu{\rm m})/\nu F_\nu(8\,\mu{\rm m}) > 0.5$, and $\nu F_\nu(24\,\mu{\rm m})/\nu F_\nu(6440\,{\rm Å}) > 1$. The latter two criteria were designed to select dusty starbursts at $z \gtrsim 1$, or obscured AGNs. Thirty-three such sources at $z > 1.5$ were imaged with NIC2 and the F160W filter, 11 of which are in the $2.0 \leqslant z \leqslant 2.5$ range of interest here. All of these sources have rest-frame 14 $\mu$m luminosities greater than $10^{12}\,L_\odot$ (derived from *Spitzer*/Infrared Spectrograph (IRS) data), implying total IR luminosities greater than $\sim10^{13}\,L_\odot$. Each is classified as one of the multiple types based on its mid-IR IRS spectrum. The sample considered here contains the following types: "polycyclic aromatic hydrocarbon (PAH)," indicating a spectrum dominated by PAH emission (one object); "AGN," indicating a spectrum characterized primarily by the AGN continuum (two objects); "obscured," indicating a spectrum dominated by the SiO absorption feature at 9.7 $\mu$m (four objects); or, finally, "mixed," in which no single starburst or AGN component dominates the spectrum (four objects). The median NIC2 $H_{160}$-band magnitude for these 11 objects is $H_{160,{\rm AB}} = 22.19$ mag, ranging from 21.51 to 24.10 mag, and their median half-light radius (estimated using the SExtractor software package; Bertin & Arnouts 1996) is 2.4 kpc, ranging from 1.5 to 4.3 kpc. These sources show varied morphologies, from compact and regular to multiple systems, to disturbed and/or irregular; the majority, however, tends to be more compact and concentrated than our SINS targets. Dasyra et al. (2008) assign a qualitative description of the morphology of each object in their NIC2 sample, to assess the importance of merger events. Of the 11 objects described here, five are classified as exhibiting no signs of interaction, five are "Distorted," and one is "Binary."

These comparison samples observed with the same NICMOS camera and filter, and spanning the same redshift range as our SINS NIC2 targets, enable in principle a controlled comparison of morphological properties. However, slightly different analysis techniques, integration times, and pixel sampling are featured in the published work. These differences have consequences for the derivation of the morphological properties, which depend on the depth of the data as well as on the pixel sampling and S/N threshold applied for the analysis. We therefore obtained the actual images for these samples (P. G. van Dokkum 2008, private communication; L. Yan 2008, private communication; M. Kriek 2010, private communication) and performed a uniform analysis of our NIC2 sample alongside each of the comparison samples.

---

[14] The circularized effective radius is defined as $R_{\rm e,circ} \equiv R_{\rm e}\sqrt{b/a}$.
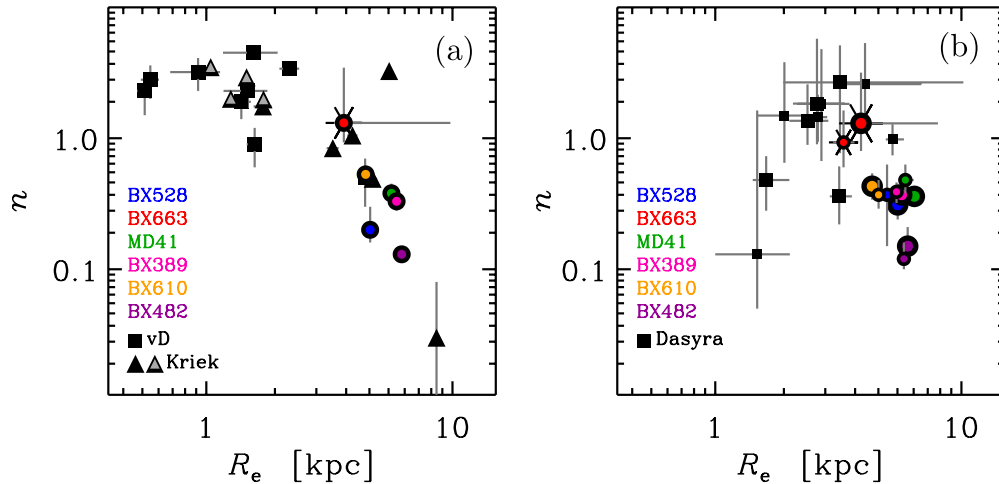
**Figure 13.** Sérsic index $n$ vs. effective radius $R_e$ for our six SINS galaxies and comparison samples at similar redshifts but with different selection criteria. All galaxies were observed with the same NICMOS NIC2 camera through the same F160W filter and the Sérsic model fits were performed in the same way for all samples, allowing consistent comparisons. (a) $n$ vs. $R_e$ for the SINS and the $K$-selected samples (labeled "vD" for objects from van Dokkum et al. 2008 and "Kriek" for those from Kriek et al. 2009). The images used for all sources were drizzled to a $0''.038$ pixel scale. Results for the SINS galaxies based on the full 4-orbit data and 3-orbit subsets (as 17 of 19 of the $K$-selected objects) are indistinguishable, so the parameters derived from the 4-orbit data are plotted. The SINS targets are plotted with filled circles following the color scheme as given by the labels. Squares and triangles correspond to the quiescent and star-forming $K$-selected samples of van Dokkum et al. (2008) and Kriek et al. (2009), respectively. The AGN sources are distinguished with a starred circle for BX 663 in our SINS sample, and with gray-filled triangles for those of the Kriek et al. sample. (b) Same as the previous panel, but for the SINS and 24 $\mu$m selected dusty IR-luminous sample of Dasyra et al. (2008, labeled "Dasyra"). All images used here were drizzled to $0''.076$ pixels. Large and small symbols are used for results based on 2- and 1-orbit integrations, respectively. Ten of 11 sources from Dasyra et al. (2008) show signatures of AGN activity in their mid-IR spectrum, either dominant or along with PAH features indicative of star formation; the only star formation dominated object is the second largest with second highest $n$ (4.06 kpc and 2.59).

(A color version of this figure is available in the online journal.)

### 6.1. Comparison of Structural Parameters

As a first step in our comparison, we considered the global structural parameters and, more specifically, the effective radius $R_e$ and Sérsic index $n$. While each of the SINS targets was observed for four orbits, 17 of the 19 $K$-selected targets were observed for three orbits and the two brightest objects for two orbits. In the 24 $\mu$m selected sample, five objects were observed for two orbits, and six for only one orbit. Moreover, the published images from van Dokkum et al. (2008) and Kriek et al. (2009) were drizzled to $0''.038$ pixels, while those of Dasyra et al. (2008) to $0''.076$ pixels. To match both the imaging depth and sampling of the two comparison samples, we created 1-, 2-, and 3-orbit subsets of the NIC2 data of our SINS targets, and also drizzled them to $0''.038$ and $0''.076$ pixel$^{-1}$. We repeated our single-component Sérsic model fitting as described in Section 4.1.1 for each combination of exposure time and pixel sampling. Because of the differences in depth and pixel sampling of the van Dokkum et al. (2008) and Kriek et al. (2009) NIC2 data with respect to those of Dasyra et al. (2008), we compare our SINS targets separately with the $K$-selected and 24 $\mu$m selected samples.

For the $K$-selected galaxies, van Dokkum et al. (2008) and Kriek et al. (2009) derived the structural parameters using the same code as we employed (GALFIT) and a conceptually analogous approach was followed in treating the sky background. We thus adopted the best-fit $R_e$ and $n$ parameters as published by these authors, converting the circularized effective radii to standard effective radii. None of our conclusions is affected if we convert our radii to circularized radii instead. For the SINS galaxies, the difference in structural parameters between the 3- and 4-orbit subsets is negligible. The pixel scale has fairly little impact on the derived parameters of extended, well-resolved sources but more so for compact ones. Accordingly, for all but one of our SINS targets, the resulting best-fit $R_e$ and $n$ obtained

from the $0''.038$ and $0''.05$ pixel$^{-1}$ images are nearly identical and within the (small) $1\sigma$–$2\sigma$ uncertainties, depending on the source and parameter. For BX 663, the AGN host with a compact central peak, the changes are significantly larger than for the other five SINS sources although they are formally within $1.5\sigma$ of the best-fit values for each pixel scale.[15]

For the 24 $\mu$m selected dusty IR-luminous sample, Dasyra et al. (2008) did not perform single-component Sérsic profile fitting for their analysis. We thus applied our fitting procedure using their images to obtain the $R_e$ and $n$ for comparison with our sample. The resulting effective radii agree on average within 20%, or $<1\sigma$ based on our fitting uncertainties, with those estimated using the SExtractor software by Dasyra et al. The most important difference (by 30%, or $3\sigma$) occurs for the largest, most diffuse and asymmetric source (MIPS 8242). For our SINS targets, and compared to the nominal fits for the 4-orbit $0''.05$ pixel$^{-1}$ data, the differences resulting from the shallower subsets and larger $0''.076$ pixel$^{-1}$ sampling are typically $\lesssim 3\sigma$. Again, BX 663 shows the largest changes with $R_e$ smaller by $\approx 0.6$–$1.2$ kpc and $n$ lower by $\approx 0.7$–$1$, depending on the subset.

Figure 13 plots the best-fit $n$ index versus $R_e$ of our SINS sample along with those of the $K$-selected and 24 $\mu$m selected comparison samples. In terms of size and Sérsic index, the quiescent sample of van Dokkum et al. (2008) is clearly distinct from our SINS galaxies, with overall significantly smaller $R_e$ and typically higher $n$ values. The Kriek et al. (2009) objects are intermediate between the passive objects of van Dokkum et al. and our actively star-forming SINS sources with, as already discussed by Kriek et al., a clear separation between the AGN sources that have sizes and $n$ indices in a narrow range and fully

---
[15] Specifically, the best-fit $R_e$ and $n$ for the finer $0''.038$ pixel$^{-1}$ sampling are $3.6^{+6.2}_{-0.3}$ kpc and $1.31^{+2.15}_{-0.38}$, respectively, compared to $4.5^{+7.7}_{-0.8}$ kpc and $2.00^{+2.11}_{-0.59}$ for the $0''.05$ pixel$^{-1}$ one.

overlapping with the passive objects whereas the purely star-forming sources span wider ranges shifted toward larger sizes and lower $n$ values.

Quantitatively, our SINS objects lie at the large size − low $n$ end with sample median $R_{e,med} = 5.1$ kpc and $n_{med} = 0.35$ (or 5.7 kpc and 0.33, respectively, when excluding the AGN source BX 663). In the $K$-selected comparison sample, the six star-forming sources have median values of $R_{e,med} = 4.3$ kpc and $n_{med} = 0.95$, the four AGN sources have $R_{e,med} = 1.4$ kpc and $n_{med} = 2.46$, and the nine passive objects have $R_{e,med} = 1.5$ kpc and $n_{med} = 2.30$. Our AGN source BX 663 is not as compact as the Kriek et al. AGNs but, among our SINS sample, it reflects the trend toward lower $R_e$ and higher $n$ of AGN relative to star-forming galaxies seen in the $K$-selected sample. One source (HDFS1-1849) from van Dokkum et al. appears to be an "outlier" with respect to the other eight passive $K$-selected objects: its $R_e = 4.4$ kpc and $n = 0.5$ is clearly more characteristic of the SINS and Kriek et al. (2009) star-forming galaxies. As we will see below, it is also more similar to the star-forming sources in terms of the non-parametric Gini, $\Psi$, and $M_{20}$ coefficients. This object is anomalous within the sample of quiescent galaxies insofar as its broadband SED fit indicates in fact active star formation. The lack of emission lines that formed the basis of the "quiescent" classification may only be due to this object's dusty, edge-on nature (Kriek et al. 2009). Excluding this object, the median values for the eight remaining passive $K$-selected sources are $R_{e,med} = 1.4$ kpc and $n = 2.55$.

With the Dasyra et al. (2008) sample, we can explore variations in different regimes of bolometric luminosity. While the four SINS objects with $Spitzer$/MIPS data are among the most luminous of the rest-UV-selected high $z$ population, their observed $24\,\mu m$ fluxes and total IR luminosities are still on average almost an order of magnitude lower than those of the $24\,\mu m$ selected sources of Dasyra et al. (2008). Overall, the $24\,\mu m$ selected dusty IR-luminous sample is distinct from our SINS objects, and appears to be intermediate between the rest-UV SINS and $K$-selected star-forming galaxies and the $K$-selected passive and AGN objects. The $24\,\mu m$ selected sources have a median size and Sérsic index of $R_{e,med} = 2.6$ kpc and $n_{med} = 1.45$. These values are comparable to the median rest-frame optical structural parameters derived from NIC2 imaging for a sample of high-$z$ submillimeter-selected galaxies by Swinbank et al. (2010), which overlap in bolometric luminosity with the Dasyra et al. objects. Sampled at the same $0\rlap{.}''076\,pixel^{-1}$ scale, and 1- and 2-orbit integration times, the SINS sample has about twice larger $R_{e,med} = 5.4$ kpc and significantly lower $n_{med} = 0.37$. The trend for the $24\,\mu m$ selected sources to lie toward smaller radii and steeper inner profiles with respect to the SINS galaxies may reflect the prevalence of AGN activity among the Dasyra et al. sample (10 out of 11 objects).

### 6.2. Comparison of Morphological Coefficients

Clearly, the various samples probe different regimes in structural parameters, and this appears to be related to both the level of star formation and AGN activity. To further quantify the differences between our SINS galaxies and the comparison samples, we analyzed the images through the non-parametric approach described in Section 4.2.1, using the relevant data sets for the SINS targets matching the depth and pixel sampling of the $K$- and $24\,\mu m$ selected samples. In addition, to take into account the redshift range of our targets and remove the effects of surface brightness dimming, particularly important in this approach, we selected pixels for our analysis as if all objects were observed at the maximum redshift among the three samples, i.e., $z = 2.6$.

We estimated Gini, $\Psi$, and $M_{20}$ for galaxies in the three samples, and the results are shown in Figure 14. All panels contain our SINS galaxies, and the top two panels show $G$ versus $\Psi$ and $G$ versus $M_{20}$, using the $K$-selected sample for comparison. The bottom two panels show the same parameters, but feature the $24\,\mu m$ selected sample for comparison. For the top two panels, the SINS targets have been reanalyzed using 3- and 2- orbit subsets of the data at $0\rlap{.}''038\,pixel^{-1}$, in order to match the depth and sampling of the van Dokkum et al. (2008) and Kriek et al. (2009) images. Given the compact and axisymmetric nature of the quiescent $K$-selected subsample featured in van Dokkum et al., we applied the same non-parametric analysis to our empirical PSF, constructed from multiple stars as described in Section 2.5 but from our $0\rlap{.}''038$ pixel set of images. This analysis indicates that while the quiescent, $K$-selected objects are extremely compact, the majority of them can be distinguished from unresolved point sources, with significantly lower Gini values. For the bottom two panels, our SINS targets have been reanalyzed using 2- and 1-orbit subsets of the data at $0\rlap{.}''076\,pixel^{-1}$, in order to match the depth and sampling of the Dasyra et al. (2008) images. The non-parametric statistics were calculated as well for the empirical PSF sampled with this pixel scale. In all panels, the shallower 3-, 2-, and 1-orbit SINS data subsets result in lower Gini coefficient for a given object, while higher values are obtained for $\Psi$ and $M_{20}$.

The non-parametric morphological analysis reinforces the qualitative visual impression from the images and the results from the Sérsic profile fitting of the different samples of galaxies. The $K$-selected passive and AGN sources occupy a disjoint region of $G - \Psi - M_{20}$ morphological parameter space from that of the SINS targets. They are virtually all offset toward higher Gini, and both lower $\Psi$ and $M_{20}$ values, with sample median values of $G_{med} = 0.54$, $\Psi_{med} = 0.8$, and $M_{20,med} = -1.8$ for the passive galaxies and essentially identical $G_{med} = 0.53$, $\Psi_{med} = 0.8$, and $M_{20,med} = -1.8$ for the AGN sources. As was the case for the structural parameters, only a single galaxy from the $K$-selected passive sample (HDFS1-1849) even approaches the lower Gini (median of 0.28), and higher $\Psi$ (median of 7.8) and $M_{20}$ (median of $-0.5$) values of our SINS sample.[16] In contrast to the passive and AGN objects, the six $K$-selected star-forming objects show considerably more overlap with the SINS sample. The median values for the $K$-selected star-forming sources are $G_{med} = 0.34$, $\Psi_{med} = 3.6$, and $M_{20,med} = -1.4$, which are intermediate between the parameters describing the SINS sample and the $K$-selected passive and AGN objects.

One slight caveat to these results is the difference in typical S/N among the samples, with the $K$-selected quiescent and AGN objects $\sim$2–3 times higher in average surface brightness than the SINS targets, and the $K$-selected star-forming sources $\sim$1.5 times brighter. As discussed by Peter et al. (2007) and Abraham et al. (2007), using a fixed surface brightness threshold (effectively what we have done) will lead to a "truncation bias" in the Gini coefficients estimated for fainter systems, in that their pixel flux distribution functions will be sampled over a smaller dynamic range than those of more luminous objects. To test for the significance of this effect, we applied a higher surface brightness threshold to the $K$-selected samples, such that the resulting pixel flux distribution functions span the same dynamic range as those of our SINS targets. We find $G_{med} = 0.45$ for the

---

[16] These median values represent the ensemble of 3- and 2-orbit subsets of the SINS data shown in Figure 14.
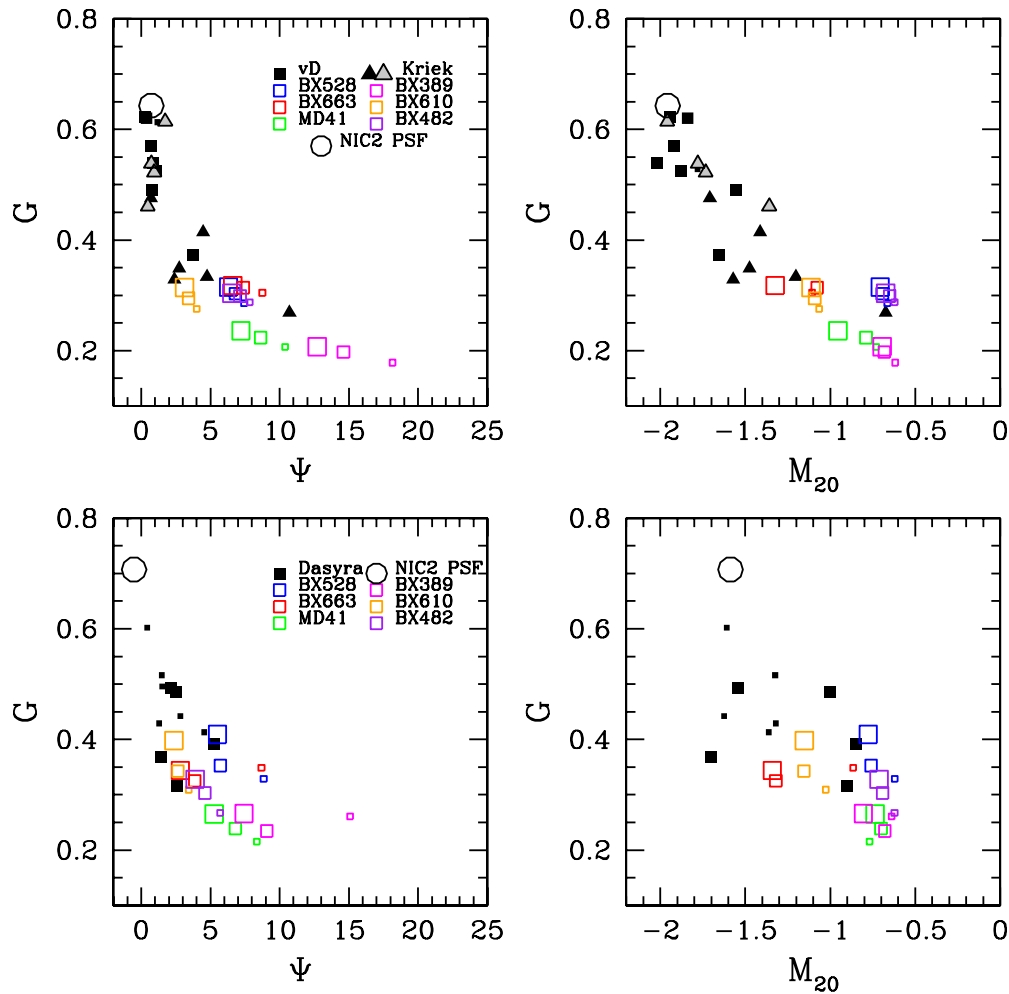
**Figure 14.** Morphological parameters derived from NIC2 $H_{160}$-band imaging for our SINS targets and comparison samples at similar redshifts but with different selection criteria. Each galaxy was analyzed as if it was placed at the maximum redshift of the combined samples, i.e., $z = 2.60$. Top left: Gini vs. $\Psi$ for the SINS and $K$-selected samples (labeled "vD" for objects from van Dokkum et al. 2008 and "Kriek" for objects from Kriek et al. 2009). As in Figure 13, $K$-selected objects are indicated with solid squares (vD) and triangles (Kriek). For vD objects, medium-sized symbols are used for 3-orbit exposures and small symbols for 2-orbit exposures, while, for Kriek objects, all points represent 3-orbit exposures. SINS objects are indicated with open squares, with the largest symbols for 4-orbit exposures, medium-sized symbols for 3-orbit subsets of the data, and small symbols for 2-orbit subsets. Our NIC2 images were drizzled to the 0″.038 pixel sampling of the van Dokkum et al. and Kriek et al. data for consistent comparison. The non-parametric statistics for the empirical PSF constructed from stars in our 0″.038 pixel$^{-1}$ NIC2 images are indicated with an open circle. Top right: Gini vs. $M_{20}$ for the SINS, vD, and Kriek samples. Symbols are the same as in the previous panel. Bottom left: Gini vs. $\Psi$ for the SINS and Dasyra et al. (2008, labeled "Dasyra") samples. Dasyra et al. objects are indicated with solid black squares, with medium-sized symbols for 2-orbit exposures and smaller symbols for 1-orbit exposures. Again, SINS objects are indicated with open squares, with the largest symbols for 4-orbit exposures, medium-sized symbols for 2-orbit subsets of the data, and smallest symbols for 1-orbit subsets. Our NIC2 images were here drizzled to the 0″.076 pixel scale of the Dasyra et al. data, and the non-parametric statistics for the empirical PSF from these images are also indicated with an open circle. Bottom right: Gini vs. $M_{20}$ for SINS and Dasyra et al. (2008) samples. Symbols are the same as in the previous panel.

(A color version of this figure is available in the online journal.)

truncated pixel flux distribution functions for $K$-selected passive and AGN sources, still significantly higher than the median of the SINS sample, and still with no overlap in morphological parameter space. Applying the same type of truncation to the $K$-selected star-forming galaxies, we find very little effect on the sample median properties, with $G_{\mathrm{med}} = 0.33$.

Turning to the properties as a function of bolometric luminosity, in the $G - \Psi - M_{20}$ parameter space, the $24\,\mu$m selected dusty IR-luminous sample separates on average from the SINS sample in the same sense as the $K$-selected sample, if not as significantly as the passive and AGN objects. The median parameter values for the $24\,\mu$m selected dusty IR-luminous sources are $G_{\mathrm{med}} = 0.44$, $\Psi_{\mathrm{med}} = 2.1$, and $M_{20,\mathrm{med}} = -1.2$. Sampled at the same pixel scale and exposure time, the SINS targets have lower Gini (median of 0.30), and higher $\Psi$ (median of 6.4) and $M_{20}$ (median of $-0.6$). The typical S/N of objects

in the two samples is very similar, so no issue of truncation bias applies in this comparison. These quantitative morphological results confirm again the qualitative visual impression that our SINS targets have systematically more irregular, extended, and clumpy morphologies than those of the $24\,\mu$m selected dusty IR-luminous sample of Dasyra et al. (2008).

Luminous dusty systems with $L_{\mathrm{IR}} > 10^{12}\,L_{\odot}$ are commonly associated with major mergers in the local universe (e.g., Genzel et al. 2001). The $24\,\mu$m selected sample of Dasyra et al. (2008) falls well above this luminosity threshold, yet the processes giving rise to extreme bolometric luminosities at high redshift may be more diverse, based on theoretical grounds (e.g., Davé et al. 2010), and supported by observational evidence (e.g., Dasyra et al. 2008; Swinbank et al. 2010). Dasyra et al. find roughly 50% of their full NIC2 sample to appear morphologically "quiescent." Furthermore, consistent with the
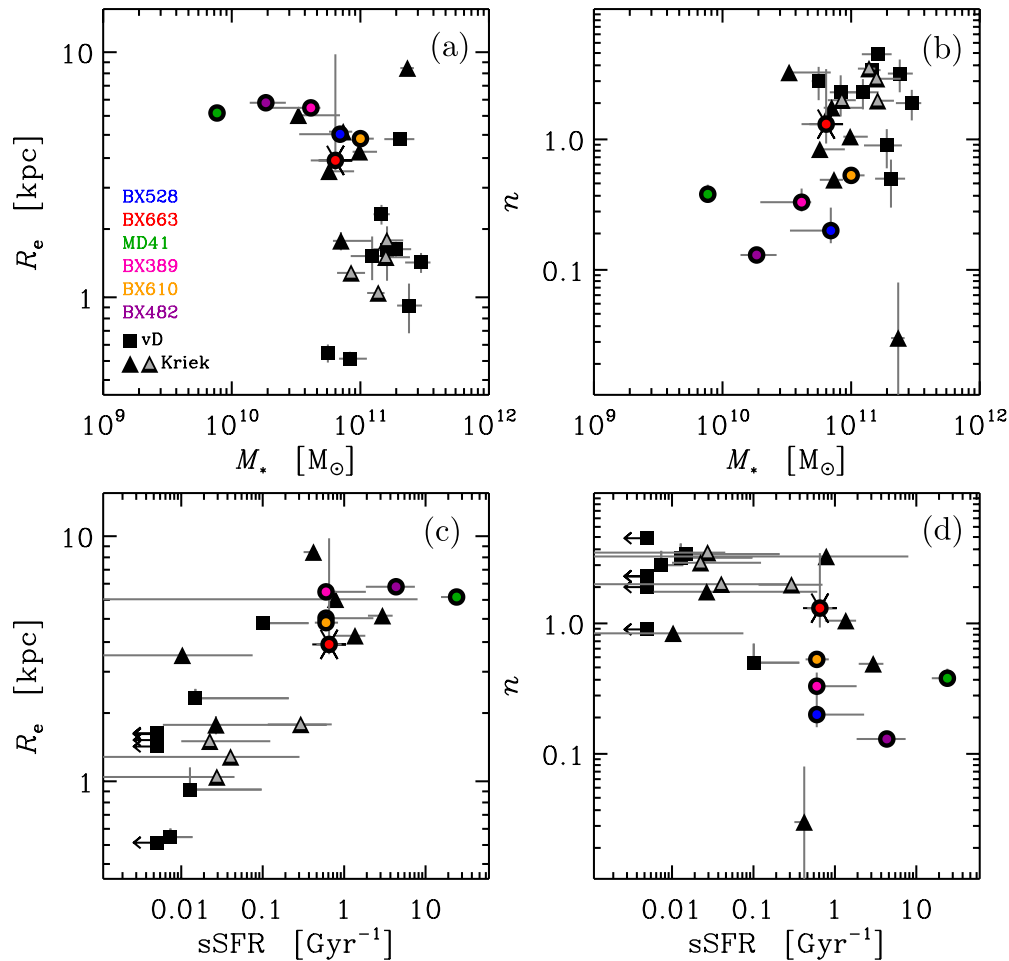
**Figure 15.** Structural parameters of our six SINS galaxies and of the $K$-selected comparison sample from van Dokkum et al. (2008, "vD") and Kriek et al. (2009, "Kriek"), plotted as a function of global stellar properties. (a) Effective radius $R_e$ vs. stellar mass $M_\star$. (b) Sérsic index $n$ vs. $M_\star$. (c) $R_e$ vs. specific star formation rate (sSFR). (d) $n$ vs. sSFR. Symbols and colors are the same as in Figure 13, and labeled in panel (a). All stellar masses are for a Chabrier (2003) IMF. In the range of $M_\star$ where our SINS objects and the $K$-selected samples overlap, the data reflect the wide range in size (and in $n$) that is known to exist for galaxies of similar stellar masses and out to $z \sim 3$. Size and star formation activity are clearly correlated, again as seen for the massive galaxy population locally and at high redshift.

(A color version of this figure is available in the online journal.)

results of Kriek et al. (2009), these authors show that objects in their sample with mid-IR AGN signatures also tend to have more compact rest-frame optical morphologies than those with starburst-dominated spectra. Given that all but one object in the Dasyra et al. $z = 2.0$–2.5 subsample show evidence of AGN activity, the 24 $\mu$m selected dusty IR-luminous galaxies included in Figure 14 are among the more compact objects in the full Dasyra et al. sample. Dasyra et al. hypothesize that 24 $\mu$m selected IR-luminous objects, with warmer mid-IR/far-IR colors than the submillimeter-selected IR-luminous high $z$ population (Chapman et al. 2003), may represent the merged, dynamically relaxed counterparts of the (major-) merging submillimeter galaxies. On the other hand, the rest-frame optical structural parameters and sizes of submillimeter galaxies as presented by Swinbank et al. (2010) are very similar to those of the 24 $\mu$m selected IR-luminous objects. A more careful morphological comparison of the two bolometrically luminous samples is clearly required to construct an evolutionary sequence.

### 6.3. The Connection between Structure and Stellar Populations in $z \sim 2$ Galaxies

In analogy with trends seen in the local universe (Kauffmann et al. 2003; Shen et al. 2003), the structural properties of $z \sim 2$

galaxies appear to be correlated with their stellar populations. Based on imaging with both NICMOS/NIC3 from space (Zirm et al. 2007; Toft et al. 2007), and with VLT/ISAAC (Franx et al. 2008; Toft et al. 2009) and UKIRT/WFCAM (Williams et al. 2010) from the ground, it has been shown that quiescent, high-redshift galaxies have systematically smaller sizes and higher stellar mass surface densities than actively star-forming systems. Based on the sample of 19 $K$-selected galaxies discussed in the previous subsections, Kriek et al. (2009) used their higher resolution NICMOS/NIC2 imaging to demonstrate that specific SFR and rest-frame $U - B$ color are strongly correlated with galaxy structural parameters. We here examine the structural properties in connection with the stellar populations for our SINS sample, complemented with the van Dokkum et al. (2008) and Kriek et al. (2009) $K$-selected samples for which stellar properties from SED modeling are available.

As proxies for galaxy stellar populations, we consider the stellar mass and specific SFR. Within our SINS NIC2 sample, the absence of correlation between morphology and stellar population properties includes parameters derived from Sérsic models ($R_e$ and $n$) as well as the non-parametric morphological coefficients ($G$, $\Psi$, and $M_{20}$). This result echoes previous ones from Law et al. (2007b) and Peter et al. (2007)
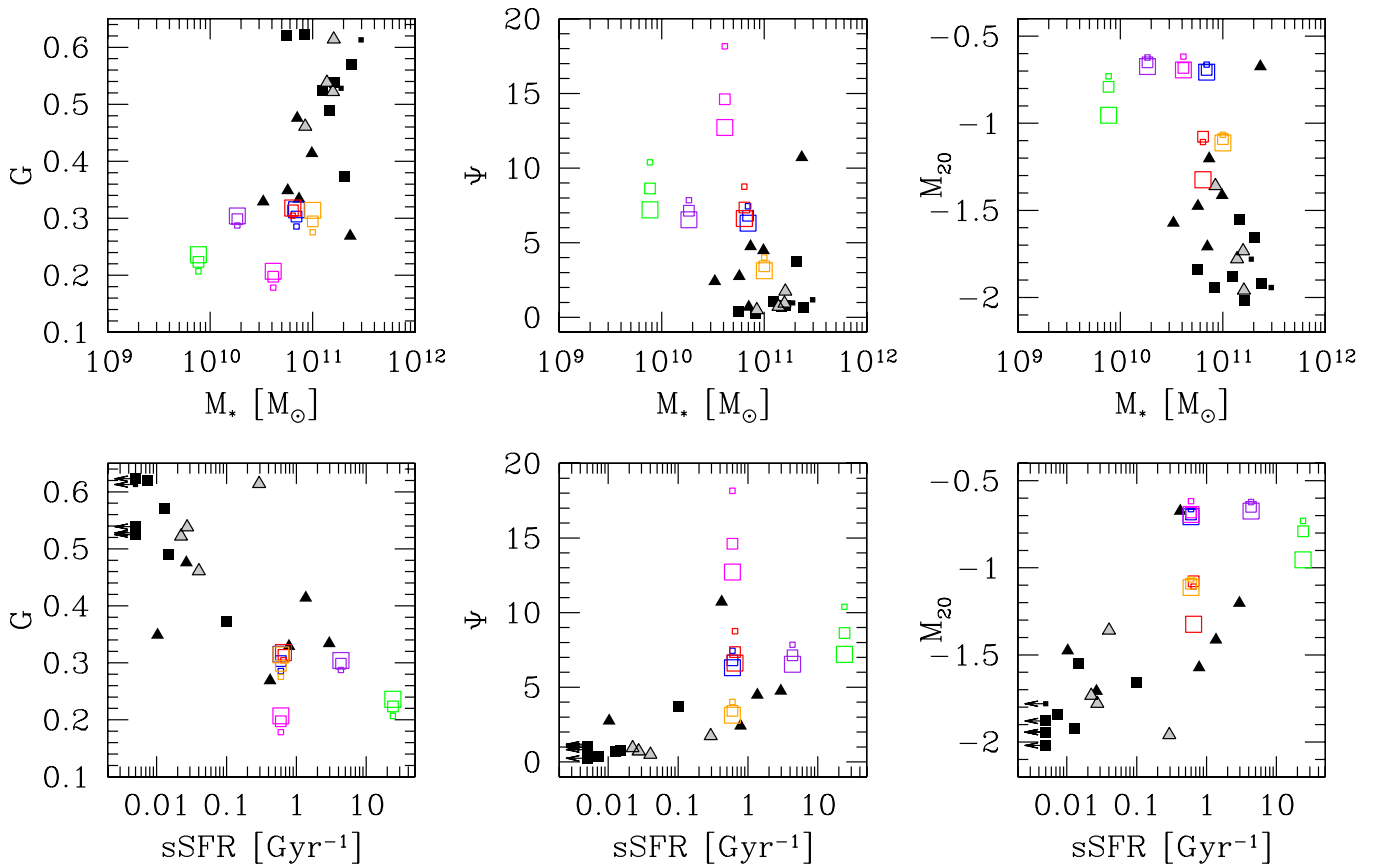
**Figure 16.** Same as Figure 15, but for the non-parametric morphological coefficients. The top row shows morphological coefficients plotted as a function of $M_\star$, while the bottom row shows them as a function of specific SFR. As for the structural parameters ($R_e$ and $n$), a large diversity of non-parametric morphological coefficients are found in the region of overlapping $M_\star$, while significant correlations are found between morphology and specific SFR.

(A color version of this figure is available in the online journal.)

demonstrating a lack of correlation between stellar populations and rest-UV morphologies for UV-selected galaxies at $z \sim 2$. However, as described by Peter et al. (2007) the UV-selected galaxies do not span the full range of stellar population properties that exist at $z \sim 2$ (see also, e.g., van Dokkum et al. 2006; M. Damen et al. 2011, in preparation). The $K$-selected sample with NIC2 imaging from van Dokkum et al. (2008) and Kriek et al. (2009) ideally augments our SINS NIC2 sample in this respect, considerably extending the range probed in specific SFR by over two orders of magnitude, in the same redshift range and at comparable stellar masses as our SINS targets.

Figures 15 and 16 combine the morphological properties of our SINS and $K$-selected samples, now plotted as a function of the stellar mass and specific SFR derived from SED modeling. The SINS and $K$-selected samples overlap in stellar mass over the range from $\approx 3 \times 10^{10}$ to $\approx 10^{11} M_\odot$. Over this range, there is significant diversity in structural parameters, with the SINS targets exhibiting the largest $R_e$, smallest $n$, largest $\Psi$ and $M_{20}$, and smallest $G$ values. At the other extreme, we find the AGN and quiescent $K$-selected galaxies, with the star-forming $K$-selected galaxies showing intermediate properties. More specifically, over this interval in stellar mass, the galaxies cover a wide range in $R_e$, consistent with the spread of about an order of magnitude in rest-frame optical sizes for $z \sim 2$ galaxies of similar masses found in previous studies (e.g., Trujillo et al. 2006; Zirm et al. 2007; Toft et al. 2007, 2009; Franx et al. 2008).

On the other hand, the $K$-selected and SINS samples separate more cleanly in specific SFR. A clear sequence of increasing specific SFR is represented, respectively, by the quiescent and AGN $K$-selected galaxies, the star-forming $K$-selected galaxies, and the SINS sample. In turn, significant connections with specific SFR are found for every morphological coefficient considered here, with systematically higher $R_e$, $\Psi$, and $M_{20}$, and systematically lower $n$ and $G$, as the specific SFR increases. These strong trends with star formation activity are consistent with the previous work from Toft et al. (2007, 2009), Zirm et al. (2007), and Franx et al. (2008), but are based on higher resolution NIC2 imaging. Furthermore, they extend the NIC2-based correlations between morphology and stellar populations from van Dokkum et al. (2008) and Kriek et al. (2009) toward higher specific SFR values. The results presented here reinforce the conclusion by Franx et al. (2008) that galaxy structural parameters are better correlated with specific SFR and color than with stellar mass. These results highlight the fact that stellar mass alone is not a good predictor of structural parameters, nor of detailed morphologies as we find from our non-parametric morphological analysis.

In that respect, it is also interesting to consider morphologies as a function of the stellar mass surface density of the galaxies. Indeed, in the local universe, the specific SFR (as well as rest-frame optical colors) is observed to be much more closely related to stellar mass surface density than to stellar mass (e.g., Kauffmann et al. 2003, 2006, for the Sloan Digital Sky Survey
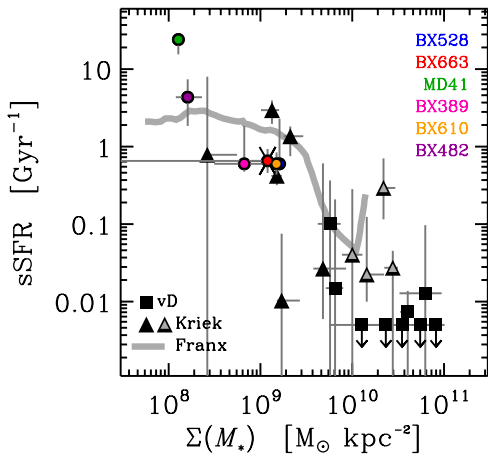
**Figure 17.** Same as Figure 15, but for the specific star formation rate as a function of the stellar mass surface density. Half of the total stellar mass is assumed to be enclosed within a radius corresponding to the circularized effective radius $R_{e\,circ} = R_e \sqrt{b/a}$, giving estimates of the projected surface density. There is a clear trend outlined by our SINS targets and the $K$-selected comparison samples of van Dokkum et al. (2008) and Kriek et al. (2009), which span overall three orders of magnitude in stellar mass surface density and even more in specific SFR (a similar trend is seen when using the $R_e$ instead for estimates of the deprojected surface density). For comparison with the more general massive galaxy population at $z \sim 2$, the median relationship derived by Franx et al. (2008) from a large $K$-selected sample in GOODS-S and based on ground-based near-IR imaging to derive rest-frame optical sizes is overplotted as a gray thick line. Our SINS and the $K$-selected comparison samples consistently follow this relationship.

(A color version of this figure is available in the online journal.)

(SDSS) sample), and these relationships are found to persist out to at least $z \sim 2$ (Franx et al. 2008; Maier et al. 2009). This trend is again reflected among the SINS and $K$-selected samples discussed here. Figure 17 plots the specific SFR as a function of the projected stellar mass surface density $\Sigma(M_\star)$ of the objects. We calculated the surface density assuming that the observed 1.6 $\mu$m light (rest-frame $\approx$5000 Å) from the NIC2 images traces well the stellar mass (as we will demonstrate for one of our SINS targets in Section 7.1), and thus that half of the total stellar mass is enclosed at $r < R_e$. We find a clear trend of decreasing specific SFR with increasing mass surface density, which is fully consistent with the median relationship at $z \sim 2$ derived by Franx et al. (2008). Our six actively star-forming SINS targets lie at the lower end of projected mass surface density with median of $\log(\Sigma(M_\star)\,[M_\odot\,\mathrm{kpc}^{-2}]) = 9.0$ (or 8.8 when excluding the AGN source BX 663) and the nine quiescent galaxies of van Dokkum et al. (2008) lie at the higher end with median of $\log(\Sigma(M_\star)\,[M_\odot\,\mathrm{kpc}^{-2}]) = 10.5$ (or 10.6 when omitting the anomalous HDFS1-1849). The ten emission line galaxies of Kriek et al. (2009) span the intermediate range, with sample median of $\log(\Sigma(M_\star)\,[M_\odot\,\mathrm{kpc}^{-2}]) = 9.5$. Among these objects, the subsamples of six star-forming and four AGN sources have, respectively, lower and higher mass surface densities (median values of $\log(\Sigma(M_\star)\,[M_\odot\,\mathrm{kpc}^{-2}]) = 9.2$ and 10.3). Since the structural and morphological properties of the SINS and $K$-selected samples considered here are strongly connected with the specific SFR, it follows from the specific SFR versus $\Sigma(M_\star)$ trend that they are also closely related to the stellar mass surface density. We note here that the high-$z$ submillimeter-selected galaxies of Swinbank et al. (2010) have properties implying on average both higher specific SFR and $\Sigma(M_\star)$ than the SINS galaxies, and do not follow the median relationship of Franx et al. (2008), pointing toward differences in their assembly histories.

## 7. DISCUSSION

### 7.1. Rest-frame UV Structure, Colors, and Mass Distribution of MD 41

In this section, we focus on MD 41, the target among our NIC2 sample with additional high-resolution optical imaging with *HST*/ACS. We first combine the ACS and NIC2 images to compare the structural parameters derived from the rest-frame UV and optical surface brightness distributions. We then use the observed optical-to-near-IR color map to construct the spatially resolved stellar mass map of the galaxy.

#### 7.1.1. Rest-frame UV Structural Parameters

In Section 4.2, we presented the ACS F814W image that exists for one of our NIC2 targets, MD 41. The fairly similar appearance of this galaxy in the ACS $i_{814}$ and NIC2 $H_{160}$ bands (Figure 8) is supported by our quantitative non-parametric analysis, which yields very comparable $G$, $\Psi$, and $M_{20}$ values for both images. Here we extend the comparison to the structural parameters between the $H_{160}$- and $i_{814}$-band images. This comparison also complements the one in Section 5.2, where we found that the size, Sérsic index, and axis ratio are very similar between the H$\alpha$ and rest-frame $\approx$5000 Å continuum emission for all our targets at a common (PSF-matched) $\approx$0″.5 resolution. At the redshift of MD 41 ($z = 2.17$), the ACS $i_{814}$ band probes rest-frame $\approx$2600 Å light, predominantly tracing young massive stars similarly to H$\alpha$. Therefore, the ACS+NIC2 imaging allows us to examine the relative surface brightness distributions of different stellar populations at significantly higher resolution than possible with the SINFONI seeing-limited H$\alpha$ data available for MD 41, although with the caveat that extinction effects are more important at rest-frame $\approx$2600 Å than at $\sim$5000–6500 Å mapped by the $H_{160}$ band and H$\alpha$ observations.

We repeated our Sérsic model fitting procedure (Section 4.1.1) on the ACS $i_{814}$-band image of MD 41. For consistent comparison with the results from the NIC2 $H_{160}$-band image, we first convolved the ACS data to the spatial resolution of the NIC2 data. We constructed an empirical PSF for the ACS data using ten bright but unsaturated, isolated stars identified across the full map. From a Gaussian fit, the PSF FWHM is 0″.099 with ellipticity of 0.02 (or FWHM = 0″.080 and same ellipticity for a Moffat profile fit). The smoothing kernel was computed through a Lucy–Richardson deconvolution algorithm, and the curves of growth of the NIC2 and smoothed ACS PSFs agree to better than 10% at radii 0″.1 $< r <$ 1″.5. No spatial resampling of the data is needed since both ACS and NIC2 data sets were drizzled to 0″.05 pixels. For accurate registration between the NIC2 and ACS maps, we relied on the star and a number of very compact sources visible in both $H_{160}$- and $i_{814}$-band emission within the smaller NIC2 FOV. The right panel of Figure 8 shows an RGB color composite with the $H_{160}$-band image in red and the PSF-matched $i_{814}$-band image in green+blue.

The best-fit parameters based on the smoothed ACS map are $R_e(i_{814}) = 7.44^{+0.59}_{-0.71}$ kpc, $n(i_{814}) = 0.27^{+0.45}_{-0.09}$, $b/a(i_{814}) = 0.30^{+0.12}_{-0.02}$, and P.A.$(i_{814}) = 38.8^{+1.3}_{-1.6}$ deg. Compared to the parameters derived from the NIC2 image (Table 4), the effective radius is thus $\approx$30% larger, the Sérsic index is $\approx$0.25 lower, and the axis ratio and P.A. are virtually identical. The larger size and lower light concentration index derived from the $i_{814}$-band image could be due to higher extinction in the central regions and/or more extended distribution of the young stellar population dominating the rest-UV emission. While the differences
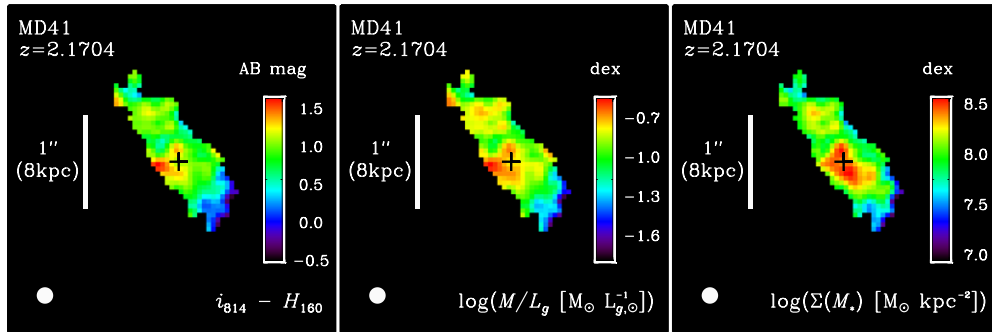
**Figure 18.** Color, observed mass-to-light ratio, and stellar mass maps of MD 41. North is up and east is to the left in all panels, and a bar of 1″ in length (approximately 8 kpc at the redshift of the source) indicates the scale in the images. Left: observed $i_{814} - H_{160}$ colors from the ACS/F814W and NIC2/F160W images, matched to the same PSF with FWHM indicated by the filled circle at the bottom left corner. Middle: observed stellar mass to rest-frame $g$-band light ratio, computed from the $i_{814} - H_{160}$ colors using the relationship derived in the Appendix. Right: stellar mass surface density, derived from the $M_\star/L_g^{rest}$ ratio of the previous panel and the NIC2 $H_{160}$-band map. Pixels with an S/N > 3 in each of the ACS/F814W and NIC2/F160W images are shown, while others are masked out.

(A color version of this figure is available in the online journal.)

in derived size and $n$ index are significant with respect to the uncertainties, the fits to the $i_{814}$ and $H_{160}$-band images are in broad agreement. Both indicate that MD 41 is a large and fairly edge-on system (implied disk inclination angle of $\approx 72°$), with a shallow inner light profile. The structural analysis supports the conclusions from the non-parametric morphological analysis that there is no strong $k$-correction between the rest-frame UV and optical morphologies for MD 41. This result is consistent with the general findings for rest-UV-selected samples at $z \sim 2$, and in contrast to those for samples selected at longer wavelengths with typically redder rest-frame optical colors (Dickinson et al. 2003; Peter et al. 2007; Law et al. 2007b; Toft et al. 2007; see also Overzier et al. 2010 for rest-UV-selected samples at $z \sim 3$–4 and rest-optical-selected samples at $z \sim 2$).

### 7.1.2. Rest-frame Colors, Mass-to-light Ratio, and Mass Distribution

We can further exploit the ACS and NIC2 images to investigate spatial variations in observed colors and mass-to-light ratio, and derive the stellar mass distribution within MD 41. In Figure 18, the left panel shows the observed $i_{814} - H_{160}$ color map, over the region for which the pixel flux densities have S/N > 3 in each of the ACS and NIC2 map. The observed colors are fairly uniform across most of the disk of MD 41, with mean and median of $(i_{814} - H_{160})_{AB} = 0.8$ and 0.9 mag, respectively, and standard deviation of 0.37 mag. This compares reasonably well with the integrated color of 0.63 measured in a circular aperture of 3″ diameter.[17] Only two small regions exhibit significantly different colors: the southwestern edge of MD 41 at the location of the two brightest clumps in $i_{814}$ emission with bluer colors $((i_{814} - H_{160})_{AB} \approx 0.2$ on average), and an area around the center of the galaxy characterized by redder colors $((i_{814} - H_{160})_{AB} \approx 1.2$ mag on average).

To interpret the color map of MD 41, we turn to synthetic colors and $M/L$ ratios calculated for the $z = 2.2$ of MD 41 from Bruzual & Charlot (2003) models for a range of ages, extinction, SFHs, and two stellar metallicities (solar and 1/5 solar). The details are given in the Appendix. Stellar age, extinction, and SFH are highly degenerate in observed $i_{814} - H_{160}$ colors (or rest-frame 2600–5000 Å colors at the redshift of MD 41). However, there is a fairly well defined relationship between the

stellar mass to rest-frame optical light ratio (with luminosity uncorrected for extinction) and the observed colors, with very little dependence on our choice of metallicity. For our purposes, we used model predictions through the SDSS $g$-band filter, a good approximation to the rest-frame $\approx 5000$ Å luminosity probed by the NIC2 F160W filter (see the Appendix).

We thus derived a mean relationship between the observed (uncorrected for extinction) $M_\star/L_g^{rest}$ ratio and observer's frame $i_{814} - H_{160}$ colors for $z = 2.2$. We used this relationship to compute the $M_\star/L_g^{rest}$ ratio map of MD 41, shown in the middle panel of Figure 18. Unsurprisingly, the $M_\star/L_g^{rest}$ ratio map looks similar to the $i_{814} - H_{160}$ map, given the roughly linear relation (in logarithmic units for the $M/L$). The mean and median values of individual pixels are $\log(M_\star/L_g^{rest}[M_\odot L_{g,\odot}^{-1}]) \approx -0.9$, with standard deviation of $\approx 0.2$ dex. The observed integrated color gives nearly the same value, $-0.83$, while the model with best-fit parameters from the optical/near-IR SED modeling for MD 41 (Table 3) has a somewhat lower value of $-1.08$. An average value of $\approx -1.3$ is measured in the regions of bluest colors at the southwestern edge of MD 41, and of $\approx -0.7$ in the redder regions around the center. The fairly small scatter among individual pixels implies roughly constant observed $M_\star/L_g^{rest}$ ratio across most of the galaxy.

Multiplying the observed $M_\star/L_g^{rest}$ map by the $H_{160}$-band image as a proxy for the extrinsic rest-frame $g$-band luminosity then leads to the spatial distribution of stellar mass across MD 41. The map of projected stellar mass surface density $\Sigma(M_\star)$ is shown in the right panel of Figure 18. It is remarkably similar to the $H_{160}$-band image itself, indicating that the observed 1.6 $\mu$m emission does trace closely the stellar mass distribution in MD 41. The typical (mean, median) values of individual pixels is $\log(\Sigma(M_\star [M_\odot$ kpc$^{-2}])) \approx 8.0$, with standard deviation of 0.3 dex. At the largest radii probed, and especially on the southwestern edge, the surface density drops to $\log(\Sigma(M_\star)) \approx 7.5$, and it increases toward the center by about an order of magnitude to $\log(\Sigma(M_\star)) \approx 8.4$. The deprojected surface density from the total stellar mass of MD 41, assuming half of it is enclosed within a radius of $R_e$, is $\log(\Sigma(M_\star, r < R_e)) = 7.6$; for this fairly inclined system, this increases significantly when considering the projected surface density to $\log(\Sigma(M_\star, r < R_e)) = 8.1$, virtually the same as inferred on average at individual locations across the galaxy. Compared to the properties derived for massive $1.5 < z < 2.5$ galaxies by Franx et al. (2008; see also Figure 17), MD 41 lies at the low surface mass density end, consistent with its high specific

---

[17] The two blue sources offset from the main part of MD 41 to the northwest and southeast that are detected in the ACS image but not in the NIC2 image are included in this large aperture, and so contribute to this estimated integrated color.

SFR of 24 Gyr$^{-1}$ and blue estimated integrated rest-frame $(U - B)_{AB} \approx 0.5$ color.

The total stellar mass obtained by summing up the inferred stellar mass of individual pixels with S/N > 3 in the $i_{814}$- and $H_{160}$-band images is $7.3 \times 10^9$ $M_\odot$, or 95% of the value derived from the modeling of the integrated optical/near-IR SED (Section 3.3). The sum of the $H_{160}$-band flux densities over the same pixels corresponds to 65% of the total as measured in a 3$''$diameter aperture (Section 3.2). Multiplying the S/N > 3 pixels' luminosity densities by the $M_\star/L_g^{rest}$ from the best-fit SED model of MD41 results in a stellar mass of only $5.0 \times 10^9$ $M_\odot$. This difference with respect to the spatially resolved estimate reflects the difference between the pixel-averaged $M_\star/L_g^{rest}$ and that from the integrated SED noted above. It suggests the total SED-derived stellar mass may be underestimated by $\approx 30$% because dustier and/or more evolved, redder stellar populations are under-represented in the effectively luminosity-weighted integrated rest-UV and optical photometry of MD 41. A similar effect between stellar masses computed by integrating spatially resolved mass maps and by modeling unresolved photometry was found for nearby galaxies (Zibetti et al. 2009). This effect may be more important for MD 41 (possibly also for BX 482) because the SED fits rely more heavily on the rest-UV photometry than for the other galaxies with better rest-optical coverage (three near-IR bands compared to two for MD 41 and one for BX 482).

Our analysis of ACS $i_{814}$ and NIC2 $H_{160}$-band imaging of MD 41 shows modest variations in the $M_\star/L_g^{rest}$ ratio, within a factor of ~1.5 over most of the galaxy and on spatially resolved scales as small as $\approx 1.2$ kpc. In addition, the results indicate that the 1.6 $\mu$m (rest-frame $\approx 5000$ Å) is a fairly good tracer of the stellar mass distribution of MD 41. The spatially resolved color-based mass map suggests nevertheless that luminosity-weighting biases may have led to a $\approx 30$% underestimate of the total stellar mass based on modeling of the integrated SED of MD 41. It will undoubtedly be interesting to investigate this effect more systematically with larger high $z$ galaxy samples from combined high-resolution optical and near-IR imaging in future studies.

## 7.2. The Sizes of our SINS NIC2 Sample Galaxies

Size is a fundamental property of galaxies. The redshift evolution of disk sizes and scaling relations involving size (e.g., size–velocity, size–mass) set sensitive constraints on the coupling between the baryonic and dark matter, on the mechanisms through which disks acquire their angular momentum, and on the physical processes that drive galaxy growth (e.g., White & Rees 1978; Fall & Efstathiou 1980; Blumenthal et al. 1984; Dalcanton et al. 1997; Mo et al. 1998; Navarro & Steinmetz 2000). Size determinations, however, can be affected by various factors, and reconciling observed sizes with theoretical predictions remains a challenge (e.g., Dutton et al. 2007; Dutton & van den Bosch 2009; Dutton et al. 2011; Somerville et al. 2008; Sales et al. 2009; Burkert et al. 2010). In the following, we consider whether the sizes derived for our NIC2 sample are affected by their particular morphologies and interpret them in the broader context of the size distribution of the general $z \sim 2$ galaxy population. Our sample has high-quality data that allow, for the first time, a reliable and consistent comparison of rest-frame optical continuum and H$\alpha$ sizes, and we discuss implications for disk formation at high redshift.

### 7.2.1. Rest-frame Optical Continuum and Hα Sizes

It is clear from our NIC2 images that galaxies at $z \sim 2$ can have complex, clumpy, and irregular morphologies even in the rest-frame optical (see also, e.g., Papovich et al. 2005; Toft et al. 2007; Zirm et al. 2007; Dasyra et al. 2008; Kriek et al. 2009). Depending on the importance of the substructure, the overall radial light profiles may or may not be well reproduced by a simple smooth model (see Figures 4–6), and this substructure may also contribute to the observed scatter in light concentration index. This can complicate the measurement and interpretation of sizes in a broader context. For our NIC2 targets, we estimate in Paper II that the clumps identified in rest-frame optical continuum light contribute individually typically only ~2% of the total emission of the host galaxy; their total contributions range between ~10% and ~25% (15% on average), depending on the object. Therefore, for these six galaxies, the impact of the substructure associated with the clumps, spread across the galaxies, probably does not affect the size measurements in an important way.

As we found in Section 4.1.2, the kinematically identified disks have global radial light profiles that deviate appreciably from pure exponential disks, with best-fit Sérsic indices $n \approx 0.15$–0.6, or $n \approx 2$ for the AGN source BX 663. The impact of fitting exponential disks to our NIC2 targets is, however, relatively modest. Excluding the major merger BX 528, single-component Sérsic model fits to the 0$''$145 resolution $H_{160}$-band images with fixed $n = 1$ yield the following changes: the effective radii mostly increase, with mean and median $R_e(n = 1)/R_e(n \text{ free}) \approx 1.15$, and range of 0.8–1.45. All $n < 1$ sources have $R_e(n = 1) > R_e(n \text{ free})$ (with mean/median factor $\approx 1.2$ and range of 1.1–1.45), whereas BX 663 with $n = 2$ has $R_e(n = 1) = 0.8 \times R_e(n \text{ free})$. For fits to the H$\alpha$ maps at $\approx 0''5$ resolution, where all five disks have a best-fit $n < 1$ (Table 5), the $R_e(n = 1)$ are larger compared to $R_e(n \text{ free})$ by a factor of 1.1 on average and median, ranging from 1.0 to 1.14.

As discussed in Section 6.3, the rest-frame optical sizes derived for our massive and actively star-forming targets, though large, are fully consistent with the trend of increasing effective radius at higher specific SFR and lower stellar mass surface density observed among the general massive galaxy population at high redshift. While the objects studied in this paper include some of the larger galaxies from the SINS survey (Figure 3), they lie well within the distribution of sizes derived for $1.5 < z < 2.5$ galaxies at very similar rest-frame optical wavelengths (close to $g$ band) and in the relevant stellar mass range of $\log(M_\star [M_\odot]) = 9.9$–11.0 by Franx et al. (2008), which span $R_{e,circ} \sim 0.5$–8 kpc. Our targets have $R_{e,circ} = 2.6$–4.3 kpc, which places them within the upper half of the full distribution. The substantial scatter by roughly an order of magnitude in rest-frame optical (circularized) effective radius at fixed stellar mass is seen at all redshifts up to $z \sim 2.5$ and is attributed, at least in part, to the wide range of SFRs and histories among galaxies (e.g., Shen et al. 2003; Kauffmann et al. 2003; Trujillo et al. 2006; Franx et al. 2008; Toft et al. 2009; and see Figure 15). This scatter as well as the relationships between size, star formation activity, stellar mass, and stellar mass surface density mean that sample properties and selection biases need to be considered for consistent comparisons with other galaxy samples as well as theoretical predictions.

The rest-frame $\approx 5000$ Å continuum probed by our NIC2 data is more sensitive to lower-mass, longer-lived stars making up the bulk of the stellar mass while the H$\alpha$ emission is dominated by the young, short-lived stars. One might expect to be able

to discern with these data possible differences between the distributions of stellar mass and of star formation, if any. For all our SINS NIC2 galaxies, however, we find very close agreement between the parameters derived from the $H_{160}$ band and H$\alpha$ maps, with on average the same effective radius and Sérsic index to within 3% and 0.08, respectively (Section 5.2 and Figure 13). This similarity in size and global profile shape is probably not due to beam-smearing effects, which we found to be not very significant for our targets based on the $H_{160}$-band images at the original NIC2 resolution and convolved to the typical $\approx 0\rlap{.}{''}5$ resolution of the SINFONI data as well as on the seeing-limited and AO-assisted H$\alpha$ maps of BX 482.

These results, albeit for a small sample, are interesting to consider in the context of models of disk formation, where a signature of "inside-out" scenarios for the growth of stellar disks is that the half-mass radius of the recently formed stars, "$R_{\rm e}$(SF)," is larger than the half-mass radius from the total stellar mass, "$R_{\rm e}(M_\star)$." In particular, in the semi-analytical models of Dutton et al. (2011; see also Dutton 2009), the $R_{\rm e}$(SF) is on average a factor of $\approx 2$ larger than $R_{\rm e}(M_\star)$ for $z \sim 2$ disks. Using cosmological hydrodynamical simulations, Sales et al. (2009) find a similar difference by a factor of $\approx 1.8$ at $z \sim 2$. To account for radial variations in mass-to-light ratio across their model disks, Dutton et al. (2011) also compute half-light radii in several rest-frame optical and near-IR bands, and find that the differences between half-light radii and half-mass radius of recent star formation decreases toward bluer bands. For the $V$ band, the bandpass that most closely matches the rest-frame emission probed by the $H_{160}$ observations of our targets, the models of Dutton et al. imply on average $R_{\rm e}$(SF)/$R_{\rm e}(V) \approx 1.26$. In these models, "recent star formation" refers to stars formed in the last $\approx 30$–100 Myr, and we assume here that it is traced reliably by H$\alpha$. Excluding the major merger BX 528, the rest-frame optical radii derived from the NIC2 images matched to the PSF of the SINFONI H$\alpha$ data in Table 5 give on average $R_{\rm e}$(H$\alpha$)/$R_{\rm e}(H_{160})$ = 1.06 (and 1.02 for the median), ranging from $\approx 0.95$ (MD 41, BX 482) to $\approx 1.15$ (BX 663, BX 610). These results for fits where $n$ was left as a free parameter are appropriate for comparison with the Dutton et al. (2011) models, in which disks are not formally exponential. For completeness, the same comparison based on fits with $n$ fixed to 1 gives an average $R_{\rm e}$(H$\alpha$)/$R_{\rm e}(H_{160})$ ratio of 1.10 (median of 1.08), in the range $\approx 1.0$–1.2. Formally, the uncertainties of individual objects would allow ratios of $\approx 1.25$ but the trend of ratios $\approx 1.05$–1.1 (with standard deviation of 0.1) for the ensemble of our five $z \sim 2$ disks indicates little, if any, systematic difference between the H$\alpha$ and rest-frame optical sizes.

We conclude from the considerations above that the size measurements of our SINS NIC2 targets appear robust against possible biases due to substructure, or to specific assumptions on the light profile as tested with fixed $n = 1$ fits to our disks. We estimated the impact of substructure or of adopting $n = 1$ models to all be within typically $\sim 15\%$. Based on the NIC2 and SINFONI data of the five disks among our sample, we do not detect a clear effect whereby the distribution of the actively star-forming regions would be characterized by a larger effective radius relative to that of stars tracing more closely the bulk of the stellar mass. It would be premature to generalize this finding from a small number of galaxies and draw conclusions on the "inside-out" scenario of disk formation, but our high-quality NIC2 and SINFONI data provide a first set of direct empirical constraints at $z \sim 2$ for theoretical models. The sizes of all our six galaxies with $R_{\rm e} \approx 4$–6 kpc (or $R_{\rm e,circ} \approx 2.5$–4.5 kpc) are

not surprisingly large when placed in the broader context of the massive $z \sim 2$ galaxy population, taking into account their properties in conjunction with the existing trends of larger sizes at high specific SFR and low stellar mass surface density.

### 7.2.2. Possible Caveats

There are several possible caveats to the analysis presented in the previous subsection. In particular, our simple Sérsic model fits do not account for multi-component structure. As a specific example, if there is a significant bulge, the $R_{\rm e}$ from single-component model fits will tend to underestimate the $R_{\rm e}$ for the disk itself. The $H_{160}$-band radial light profiles do not indicate the presence of a significant bulge component in our disks (Figure 6), and this is further supported by the low Sérsic indices and relatively small Gini coefficients (Figures 13 and 14). The exception may be BX 663 but it is unclear whether, and by how much, the AGN in this object may contribute to the central emission peak. The two-component fits for BX 663 explored in Section 4.1.2 imply a very minor fraction of 6% of the total $H_{160}$-band light for a putative nuclear point source but a more important 35% for a putative bulge. In both cases, however, the $R_{\rm e}$ of the disk component is not significantly different from that of the best-fit single-component model (with $n = 2$). Also, as we determine in Paper II, the clump closest to the center in each of the other four disks, which could be interpreted as a young bulge, makes a marginal contribution of < 5% to the total rest-frame $\approx 5000$ Å light, and even only $\approx 13\%$ for the more prominent central peak of BX 663.[18] It thus appears unlikely that the sizes inferred for the disks in our SINS NIC2 sample would be significantly affected by the presence of a bulge, neglected in our Sérsic model fits.

Another caveat is that the effects of dust obscuration are ignored. Extinction may significantly modify the surface brightness distributions, and hence the best-fit sizes. In particular, higher extinction toward the central parts of the sources will lead to shallower observed inner profiles. For BX 610, our seeing-limited SINFONI $H$ and $K$-band data are of sufficient S/N to constrain the radial variations of the H$\beta$/H$\alpha$ flux ratio (P. Buschkamp et al. 2011, in preparation). The Balmer decrement suggests indeed an increase in visual extinction by $\approx 1$ mag in the inner $\approx 5$ kpc, so that the intrinsic inner light profile could be steeper and the effective radius could be smaller. Moreover, differential extinction toward the H II regions and the stars could affect the relative rest-frame optical and H$\alpha$ effective radii. The existing data for our NIC2 targets do not allow us, however, to constrain on $\sim$ kpc scales the effects of spatial variations in dust extinction and of differential obscuration between the H II regions and the bulk of the stellar populations.

Finally, the depth of the $H_{160}$ band and H$\alpha$ maps may also influence the best-fit Sérsic model parameters, including the $n$ index and $R_{\rm e}$. Our SINFONI and NIC2 data sets are fairly deep in terms of what can be achieved with these instruments (see Sections 2.2 and 2.6), and the radial light profiles are traced to $\gtrsim 2 \times R_{\rm e}$ (Figures 6 and 12). Nonetheless, the $3\sigma$ surface brightness limits correspond to fairly high H$\alpha$ and rest-frame

---

[18] From detailed modeling of the H$\alpha$ kinematics of SINS disks with high-quality SINFONI data, including four of our targets, Genzel et al. (2008) found a trend of increasing central dynamical mass concentration with stellar evolutionary stage, which could be interpreted as evidence for growing bulges/inner disks. The inferred ratio of enclosed dynamical mass within 3 kpc and 10 kpc ranges from <0.15 for MD 41, to 0.2 for BX 482, and 0.4 for BX 389 and BX 610. Disentangling the relative contributions of a bulge and the underlying disk from these data is uncertain but these estimates would provide conservative upper limits to bulge-to-disk mass ratios.

$g$-band luminosities of $L_{H\alpha} \approx 4.3 \times 10^{39}$ erg s$^{-1}$ kpc$^{-2}$ and $L_g^{\rm rest} \approx 6.7 \times 10^8$ $L_{g,\odot}$ kpc$^{-2}$ at the median $z = 2.2$ of our NIC2 targets, and it is conceivable that fainter extended emission in the outer parts is undetected in our data.

### 7.3. Relation Between Kinematics and Morphologies

Arguably, one of the key aspects in the study of high-redshift galaxies is a characterization of the mass assembly process, and, in particular, pinpointing evidence for the occurrence of major mergers and interactions or, in their absence, for the establishment of disk-like systems, which are a prediction of models of galaxy formation. There are several inherent difficulties in studies based on morphologies, including bandshifting, intrinsically complex structure, and uncertainties in the timescales over which key merger signatures are observable (e.g., Toft et al. 2007; Elmegreen et al. 2007, 2009; Lotz et al. 2008, 2010a, 2010b). Therefore, kinematics appear to be a prerequisite for a robust distinction although there are possible complications as well (for instance, particular merger configurations mimicking disk-like kinematics; e.g., Law et al. 2006; Shapiro et al. 2008; Robertson & Bullock 2008; Förster Schreiber et al. 2009; Épinat et al. 2010). Morphologies and kinematics together make for a powerful combination, mitigating the respective potential limitations as well as providing a more complete picture of individual galaxies (see also Neichel et al. 2008).

The kinematic classification of our six SINS targets, all disks except BX 528, was first based on SINFONI data sets taken with the 0.″125 pixel$^{-1}$ scale, at $\approx$0.″5 or $\approx$4.1 kpc resolution (0.″39 and 3.2 kpc for the NGS-AO data of BX 663). Initially based on qualitative assessment of both the H$\alpha$ velocity field and velocity dispersion map (Förster Schreiber et al. 2006b), the classification into disk- and merger-like systems was quantitatively confirmed through the application of kinemetry (Shapiro et al. 2008), with the exception of BX 663 due to S/N limitations outside of the inner regions. To date, BX 482 is the only target among our NIC2 sample followed-up with AO and the 0.″05 pixel$^{-1}$ scale, with effective resolution of 0.″17. Its kinematic classification as a disk is further confirmed with the higher resolution data, although more detail in the H$\alpha$ emission and kinematic maps is resolved. Fourteen other galaxies from the full SINS survey were classified by kinemetry, of which four have follow-up AO observations at $\sim$0.″15–0.″20 resolution (Shapiro et al. 2008; Genzel et al. 2008; Förster Schreiber et al. 2009; Genzel et al. 2011; P. Buschkamp et al. 2011, in preparation). In all cases, as for BX 482, the kinematic classification is the same whether it is based on the seeing-limited or the AO data sets.

At first glance, the NIC2 $H_{160}$ images of our six targets at 0.″145 resolution ($\approx$1.2 kpc) reveal rich substructure at all surface brightness levels. Qualitatively, multiple bright compact components can be interpreted as distinct interacting/merging units, asymmetries in the more diffuse emission or distorted isophotes on large scales can be attributed to tidal features (e.g., Lotz et al. 2004; Conselice et al. 2005). On the other hand, these characteristics may also result from internal dynamical processes within gas-rich disks, such as bar- and spiral-like features from non-axisymmetric perturbations or luminous kpc-sized clumps resulting from disk instabilities and tidal-like features induced by the mutual interactions between massive clumps (e.g., Bournaud et al. 2007, 2008). It may therefore not be immediately obvious whether a system is a disk or a merger from simple visual inspection. Quantitatively, as found in Section 4.1.2, all the kinematically classified disks among our

NIC2 sample have Sérsic indices $n \leqslant 2$ (and even $< 1$ when excluding the AGN source BX 663), consistent with structurally late-type, disky systems.

Among our NIC2 sample, BX 610 appears to be a particularly striking example where the rest-frame optical morphology reflects tell-tale signatures of internal dynamical processes. Indeed, its appearance, as outlined in Section 3.1, exhibits evidence for a bar and features reminiscent of spiral arms, and there is no evidence for any nearby companion in our NIC2 and SINFONI data, nor of recent merging. This galaxy is one of the most robust examples of rotating disk kinematics among the SINS survey (Förster Schreiber et al. 2006b; Genzel et al. 2008; Shapiro et al. 2008; Cresci et al. 2009), with the H$\alpha$ velocity field exhibiting the classical "spider diagram" of isovelocity contours, a nearly axisymmetric and centrally peaked velocity dispersion map, and a close correspondence of the kinematic center and major axis with the geometrical center and morphological major axis (from both the rest-frame optical and H$\alpha$ emission). BX 610 shows several prominent clumps and direct observations of CO molecular gas indicate a very high gas to baryonic mass fraction of $\sim$55% (Tacconi et al. 2010). All these properties suggest that BX 610 may be one such apparently isolated galaxy where clumps formed from fragmentation in a Toomre-unstable gas-rich disk and where efficient secular processes drive its early dynamical evolution (Genzel et al. 2008, see also Carollo et al. 2007; Bournaud et al. 2007; Dekel et al. 2009; Agertz et al. 2009; Ceverino et al. 2010). While BX 610 is a particularly remarkable case, the other disks among our NIC2 targets as well as other high $z$ samples studied at high resolution (e.g., Bournaud et al. 2008; Elmegreen & Elmegreen 2005; Elmegreen et al. 2009; Genzel et al. 2011; and Paper II) show prominent clumps and properties consistent with the above theoretical scenario.

While the majority of objects in our SINS NIC2 sample are classified as disks, it is noteworthy to highlight examples of how the unique combination of H$\alpha$ kinematics and rest-frame optical morphologies sheds light on galaxy interactions. For BX 528, the H$\alpha$ kinematics clearly indicate its merger nature even at the $\approx$0.″6 seeing-limited resolution of the SINFONI data (Förster Schreiber et al. 2006b; Shapiro et al. 2008). The reversal in velocity gradient across the system could be produced by a counterrotating binary merger. In the NIC2 image, the system is resolved into two main "SE" and "NW" components separated by about 1″ (8 kpc) in projection, and connected by a fainter "bridge" of emission. Single-component Sérsic model fits to the $H_{160}$ map, either at the original NIC2 resolution or convolved to the lower resolution of the SINFONI observations, imply a shallow inner light profile with $n \sim 0.2$, evidently caused by the lower surface brightness between the SE and NW components. As seen in Section 3.1, at 0.″6 resolution, both the H$\alpha$ and smoothed $H_{160}$-band morphologies appear rather regular and the SE and NW components are not discerned, making it impossible to distinguish from disk-like systems. Moreover, BX 528 does not stand out compared to the disks in our sample in the $G - \Psi - M_{20}$ parameter space based on the high-resolution NIC2 image (Figure 7). Thus, for BX 528, both the H$\alpha$ kinematics and the high-resolution rest-frame optical imaging are necessary to fully characterize the nature of this system.

Even if not as significantly as BX 528, BX 389 also presents evidence for galaxy interaction (Figure 10). The H$\alpha$ kinematics at 0.″5 resolution show fairly regular motions consistent with rotation in a highly inclined disk. The various line maps from the $K$- and $H$-band seeing-limited SINFONI data all exhibit an

extension to the south of the center, and the rest-frame optical line ratios ([N II]/H$\alpha$, [O III]/H$\beta$) are consistent with either a low-metallicity companion or shock excitation in a starburst-driven galactic outflow (Lehnert et al. 2009; P. Buschkamp et al. 2011, in preparation). This extension does not appear kinematically distinct from the main part of the source, with line-of-sight velocities similar to those along the major axis of the main body of the galaxy, on the same side and at the same projected radii. The NIC2 $H_{160}$-band imaging reveals that this is a separate component, at a projected distance of 5 kpc below the galactic plane of BX 389, supporting the nearby satellite interpretation. For BX 389, therefore, the high-resolution near-IR imaging resolves the companion from the main part of the source and the kinematics confirm the physical association between the two components.

Assuming that the observed 1.6 $\mu$m light traces closely the stellar mass in our NIC2 targets (see Section 7.1.2), we can set constraints on the mass ratios of the different components in BX 528 and BX 389. Various estimates based on the two-component Sérsic model fits (Section 4.1), on simple aperture photometry, and on the fractional light contributions of the associated "clumps" (presented in Paper II) imply a mass ratio in the range 1.2:1 to 1.9:1 for BX528−SE relative to BX528−NW, and 6:1 to 20:1 for the main part of BX 389 relative to the southern companion. From the stellar mass ratio, BX 528 is a nearly equal-mass major merger, in agreement with the signatures and classification from the H$\alpha$ kinematics. In contrast, the southern companion of BX 389 represents a minor merger, unlikely to have strong impact on the large-scale kinematics of the primary component and consistent with the lack of substantial disturbances in the kinematics expected for major mergers.

We conclude from the above that the H$\alpha$ kinematics and rest-frame optical continuum morphologies of our NIC2 sample draw a consistent picture for the nature of each target and are very complementary. The kinematics, even at $\sim$3–5 kpc resolution, are sufficient (and in some cases necessary, as for BX 528) to reliably distinguish between disks and major mergers. We caution that there will be specific cases where a system's configuration will lead to ambiguous or erroneous classification, also depending on the data quality (Shapiro et al. 2008; Law et al. 2009), but this does not appear to be the case for the objects studied in this paper. Morphologies (as well as kinematics) at higher $\sim$1 kpc resolution then reveal further details and are important to identify minor mergers, and more subtle or smaller scale signatures of internal dynamical processes (e.g., Bournaud et al. 2008; Genzel et al. 2008, 2011).

## 8. SUMMARY

We have presented *HST*/NIC2 F160W imaging for a unique sample of six $z \sim 2$ star-forming galaxies with VLT/SINFONI integral field spectroscopic measurements. Our analysis has been based on the combined NIC2 and SINFONI seeing-limited and AO-assisted data sets, along with multi-wavelength ground-based photometry and, in one case, *HST*/ACS imaging. Using NIC2 imaging alone we have carried out galaxy structural analyses, using both parametric and non-parametric approaches, and placed the structural properties of our SINS NIC2 sample in the larger context of the correlations between morphology and star formation activity present at $z \sim 2$. However, it is the full combination of data sets presented here that has enabled investigations of unprecedented detail into the dynamical nature of our targets and the importance (or lack thereof) of mergers of

different mass ratios; the relative galaxy sizes traced by recent star formation and stellar mass; and spatial variations in the stellar $M/L$ and stellar mass surface density.

The main scientific conclusions of this paper can be summarized as follows.

1. The rest-frame optical continuum morphology of our targets yields classifications consistent with those based on ionized gas kinematics. Those systems with disk-like kinematics (the majority of our sample) are characterized by disk-like structures in rest-frame optical light. Furthermore, for the one target (BX 528) with kinematics indicative of binary counterrotating elements, the NIC2 image is clearly resolved into two, discrete components separated by $\approx 1''$, or 8 kpc. While BX 528 may provide evidence for a major merger, the morphology and kinematics of BX 389 provide evidence for a less dramatic interaction. The SINFONI kinematics for BX 389 indicate regular disk rotation, but both SINFONI H$\alpha$ maps and NIC2 rest-frame optical imaging reveal a low-luminosity companion at roughly the same line-of-sight velocity, and a projected distance of 5 kpc—possibly a minor merger in action.

2. We use both parametric (Sérsic profile) and non-parametric ($G$, $\Psi$, $M_{20}$) methods for characterizing the NIC2 morphologies of the SINS NIC2 sample. The majority of these objects are characterized by shallow ($n < 1$) inner light profiles, with a median effective radius of $R_e \sim 5$ kpc. Significant residuals are found with respect to the model fits for some objects due to the presence of multiple discrete clumps in the surface-brightness distributions, giving rise to an overall irregular appearance. The $G$, $\Psi$, and $M_{20}$ values for the sample also reflect the clumpy appearance, with significantly higher $M_{20}$ and $\Psi$ values than would be derived for axisymmetric, monolithic, and compact galaxies at similar redshift. The relatively low $G$ values indicate the lack of any single, prominent bulge component.

3. Given the small sample size, and the active levels of ongoing star formation in all of our targets, it is difficult to extract strong trends between morphology and other galaxy properties within the SINS NIC2 sample. However, a comparison with other $z \sim 2$ samples selected using a rest-frame optical (observed $K$ band) or mid-IR (observed 24 $\mu$m) limit reveals that our galaxies follow the broader trends of increasing size, $M_{20}$, and $\Psi$, and decreasing $n$, $G$, and stellar mass surface density, with increasing specific star formation rate. At the same time, the larger ensemble of galaxies reflects a considerable diversity in structure at fixed stellar mass. While these trends have been presented in other work using seeing-limited or lower resolution NIC3 images, the sample with adequate resolution for detailed profile fits (i.e., NIC2) is still very small, and our objects represent an extension of the deep $z \sim 2$ NIC2 data set to higher specific star formation rate.

4. The data presented here allow for a comparison between rest-frame optical morphologies and those derived from tracers of active star formation such as H$\alpha$ emission and rest-frame UV light. Some theoretical models (Sales et al. 2009; Dutton et al. 2011) predict that the size of the galaxy obtained from tracers dominated by young stellar populations, such as H$\alpha$ emission, should be systematically larger than that traced by rest-frame optical light. For the SINS NIC2 sample (excluding the one putative major merger, BX 528), the H$\alpha$ and NIC2 $H_{160}$-band sizes reveal no significant differences. For the one object with AO-assisted

SINFONI data obtained at comparable resolution to our NIC2 imaging (BX 482), the non-parametric coefficients for Hα and rest-frame optical continuum emission are very similar. Furthermore, the average NIC2 $G$, $\Psi$, and $M_{20}$ coefficients for our UV-selected SINS NIC2 targets are very similar to those based on rest-UV ACS morphologies for a larger sample of UV-selected galaxies at $z \sim 2$ (Peter et al. 2007). MD 41 is the only galaxy in our sample with both NIC2 F160W and ACS F814W imaging. The rest-UV morphology for this object is broadly similar to that in the rest-frame optical, although, in detail, its derived $R_e$ and $n$ are slightly larger and lower, respectively. Overall, however, the parametric and non-parametric coefficients for this object are in agreement. For UV-selected $z \sim 2$ galaxies with active star formation, the rest-frame optical appearance thus seems very similar to that traced by rest-frame UV light and ionized gas. We have also established that the NIC2 $H_{160}$-band images are truly tracing continuum emission, and are not dominated by nebular line emission.

The power of combining ∼kpc-scale resolution rest-frame optical and UV imaging together with integral field spectroscopy at seeing-limited and AO-assisted resolution has been demonstrated here for a small sample of galaxies. With such a data set, it is possible to characterize simultaneously the past and present assembly of mass, and the history of star formation. A statistical sample of such measurements will provide crucial inputs into models of the formation and evolution of massive galaxies, and will be possible with current and planned facilities in space and on the ground.

## APPENDIX

### DERIVATION OF THE RELATIONSHIP BETWEEN MASS-TO-LIGHT RATIO AND COLORS FOR MD 41

In Section 7.1, we combined the NIC2 $H_{160}$-band data with ACS $i_{814}$-band imaging available for one of our targets, MD 41, to investigate spatial variations in color, mass-to-light ratio, and stellar mass on resolved scales of 1.2 kpc. It is well known that observed colors and $M/L$ ratio of stellar populations are correlated, and this behavior can be used to infer stellar masses (see, e.g., Rudnick et al. 2006; Zibetti et al. 2009 for applications to derive the cosmic stellar mass density or spatially resolved mass maps of nearby galaxies). In this appendix, we present the derivation of the relationship we used to interpret quantitatively the $i_{814} - H_{160}$ color map of MD 41.

We employed Bruzual & Charlot (2003) models to generate the observed $i_{814} - H_{160}$ colors of stellar populations appropriate for $z = 2.2$, corresponding to the redshift of MD 41. The

colors were synthesized from the redshifted model spectra using the total transmission curves of the NIC2 F160W and ACS F814W bandpasses. We considered a variety of SFHs ranging from single stellar populations ("SSPs") with all stars formed instantaneously and no subsequent star formation, exponentially declining SFRs with $e$-folding timescales from 10 Myr to 1 Gyr, and CSF. The models were computed for a grid of ages from 1 Myr to 5 Gyr, and of extinctions with $A_V$ from 0 to 3 mag. We adopted the Chabrier (2003) IMF and the Calzetti et al. (2000) reddening law, and considered two different metallicities with $Z = Z_\odot$ and $0.2\,Z_\odot$.

For every parameter combination (SFH, age, $A_V$, $z$), the models provide the ratio of stellar mass to rest-frame optical luminosity. We consider here the "effective" $M/L$ ratio, i.e., where the luminosity refers to the light that reaches the observer after being attenuated by dust. We further consider the luminosity at rest-frame wavelengths close to the range probed by our NIC2 F160W data of MD 41. These choices are relevant because we ultimately combine the derived $M/L$ map with the observed $H_{160}$-band image (least affected by extinction and by light from young stars) to derive the stellar mass map. For our purposes, we approximated the rest-frame optical luminosity seen through the NIC2 F160W filter (mean wavelength of 1.61 $\mu$m, range with peak-normalized transmission $>50\%$ of 1.40–1.80 $\mu$m, corresponding to rest-frame 5080 Å and 4415–5675 Å, respectively) with the model predictions through the SDSS $g$-band filter (mean wavelength of 4695 Å and range of 4020–5330 Å). The $g$ band is $\approx$380 Å bluer than the rest-frame range probed by our NIC2 data, but it is closer in mean wavelength and has larger overlap than the $V$ band (with mean wavelength of 5510 Å and range of 5010–5865 Å). Over the entire range of SFHs and ages considered, the differences between $M_\star/L_g^{\rm rest}$ and $M_\star/L_V^{\rm rest}$ ratios are of at most a factor of two, and similarly over the range of extinction assumed. Metallicity has a very minor impact in comparison. These differences in $M/L$ ratios constitute however extremes as they are for the full range of model parameters. More realistically, the fairly narrow range in observed $i_{814} - H_{160}$ colors across MD 41 suggest only modest variations in age and extinction. With the assumption of ages $\sim$10$^7$–10$^8$ yr and $A_V \sim 1$ mag, more consistent with the results from the modeling of the integrated optical to near-IR SED of MD 41 in Section 3.3, the $M_\star/L_g^{\rm rest}$ ratio is $\approx$20% lower than the $M_\star/L_V^{\rm rest}$ ratio, with little dependence on the assumed SFH. Since our NIC2 F160W data probe a rest-frame wavelength range intermediate between the $g$ and $V$ bands, the numbers above represent upper limits on the offset between $M_\star/L_g^{\rm rest}$ we use and the actual stellar mass to rest-frame optical luminosity ratio from our data.

Figure 19 plots the observed $i_{814} - H_{160}$ colors versus $M_\star/L_g^{\rm rest}$ ratios derived from the models for solar metallicity. Curves with different colors correspond to different SFHs. Stellar age increases along the curves from blue to red $i_{814} - H_{160}$ colors, and from low to high $M/L$ ratios. Different line styles are used to plot models with different extinction (shown for $A_V = 0$, 1, 2, and 3 mag in the figure). The main effect of increasing extinction is to shift the model curves along a direction that is roughly parallel to the age tracks. The model curves occupy a fairly well defined locus in the observed $i_{814} - H_{160}$ versus $M_\star/L_g^{\rm rest}$ parameter space, reflecting the strong degeneracy between stellar age, extinction, and SFH in these properties. This degeneracy can be exploited to derive the mean effective $M/L$ ratio for a given observed color, which, multiplied by the observed luminosity, yields a stellar mass estimate
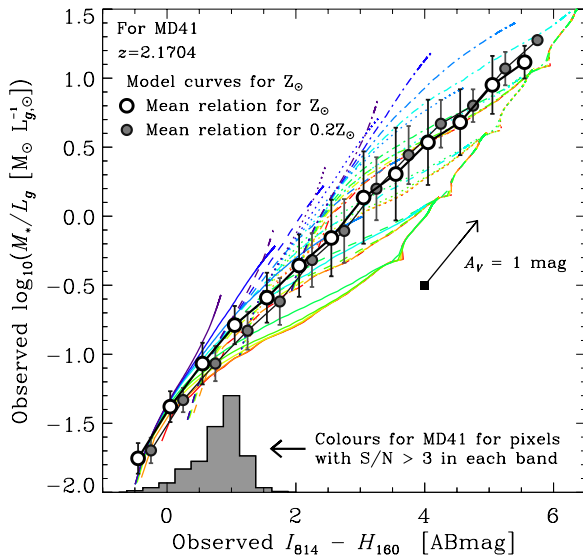
**Figure 19.** Relationship between observed $i_{814} - H_{160}$ colors and the ratio of stellar mass to rest-frame $g$-band luminosity $M_\star/L_g^{\rm rest}$. Both the colors and the $M_\star/L_g^{\rm rest}$ correspond to observed quantities, uncorrected for the effects of dust extinction. The various curves plotted in colors are computed from Bruzual & Charlot (2003) models with solar metallicity, a Chabrier (2003) IMF, and the Calzetti et al. (2000) reddening law. Different colors are used for different star formation histories: red to blue represent SFHs of increasing star formation timescale from a single stellar population, a suite of exponentially declining SFRs with $e$-folding timescales between 10 Myr and 1 Gyr, and constant SFR. Different line styles are also used for models computed with different values for extinction: $A_V = 0$ (solid), 1 (dashed), 2 (dotted), and 3 mag (dash-dotted). Age increases along each model curve from blue to red $i_{814} - H_{160}$ colors and low to high $M_\star/L_g^{\rm rest}$ ratios. As shown by the arrow, the effects of extinction are roughly parallel to the locus of the various models. The colors are synthesized from the model spectrum redshifted to the $z = 2.1704$ of MD 41, using the transmission curves for the ACS F814W and NIC2 F160W filters. The large white-filled circles and thick black line show the mean relationship derived from the solar metallicity models. For comparison, the smaller gray-filled circles and thinner black line are the relationship that is derived from models with 1/5 solar metallicity. The gray-shaded histogram shows the distribution of observed $i_{814} - H_{160}$ colors of all individual pixels with S/N > 3 in each band for MD 41 (see Section 7.1).

(A color version of this figure is available in the online journal.)

without requiring any knowledge about the actual SFH, age, or extinction.

We computed the "mean" relationship by taking the average of the minimum and maximum values in $\log(M_\star/L_g^{\rm rest})$ over all model curves within equally spaced bins of width 0.1 mag in $i_{814} - H_{160}$ colors. By proceeding in this way, we reduced the impact of the discreteness of our grids of SFHs and extinction. Over the ranges in colors where models for all SFHs and all ages for a fixed extinction value are represented, the average of the minimum and maximum $\log(M_\star/L_g^{\rm rest})$ is very close to the weighted mean over all models, where the weights are obtained from the time span of each model within a given color bin; the differences are at most 0.08 dex in $\log(M_\star/L_g^{\rm rest})$. Varying the $A_V$ value has little impact since extinction effects are mostly along the relationship. The mean relationship for solar metallicity is plotted in Figure 19 (white-filled circles and thick solid black line), with error bars corresponding to the standard deviation of all models within each color bin. The relationship derived for 1/5 solar metallicity is also shown for comparison (gray-filled circles and thin solid black line), but is very similar to the one for solar metallicity. For our analysis of MD 41, we adopted the $i_{814} - H_{160}$ versus $\log(M_\star/L_g^{\rm rest})$ relationship derived for $Z = Z_\odot$ models. The standard deviation of the models suggest

that the relationship is accurate to 0.15 dex in $\log(M_\star/L_g^{\rm rest})$ over the range of observed colors across MD 41 (indicated by the shaded histogram in Figure 19).

## REFERENCES

Abraham, R. G., van den Bergh, S., & Nair, P. 2003, ApJ, 588, 218
Abraham, R. G., et al. 2007, ApJ, 699, 184
Adelberger, K. L., Steidel, C. C., Shapley, A. E., Hunt, M. P., Erb, D. K., Reddy, N. A., & Pettini, M. 2004, ApJ, 607, 226
Agertz, O., Teyssier, R., & Moore, B. 2009, MNRAS, 397, L64
Allen, C. W. 1976, Astrophysical Quantities (3rd ed.; London: Athlone)
Bell, E. F., et al. 2004, ApJ, 608, 752
Bertin, E., & Arnouts, S. 1996, A&AS, 117, 393
Blumenthal, G. R., Faber, S. M., Primack, J. R., & Rees, M. J. 1984, Nature, 311, 517
Bonnet, H., et al. 2004, Messenger, 117, 17
Bouché, N., et al. 2007, ApJ, 671, 303
Bouchet, P., Lequeux, J., Maurice, E., Prévot, L., & Prévot-Burnhon, M. L. 1985, A&A, 149, 330
Bournaud, F., Elmegreen, B. G., & Elmegreen, D. M. 2007, ApJ, 670, 237
Bournaud, F., et al. 2008, A&A, 486, 741
Bruzual, A. G., & Charlot, S. 2003, MNRAS, 344, 1000
Burkert, A., et al. 2010, ApJ, 725, 2324
Calzetti, D., Armus, L., Bohlin, R. C., Kinney, A. L., Koornneef, J., & Storchi-Bergmann, T. 2000, ApJ, 533, 682
Cameron, E., Carollo, C. M., Oesch, P. A., Bouwens, R. J., Illingworth, G. D., Trenti, M., Labbé, I., & Magee, D. 2010, ApJ, submitted (arXiv:1007.2422)
Carollo, C. M., et al. 2007, ApJ, 658, 960
Ceverino, D., Dekel, A., & Bournaud, F. 2010, MNRAS, 404, 2151
Chabrier, G. 2003, PASP, 115, 763
Chapman, S. C., Blain, A. W., Ivison, R. J., & Smail, I. R. 2003, Nature, 422, 695
Cimatti, A., et al. 2008, A&A, 482, 21
Conselice, C. J., Blackburne, J. A., & Papovich, C. 2005, ApJ, 620, 564
Cresci, G., et al. 2009, ApJ, 697, 115
Daddi, E., Cimatti, A., Renzini, A., Fontana, A., Mignoli, M., Pozzetti, L., Tozzi, P., & Zamorani, G. 2004, ApJ, 617, 746
Daddi, E., et al. 2010, ApJ, 713, 686
Dalcanton, J. J., Spergel, D. N., & Summers, F. J. 1997, ApJ, 482, 659
Damjanov, I., et al. 2009, ApJ, 695, 101
Dasyra, K. M., Yan, L., Helou, G., Surace, J., Sajina, A., & Colbert, J. 2008, ApJ, 680, 232
Davé, R., Finlator, K., Oppenheimer, B. D., Fardal, M., Katz, N., Kereš, D., & Weinberg, D. H. 2010, MNRAS, 404, 1355
Dekel, A., Sari, R., & Ceverino, D. 2009, ApJ, 703, 785
Dib, S., Bell, E., & Burkert, A. 2006, ApJ, 638, 797
Dickinson, M., Papovich, C., Ferguson, H. C., & Budavári, T. 2003, ApJ, 587, 25
Dutton, A. A. 2009, MNRAS, 396, 121
Dutton, A. A., & van den Bosch, F. C. 2009, MNRAS, 396, 141
Dutton, A. A., van den Bosch, F. C., Dekel, A., & Courteau, S. 2007, ApJ, 654, 27
Dutton, A. A., et al. 2011, MNRAS, 410, 1660
Eisenhauer, F., et al. 2003, Messenger, 113, 17
Elmegreen, B. G., & Elmegreen, D. M. 2005, ApJ, 627, 632
Elmegreen, B. G., Elmegreen, D. M., Fernandez, M. X., & Lemonias, J. J. 2009, ApJ, 692, 12
Elmegreen, D. M., Elmegreen, B. G., Ravindranath, S., & Coe, D. A. 2007, ApJ, 658, 763
Épinat, B., Amram, P., Balkowski, C., & Marcelin, M. 2010, MNRAS, 401, 2113
Épinat, B., et al. 2009, A&A, 504, 789
Erb, D. K., Shapley, A. E., Steidel, C. C., Pettini, M., Adelberger, K. L., Hunt, M. P., Moorwood, A. F. M., & Cuby, J.-G. 2003, ApJ, 591, 101
Erb, D. K., Steidel, C. C., Shapley, A. E., Pettini, M., & Adelberger, K. L. 2004, ApJ, 612, 122
Erb, D. K., Steidel, C. C., Shapley, A. E., Pettini, M., Reddy, N. A., & Adelberger, K. L. 2006, ApJ, 646, 107
Fall, S. M., & Efstathiou, G. 1980, MNRAS, 193, 189
Flores, H., Hammer, F., Puech, M., Amram, P., & Balkowski, C. 2006, A&A, 455, 107
Förster Schreiber, N. M., et al. 2006a, AJ, 131, 1891
Förster Schreiber, N. M., et al. 2006b, ApJ, 645, 1062
Förster Schreiber, N. M., et al. 2009, ApJ, 706, 1364

Franx, M., van Dokkum, P. G., Förster Schreiber, N. M., Wuyts, S., Labbé, I., & Toft, S. 2008, ApJ, 688, 770
Franx, M., et al. 2003, ApJ, 587, L79
Genzel, R., Tacconi, L. J., Rigopoulou, D., Lutz, D., & Tecza, M. 2001, ApJ, 563, 527
Genzel, R., et al. 2006, Nature, 442, 786
Genzel, R., et al. 2008, ApJ, 687, 59
Genzel, R., et al. 2011, ApJ, in press (arXiv:1011.5360)
Hopkins, P. F., Bundy, K., Murray, N., Quataert, E., Lauer, T. R., & Ma, C. 2009, MNRAS, 398, 898
Immeli, A., Samland, M., Gerhard, O., & Westera, P. 2004a, A&A, 413, 547
Immeli, A., Samland, M., Westera, P., & Gerhard, O. 2004b, ApJ, 611, 20
Jones, T., Swinbank, A. M., Ellis, R. S., Richard, J., & Stark, D. P. 2010, MNRAS, 404, 1247
Kauffmann, G., Heckman, T. M., De Lucia, G., Brinchmann, J., Charlot, S., Tremonti, C., White, S. D. M., & Brinkmann, J. 2006, MNRAS, 367, 1394
Kauffmann, G., et al. 2003, MNRAS, 341, 54
Kennicutt, R. C., Jr. 1998, ApJ, 498, 541
Krajnović, D., Cappellari, M., de Zeeuw, P. T., & Copin, Y. 2006, MNRAS, 366, 787
Kriek, M., van der Wel, A., van Dokkum, P. G., Franx, M., & Illingworth, G. D. 2008a, ApJ, 682, 896
Kriek, M., van Dokkum, P. G., Franx, M., Illingworth, G. D., & Magee, D. K. 2009, ApJ, 705, L71
Kriek, M., et al. 2006, ApJ, 649, L71
Kriek, M., et al. 2008b, ApJ, 677, 219
Kroupa, P. 2001, MNRAS, 322, 231
Labbé, I., et al. 2003, ApJ, 591, L95
Law, D. R., Steidel, C. C., & Erb, D. K. 2006, AJ, 131, 70
Law, D. R., Steidel, C. C., Erb, D. K., Larkin, J. E., Pettini, M., Shapley, A. E., & Wright, S. A. 2007a, ApJ, 669, 929
Law, D. R., Steidel, C. C., Erb, D. K., Larkin, J. E., Pettini, M., Shapley, A. E., & Wright, S. A. 2009, ApJ, 697, 2057
Law, D. R., Steidel, C. C., Erb, D. K., Pettini, M., Reddy, N. A., Shapley, A. E., Adelberger, K. L., & Simenc, D. J. 2007b, ApJ, 656, 1
Lehnert, M. D., Nesvadba, N. P. H., Le Tiran, L., Di Matteo, P., van Driel, W., Douglas, L. S., Chemin, L., & Bournaud, F. 2009, ApJ, 699, 1660
Lilly, S. J., et al. 1998, ApJ, 500, 75
Lotz, J. M., Jonsson, P., Cox, T. J., & Primack, J. R. 2008, MNRAS, 391, 1137
Lotz, J. M., Jonsson, P., Cox, T. J., & Primack, J. R. 2010a, MNRAS, 404, 575
Lotz, J. M., Jonsson, P., Cox, T. J., & Primack, J. R. 2010b, MNRAS, 404, 590
Lotz, J. M., Madau, P., Giavalisco, M., Primack, J., & Ferguson, H. 2006, ApJ, 636, 592
Lotz, J. M., Primack, J., & Madau, P. 2004, AJ, 128, 163
Maier, C., et al. 2009, ApJ, 694, 1099
Maller, A. H., Berlind, A. A., Blanton, M. R., & Hogg, D. W. 2009, ApJ, 691, 394
Mancini, C., et al. 2010, MNRAS, 401, 933
Maraston, C. 2005, MNRAS, 362, 799
Maraston, C., Pforr, J., Renzini, A., Daddi, E., Dickinson, M., Cimatti, A., & Tonini, C. 2010, MNRAS, 407, 830
Mo, H. J., Mao, S., & White, S. D. M. 1998, MNRAS, 295, 319
Navarro, J. F., & Steinmetz, M. 2000, ApJ, 538, 477
Neichel, B., et al. 2008, A&A, 484, 159
Noguchi, M. 1999, ApJ, 514, 77
Overzier, R. A., Heckman, T. M., Schiminovich, D., Basy-Zych, A., Gonçalves, T., Martin, D. C., & Rich, R. M. 2010, ApJ, 710, 979
Panella, M., et al. 2009, ApJ, 701, 787
Papovich, C., Dickinson, M., Giavalisco, M., Conselice, C. J., & Ferguson, H. C. 2005, ApJ, 631, 101
Peng, C. Y., Ho, L. C., Impey, C. D., & Rix, H.-W. 2002, AJ, 124, 266
Peter, A. H. G., Shapley, A. E., Law, D. R., Steidel, C. C., Erb, D. K., Reddy, N. A., & Pettini, M. 2007, ApJ, 668, 23

Prévot, M. L., Lequeux, J., Prévot, L., Maurice, E., & Rocca-Volmerange, B. 1984, A&A, 132, 389
Puech, M., Hammer, F., Lehnert, M. D., & Flores, H. 2007, A&A, 466, 83
Ravindranath, S., et al. 2004, ApJ, 604, L9
Reddy, N. A., Erb, D. K., Pettini, M., Steidel, C. C., & Shapley, A. E. 2010, ApJ, 712, 1070
Renzini, A. 2009, MNRAS, 398, L58
Robertson, B. E., & Bullock, J. S. 2008, ApJ, 685, L27
Rudnick, G., et al. 2006, ApJ, 650, 624
Sales, L. V., Navarro, J. F., Schaye, J., Dalla Vecchia, C., Springel, V., Haas, M. R., & Helmi, A. 2009, MNRAS, 399, L64
Salpeter, E. E. 1955, ApJ, 121, 161
Scarlata, C., et al. 2007a, ApJS, 172, 406
Scarlata, C., et al. 2007b, ApJS, 172, 494
Sérsic, J. L. 1968, Atlas de Galaxias Australes (Cordoba: Observatorio Astronomico)
Shapiro, K., et al. 2008, ApJ, 682, 231
Shapley, A. E., Erb, D. K., Pettini, M., Steidel, C. C., & Adelberger, K. L. 2004, ApJ, 612, 108
Shapley, A. E., Steidel, C. C., Adelberger, K. L., Dickinson, M., Giavalisco, M., & Pettini, M. 2001, ApJ, 562, 95
Shen, S., Mo, H. J., White, S. D. M., Blanton, M. R., Kauffmann, G., Voges, W., Brinkmann, J., & Csabai, I. 2003, MNRAS, 343, 978
Somerville, R. S., et al. 2008, ApJ, 672, 776
Stanford, S. A., Dickinson, M., Postman, M., Ferguson, H. C., Lucas, R. A., Conselice, C. J., Budavàri, T., & Somerville, R. 2004, AJ, 127, 131
Stark, D. P., Swinbank, A. M., Ellis, R. S., Dye, S., Smail, I. R., & Richard, J. 2008, Nature, 455, 775
Steidel, C. C., Adelberger, K. L., Shapley, A. E., Pettini, M., Dickinson, M., & Giavalisco, M. 2003, ApJ, 592, 728
Steidel, C. C., Shapley, A. E., Pettini, M., Adelberger, K. L., Erb, D. K., Reddy, N. A., & Hunt, M. P. 2004, ApJ, 604, 534
Swinbank, A. M., et al. 2010, MNRAS, 405, 234
Tacconi, L. J., et al. 2010, Nature, 463, 781
Toft, S., Franx, M., van Dokkum, P. G., Förster Schreiber, N. M., Labbé, I., Wuyts, S., & Marchesini, D. 2009, ApJ, 705, 255
Toft, S., et al. 2007, ApJ, 671, 285
Trujillo, I., Conselice, C. J., Bundy, K., Cooper, M. C., Eisenhardt, P., & Ellis, R. S. 2007, MNRAS, 382, 109
Trujillo, I., et al. 2006, ApJ, 650, 18
van den Bergh, S., Abraham, R. G., Ellis, R. S., Tanvir, N. R., & Glazebrook, K. G. 1996, AJ, 112, 359
van den Bergh, S., Cohen, J. G., & Crabbe, C. 2001, AJ, 122, 611
van der Wel, A., Holden, B. P., Zirm, A. W., Franx, M., Rettura, A., Illingworth, G. D., & Ford, H. C. 2008, ApJ, 688, 48
van Dokkum, P. G., et al. 2004, ApJ, 611, 703
van Dokkum, P. G., et al. 2006, ApJ, 638, L59
van Dokkum, P. G., et al. 2008, ApJ, 677, L5
White, S. D. M., & Rees, M. J. 1978, MNRAS, 183, 341
Williams, R. J., Quadri, R. F., Franx, M., van Dokkum, P., & Labbé, I. 2009, ApJ, 691, 1879
Williams, R. J., Quadri, R. F., Franx, M., van Dokkum, P., Toft, S., Kriek, M., & Labbé, I. 2010, ApJ, 713, 738
Wright, S. A., Larkin, J. E., Law, D. R., Steidel, C. C., Shapley, A. E., & Erb, D. K. 2009, ApJ, 699, 421
Wright, S. A., et al. 2007, ApJ, 658, 78
Wuyts, S., Cox, T. J., Hayward, C. C., Franx, M., Hernquist, L., Hopkins, P. F., Jonsson, P., & van Dokkum, P. G. 2010, ApJ, 722, 1666
Wuyts, S., Labbé, I., Förster Schreiber, N. M., Franx, M., Rudnick, G., Brammer, G., & van Dokkum, P. G. 2008, ApJ, 682, 985
Yip, C.-W., Szalay, A. S., Wyse, R. F. G., Dobos, L., Budavári, T., & Csabai, I. 2010, ApJ, 709, 780
Zibetti, S., Charlot, S., & Rix, H.-W. 2009, MNRAS, 400, 1181
Zirm, A. W., et al. 2007, ApJ, 656, 66